

Forschungszentrum Karlsruhe
Technik und Umwelt

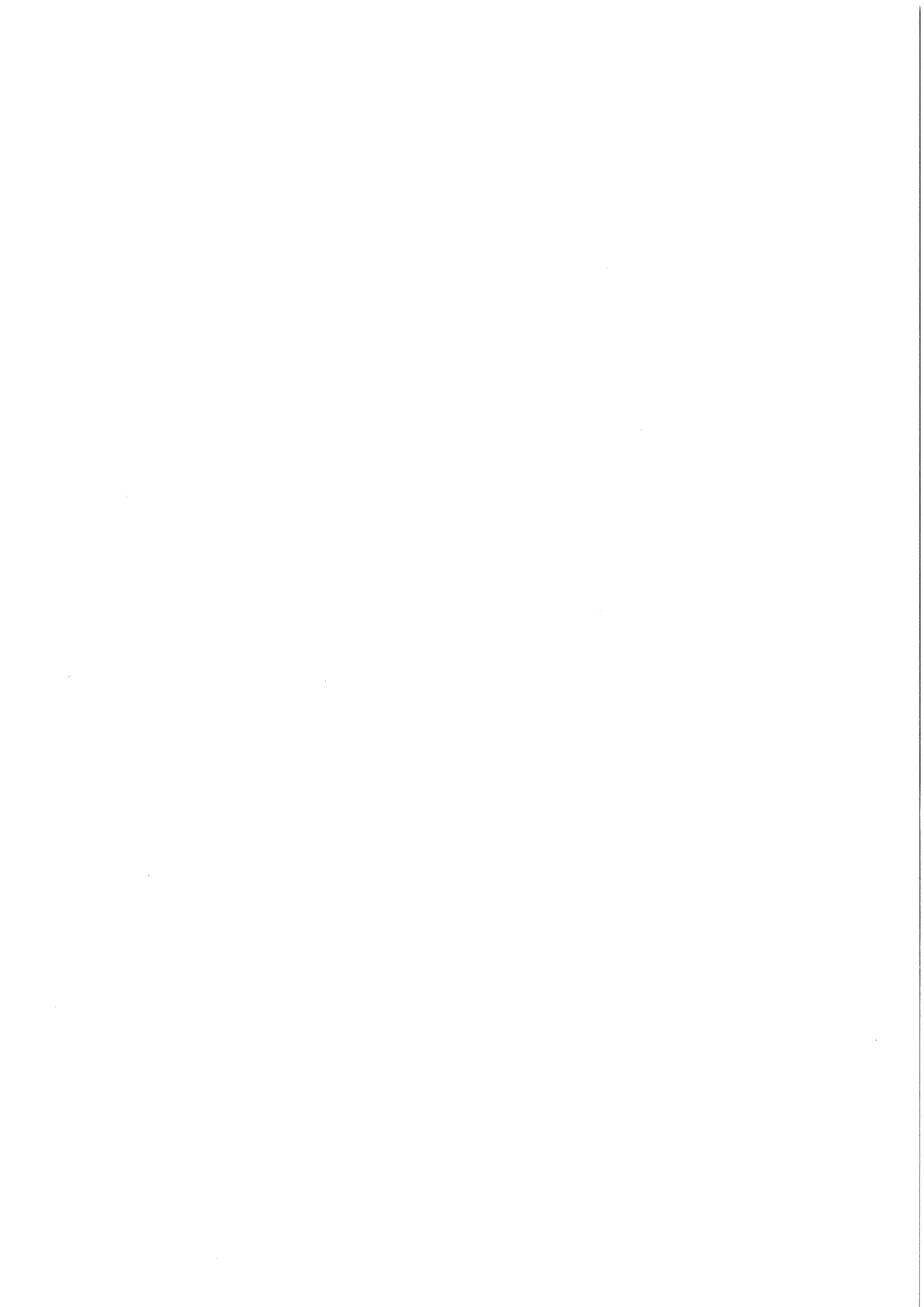
Wissenschaftliche Berichte
FZKA 5654

A Concept for the Numerical Solution of the Maxwell-Vlasov System

**E. Halter, M. Krauß, C.-D. Munz,
R. Schneider, E. Stein, U. Voß,
T. Westermann**

**Institut für Neutronenphysik und Reaktortechnik
Hauptabteilung Daten- und Informationsverarbeitung**

Oktober 1995



Forschungszentrum Karlsruhe

Technik und Umwelt

Wissenschaftliche Berichte

FZKA 5654

A Concept for the Numerical Solution of the Maxwell-Vlasov System

E. Halter¹, M. Krauß, C.-D. Munz, R. Schneider, E. Stein, U. Voß, T. Westermann²

Institut für Neutronenphysik und Reaktortechnik
Hauptabteilung Daten- und Informationsverarbeitung

¹ Fachbereich Feinwerktechnik, FH Karlsruhe,
Postfach 2440, 76012 Karlsruhe

² Fachbereich Naturwissenschaften, FH Karlsruhe,
Postfach 2440, 76012 Karlsruhe

Forschungszentrum Karlsruhe GmbH, Karlsruhe

1995

Als Manuskript gedruckt
Für diesen Bericht behalten wir uns alle Rechte vor

Forschungszentrum Karlsruhe GmbH
Postfach 3640, 76021 Karlsruhe

ISSN 0947-8620

Abstract

In this paper the basic concept of the numerical treatment of charged particles in electrical devices used in the Karlsruhe Diode (KADI) simulation code development is described. This concept includes a new interactive grid generation module based on boundary-fitted coordinates to create a computational grid in a comfortable manner. Besides the standard finite-difference approach on staggered grids, an alternative scheme based on high resolution finite-volume methods is investigated and found to be an adequate field solver for the nonstationary Maxwell equations. This is a new approach in the context of self-consistent charged particle simulation in electromagnetic fields. Several test problems show the quality and properties of the Maxwell field solver. The basic ideas of an extended particle-in-cell (PIC) method used for the particle treatment in boundary-fitted coordinates are reviewed.

Ein Konzept zur numerischen Lösung des Maxwell-Vlasov Systems

Überblick

In diesem Bericht wird das numerische Konzept zur Behandlung geladener Teilchen in elektrischen Apparaturen vorgestellt, wie es bei der Neuentwicklung des Karlsruher-Dioden-Simulationsprogramms KADI zum Tragen kommt. Der erste Baustein im Gesamtkonzept ist ein neues Modul zur interaktiven Gittererzeugung. Durch Verwendung von Gittermethoden für randangepaßte Koordinaten und den Komfort eines handelsüblichen CAD-Systems, läßt sich damit schnell und benutzerfreundlich ein passendes Berechnungsgitter erstellen. Neben dem gängigen, auf finiten Differenzen für versetzte Gitter beruhenden Zugang zur numerischen Lösung der instationären Maxwellgleichungen, untersuchten und konstruierten wir ein alternatives Schema, das auf hochauflösende finite Volumenmethoden zurückgreift. Durch den Einsatz dieser Methoden zur numerischen Lösung der Maxwellgleichungen wird auf dem Gebiet der selbstkonsistenten Simulation geladener Teilchen in elektromagnetischen Feldern ein neuer Weg beschritten. Numerische Resultate, die für verschiedene Testprobleme gewonnen wurden, geben Auskunft über die Qualität, Eigenschaften und Verwendbarkeit der untersuchten Maxwell-Feldlöser. Die wesentlichen Ideen der auf randangepaßte Koordinaten erweiterten Particle-in-Cell (PIC) Methode zur Teilchenbehandlung werden in diesem Bericht nochmals in knapper Form dargestellt.

Contents

1	Introduction	3
2	Mathematical and Numerical Model	5
3	Grid Generation	9
3.1	Boundary-Fitted Coordinates	9
3.2	Extended Grid Generation Strategies	12
3.3	Interactive Grid Generation with InGrid	13
4	Numerical Concepts for the Maxwell Equations	16
4.1	Finite-Volume Approach	17
4.1.1	Solution of the Riemann Problem and the Flux Approximation	18
4.1.2	Two-dimensional FV Scheme on Structured Quadrilateral Grids	22
4.1.3	Extention to higher order accuracy	23
4.1.4	Boundary Conditions	28
4.2	Staggered-Leapfrog FDTD Approach	33
5	Particle Treatment	37
5.1	Interpolation	37
5.2	Particle Pushing	39
5.3	Localization	40
5.4	Charge and Current Density Assignment	41
6	Results	43
6.1	Numerical Results for the homogeneous Maxwell Equations	43
6.2	Numerical Results for the inhomogeneous Maxwell Equations	46
7	Conclusion and Outlook	63
A	Maxwell's Equations in Conservation Form	67
B	Two-dimensional FV Scheme in Cartesian Grids	70

C	Unit Normals and Area of a quadrilateral Grid Zone	72
D	Miscellaneous Properties of the Matrices \mathcal{K}_i	74
E	Test Problems for the homogeneous Maxwell Equations	77
F	Test Problems for the inhomogeneous Maxwell Equations	81

1 Introduction

Providing the high densities in matter necessary for inertial confinement fusion is a challenging problem in science as well as in technology. Much progress in generating high-power ion beams has been made during the last two decades [9]. For this purpose, the KALIF pulsed power line has been installed at the Forschungszentrum Karlsruhe [5]. The high power KALIF pulse is converted to ion beams in special electrical devices, the so-called ion diodes [49, 6]. To get a deeper insight into the physical phenomena that play an important role in the ion diodes, and hence a better interpretation of the experimental results, parameter studies by numerical simulations are very useful. Theoretically it is obvious that the non-neutral plasmas inside the ion diodes can be described mathematically by the fundamental Maxwell-Vlasov equations [6, 7]. In view of numerical modelling, it is more convenient to formulate this system by its characteristic equations resulting in the so-called Maxwell-Lorentz system.

A simulation program, based on the numerical solution of the Lorentz and stationary Maxwell equations has been developed at the Forschungszentrum Karlsruhe in the last years [67]. This program is an extension of a $2\frac{1}{2}$ -dimensional PIC-code [4, 22] to boundary-fitted coordinates [56] and is called BFCPIC. It is an excellent tool for the optimization of the design of the technically relevant diodes and their resulting focusing properties [64]. However, important questions concerning the origin and consequences of electromagnetic instabilities inside the anode-cathode gap which lead to the observed microscopic divergence cannot be answered by this stationary code. For that purpose, the fully nonstationary Maxwell equations have to be considered. In order to attain this goal the Karlsruhe Diode (KADI) code initiative aims to develop a program system solving numerically the nonstationary three-dimensional Maxwell-Lorentz equations for technically relevant geometries. Because of the complexity of this problem it is convenient to go through several intermediate stages: First of all, a $2\frac{1}{2}$ -dimensional time-dependent version of the program system should be developed for Cartesian grids, which is then extended to boundary-fitted coordinates. Finally, the acquired knowledge and experience should be combined, resulting in a three-dimensional time-dependent production code using boundary-fitted coordinates.

The self-consistent motion of charged particles in electromagnetic fields as modelled by the Maxwell-Lorentz equations is a coupled system, which will be huge after discretization. In the nonstationary three-dimensional case it is one of the great challenges of high performance computing. From the stationary BFCPIC program we extrapolate that for a fully three-dimensional nonstationary approach the computational effort will be in the order of 100 CPU-hours on the present vector computer VP400EX. Hence, within all stages of the present code development one important aspect is the efficient implementation of the corresponding algorithms, especially, in view of the future high performance computer at the Forschungszentrum Karlsruhe.

The organization of this report is as follows. In Section 2 the Maxwell-Vlasov equations are given and the realization of the numerical model in its entirety is briefly

sketched out. Numerical realization and algorithmic transposition requires a computational grid. A new method of interactive grid generation for complex geometries, developed in close collaboration with the Fachhochschule Karlsruhe is presented in Section 3. One of the most important parts of the new Maxwell-Lorentz code is the field solver for the fully nonstationary Maxwell equations. Therefore, a main point of our work was first to find out appropriate strategies how to solve the Maxwell equations numerically and to show realizeable solutions. A short overview of the resulting methods of the field solver for arbitrarily structured grids is given in Section 4. Depending on the method under consideration, different algorithms solving numerically the Maxwell equations for Cartesian and cylindrical coordinates are implemented. To close the chain of interplay between Maxwell and Lorentz equations, well-known particle methods are applied. A brief review of particle treatment for boundary-fitted grids which is already well established in the BFCPIC code is given in Section 5. Finally, in Section 6, some results for test problems are presented and evaluated. Concluding remarks and a short outlook on the further activities finish this report.

2 Mathematical and Numerical Model

A plasma is, generally spoken, a hot ionized gas consisting of ions, electrons, and neutral atoms, and is therefore a classical many-body system. An important subclass of phenomena of a real plasma is obtained, if only the interaction of the charged plasma particles with the electromagnetic field is considered. Mathematically, this situation is established by the assumption that the particles are uncorrelated, and consequently the two-particle distribution function can be written as a product of one-particle distribution functions (see, e.g., [3]). This is the lowest-order closure of the hierarchy of statistical mechanics describing correlated systems. Particles are uncorrelated in the physical sense, if the so-called plasma parameter N_p ($N_p = \frac{4\pi}{3} n_0 \lambda_D^3$; where n_0 is the typical density of the plasma and λ_D is the Debye length) is very large compared to unity, which means that the relative importance of the Coulomb interaction is negligible with respect to the thermal energy. The idealized theoretical model of an uncorrelated or collisionless plasma seems to be sufficient for most physical phenomena observed in ion diodes and is described mathematically by the Maxwell-Vlasov equations. Because strong electromagnetic fields occur we have to use the relativistic Vlasov equation (see, e.g., [12])

$$(\partial_t + \mathbf{v} \cdot \nabla_x + \mathbf{F}_L \cdot \nabla_p) f_\alpha = 0, \quad (2.1a)$$

$$\mathbf{F}_L = q_\alpha (\mathbf{E} + \mathbf{v} \times \mathbf{B}), \quad (2.1b)$$

for an adequate theoretical treatment. Here, $f_\alpha = f_\alpha(\mathbf{x}, \mathbf{p}, t)$ denotes the distribution function in phase space of the plasma component $\alpha = e, i$ for electrons and ions, respectively, and ∇ is the usual divergence operator. The Lorentz force \mathbf{F}_L on the point charge q_α depends on the velocity \mathbf{v} , the electric field \mathbf{E} and the magnetic induction \mathbf{B} . In the terminology of hyperbolic partial differential equations, the general solution of (2.1a) is given by its characteristic equations, the so-called Lorentz equations,

$$\frac{d\mathbf{x}(t)}{dt} = \mathbf{v}(t), \quad (2.2a)$$

$$\frac{d\mathbf{p}(t)}{dt} = \mathbf{F}_L(t). \quad (2.2b)$$

The relativistic momentum is determined according to $\mathbf{p} = m_\alpha \gamma \mathbf{v}$ with the Lorentz factor $\gamma^2 = 1 + \frac{\mathbf{p}^2}{m_\alpha^2 c^2}$, where m_α denotes the particle mass and c the speed of light. The difficulty in solving (2.2) arises from the fact that the electric field \mathbf{E} and the magnetic induction \mathbf{B} are not given explicitly. Rather they have to be calculated in a self-consistent manner from the full set of Maxwell equations (see, e.g., [3] or [12])

$$\partial_t \mathbf{E} - c^2 \nabla \times \mathbf{B} = -c^2 \mu_0 (\mathbf{j}^{sc} + \mathbf{j}^{ext}), \quad (2.3a)$$

$$\partial_t \mathbf{B} + \nabla \times \mathbf{E} = 0, \quad (2.3b)$$

$$\nabla \cdot \mathbf{B} = 0, \quad (2.3c)$$

$$\nabla \cdot \mathbf{E} = \frac{1}{\epsilon_0} (\rho^{sc} + \rho^{ext}), \quad (2.3d)$$

where $\varrho^{ext} = \varrho^{ext}(\mathbf{x}, t)$ and $\mathbf{j}^{ext} = \mathbf{j}^{ext}(\mathbf{x}, t)$ denote the external charge and current density, produced outside the plasma. ϵ_0 and μ_0 are the usual symbols for the permittivity and the permeability of free space. The self-consistent parts of the total charge and current density are obtained from

$$\varrho^{sc}(\mathbf{x}, t) = \sum_{\alpha} q_{\alpha} \int f_{\alpha}(\mathbf{x}, \mathbf{p}, t) d^3p, \quad (2.3e)$$

$$\mathbf{j}^{sc}(\mathbf{x}, t) = \sum_{\alpha} q_{\alpha} \int \mathbf{v} f_{\alpha}(\mathbf{x}, \mathbf{p}, t) d^3p, \quad (2.3f)$$

respectively, where the integration has to be performed over the entire range of momentum. Obviously from (2.1) and (2.3), the Maxwell-Vlasov and consequently the Maxwell-Lorentz equations (2.2), (2.3) form a non-linear system described by an integro-differential equation.

Up to now the description is exact in the sense, that no numerical approximations are made. For the numerical realization of the Maxwell-Lorentz system (2.2), (2.3) well-known techniques called particle methods [22] are applied. In the following the basic ideas of these techniques will be discussed.

Computationally it is impracticable to divide the phase space into infinitesimally small cells. Therefore, it is common to define infinitesimally extended points P_i in the phase space which represent phase fluid elements. These phase fluid elements are called macro particles. We consider now a sample of macro particles of each species α with the phase space coordinates

$$M_{\alpha} = \{(\mathbf{x}_i, \mathbf{p}_i); \quad i = 1, \dots, K_{p,\alpha}\}, \quad (2.4a)$$

where $K_{p,\alpha}$ denotes the number of macro particles of kind α . The i -th macro particle of class α consists of

$$N_{i,\alpha} = \int \int_{P_i} f_{\alpha}(\mathbf{x}, \mathbf{p}, t) d^3p d^3x \quad (2.4b)$$

constituents. The first step in discretizing the Maxwell-Vlasov system is to replace the Vlasov equation (2.1) by its characteristic equations (2.2) for the i -th macro particle P_i . These equations thus become:

$$\frac{d\mathbf{x}_i(t)}{dt} = \mathbf{v}_i(t), \quad (2.5a)$$

$$M_i \frac{d\mathbf{U}_i(t)}{dt} = Q_i [\mathbf{E}(\mathbf{x}_i(t), \mathbf{v}_i(t), t) + \mathbf{v}_i(t) \times \mathbf{B}(\mathbf{x}_i(t), \mathbf{v}_i(t), t)], \quad (2.5b)$$

with the relativistic velocity $\mathbf{U} = \gamma \mathbf{v}$, where the Lorentz factor γ is now obtained from $\gamma = \sqrt{1 + \frac{\mathbf{U}^2}{c^2}}$. The mass and charge of the macro particle P_i is calculated from

$$M_i = N_{i,\alpha} m_{\alpha}, \quad (2.5c)$$

$$Q_i = N_{i,\alpha} q_{\alpha}, \quad (2.5d)$$

respectively. It is important to recognize that a macro particle moves in the same way as a single plasma particle, because the ratio $Q_i/M_i = q_\alpha/m_\alpha$ is independent of the number of constituents $N_{i,\alpha}$.

In order to compute the eigenfields generated by the charged macro particles according to (2.3a-d), it is necessary to have an appropriate approximation of the self-consistent charge (2.3 e) and current (2.3 f) density. That means, that the moments of the distribution function f_α

$$\langle v^n \rangle_\alpha := \int v^n f_\alpha(\mathbf{x}, \mathbf{p}, t) d^3p; \quad n = 0, 1 \quad (2.6a)$$

have to be approximated reasonably and, especially, consistently with the underlying physical picture. It is convenient to construct the moments directly from the phase space coordinates of the macro particles. For that purpose, we replace f_α by the discrete distribution function \tilde{f}_α :

$$\tilde{f}_\alpha(\mathbf{x}, \mathbf{p}, t) = \sum_{i=1}^{K_{p,\alpha}} N_{i,\alpha} \delta[\mathbf{x} - \mathbf{x}_i(t)] \delta[\mathbf{p} - \mathbf{p}_i(t)], \quad (2.6b)$$

where δ denotes the usual Dirac function. Inserting the last equation into (2.6a) and performing an additional space averaging, we finally obtain

$$\langle v^n \rangle_\alpha \approx \mathcal{A} \int v^n \tilde{f}_\alpha(\mathbf{x}, \mathbf{p}, t) d^3p, \quad (2.6c)$$

$$\mathcal{A}(\cdot) = \frac{1}{\mathcal{V}_c} \int_{\mathcal{V}_c} \cdot d^3x, \quad (2.6d)$$

for the approximation of the moments. Here, \mathcal{V}_c is the characteristic volume under consideration, which is in practical applications given by the discretization of the physical domain. The additional averaging in (2.6c) by the integral operator (2.6d) is compulsory in order to avoid inconsistencies with the physical model. Assume that a certain number of macro particles are in \mathcal{V}_c which interact according to the Coulomb force. Obviously, such a system is strongly correlated, and consequently the Vlasov description is no longer applicable. The result of the averaging in (2.6c) is that the macro particles are smeared out over the volume \mathcal{V}_c so that Coulomb singularities are avoided.

Applying the averaging process (2.6c) to (2.3e,f) and using the abbreviations

$$\nu_\alpha(\mathbf{x}, t) = \sum_{i=1}^{K_{p,\alpha}} N_{i,\alpha} \delta[\mathbf{x} - \mathbf{x}_i(t)], \quad (2.7a)$$

$$\boldsymbol{\pi}_\alpha(\mathbf{x}, t) = \sum_{i=1}^{K_{p,\alpha}} N_{i,\alpha} \mathbf{v}_{i,\alpha} \delta[\mathbf{x} - \mathbf{x}_i(t)], \quad (2.7b)$$

the self-consistent charge and current density is approximated according to

$$\rho^{sc} \approx \sum_{\alpha} q_\alpha \mathcal{A} \nu_\alpha(\mathbf{x}, t), \quad (2.7c)$$

$$j^{sc} \approx \sum_{\alpha} q_{\alpha} \mathcal{A} \pi_{\alpha}(\mathbf{x}, t), \quad (2.7d)$$

respectively. Direct evaluation of the averaging operator \mathcal{A} leads to an approximation of the source terms at the mesh points where the Maxwell equations (see Section 4) are solved numerically. These special techniques are often called Particle-in-Cell (PIC) methods [4, 22]. The extension of these methods to boundary-fitted coordinates has been realized in the well-established BFCPIC program (see [67] and references therein). The main ideas of the PIC methods for boundary-fitted coordinates as well as the adaptation of these schemes to the data structure of the nonstationary Maxwell equations which depends on the chosen solution method is given in Section 5.

3 Grid Generation

Numerical simulation of physical phenomena in technical devices is not an easy task, because the geometry of such devices can be, in general, very complicated and mixed boundary conditions have to be specified. In order to compute the discrete solution of a practical field problem in an electromagnetic device, it is important to model very accurately the boundaries of the domain and the boundary conditions.

These requirements can be met by using well established grid generation methods based on boundary-fitted coordinates (BFC) [56]. A brief review of the BFC techniques as well as the extension of these methods for our special applications in pulsed power ion diodes [16] is presented. The construction and consequently the geometry recording of technical devices is frequently done with the aid of CAD-systems. The combination of these powerful construction tools with extended BFC concepts we realize in the interactive grid generation module InGrid (**I**nteractive **G**rid generation) [17].

3.1 Boundary-Fitted Coordinates

An adequate computational grid is necessary to compute the discrete solutions for the electromagnetic fields in a complex technical device. The simplest discrete description of a geometry that one can imagine is an equidistant Cartesian monoblock grid with a very obvious data structure: each interior grid point has an upper, a lower, a right, and a left neighbouring point. More flexible is the so-called block-structured grid, where different parts of the geometry are covered by monoblock grids with different fineness. The most flexible discrete description of a geometry is obtained by using unstructured grid techniques. These grids have the highest degree of freedom. These concepts seem to be very powerful as it was demonstrated recently [2], especially, for electromagnetic field problems where an extreme local refinement of zones is required. However, the drawback of these methods is that the data structure is very complicated, and particle treatment (see Section 5) within such a grid is hardly practicable. In addition, the optimization for high performance computers becomes difficult [29].

An interesting alternative to unstructured grids are concepts using boundary-fitted coordinates based either on triangular meshes [35, 69] or on quadrilateral meshes [25, 56, 65]. They are nearly as flexible as unstructured meshes, but have the great advantage that the data structure is regular, and therefore, they are logically equivalent to monoblock grids. The basic idea of the BFC concept, namely the transformation of the physical to the logical area, is represented in Figure 3.1 for the two-dimensional case. The boundary of the physical area in the (x, y) -plane is mapped onto the boundary of a rectangle in the (ξ, η) -plane. An equidistant grid is defined in this rectangle and transformed back to the physical area. In the following, the governing equations of the BFC concept and the numerical procedure

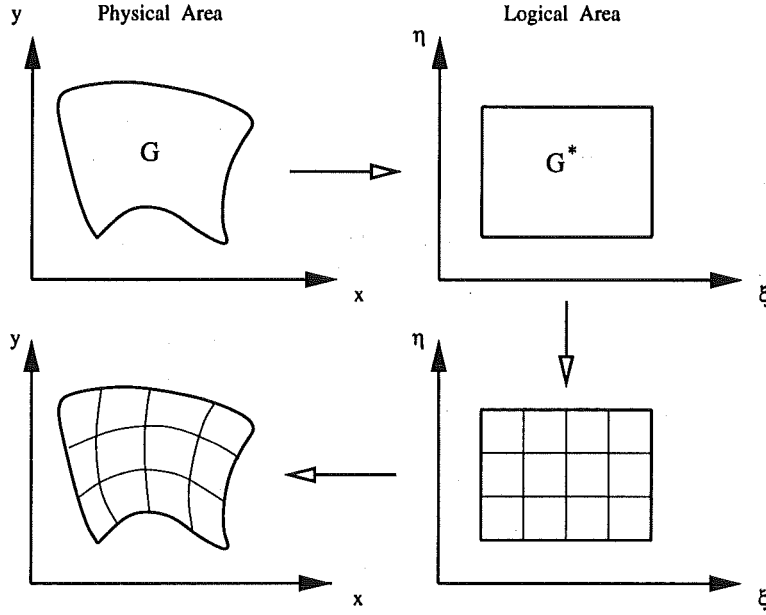


Figure 1: Mesh concept of boundary-fitted coordinates.

for the creation of the computational grid in two dimensions will be discussed (cf. [16, 57, 68]).

The computational grid is generated numerically by solving elliptic partial differential equations. In two dimensions the elliptic system is given by

$$\Delta \xi(x, y) = P, \quad (3.1a)$$

$$\Delta \eta(x, y) = Q, \quad (3.1b)$$

where P and Q are arbitrary functions depending on x and y . The mapping of the physical area in the (x, y) -plane onto the logical area (ξ, η) -plane (cf. Figure 3.1) is established by $\xi(x, y)$, $\eta(x, y)$. Representing the Laplace operator in (3.1) with respect to the coordinates (ξ, η) , the so-called metric \mathbf{g} of the transformation

$$\mathbf{g} = \begin{pmatrix} g_{11} & g_{12} \\ g_{21} & g_{22} \end{pmatrix} = \begin{pmatrix} x_\xi^2 + y_\xi^2 & x_\xi x_\eta + y_\xi y_\eta \\ x_\xi x_\eta + y_\xi y_\eta & x_\eta^2 + y_\eta^2 \end{pmatrix} \quad (3.2a)$$

plays an important role. With that, the inverse maps $x(\xi, \eta)$ and $y(\xi, \eta)$ are obtained from the solution of

$$g^{11} x_{\xi\xi} + 2g^{12} x_{\xi\eta} + g^{22} x_{\eta\eta} + P x_\xi + Q x_\eta = 0, \quad (3.2b)$$

$$g^{11} y_{\xi\xi} + 2g^{12} y_{\xi\eta} + g^{22} y_{\eta\eta} + P y_\xi + Q y_\eta = 0, \quad (3.2c)$$

where the coefficients are the elements of the inverse metric \mathbf{g}^{-1} which is given by

$$\mathbf{g}^{-1} = \begin{pmatrix} g^{11} & g^{12} \\ g^{21} & g^{22} \end{pmatrix} = \frac{1}{|\mathbf{g}|} \begin{pmatrix} x_\eta^2 + y_\eta^2 & -x_\xi x_\eta - y_\xi y_\eta \\ -x_\xi x_\eta - y_\xi y_\eta & x_\xi^2 + y_\xi^2 \end{pmatrix} \quad (3.2d)$$

with the determinant of \mathbf{g}

$$|\mathbf{g}| = (x_\xi y_\eta - x_\eta y_\xi)^2. \quad (3.2e)$$

If the boundary points are specified as Dirichlet points, which means that they are fixed and known, the interior points are uniquely determined by equations (3.2). Hence, solving the discretized Dirichlet problem leads to the coordinates of the grid points $\mathbf{r}_{i-1/2,j-1/2} = (x_{i-1/2,j-1/2}, y_{i-1/2,j-1/2})^T$ in the physical area. Concerning the notation of these points we refer to Figure 3.2. Attraction and repulsion of the grid

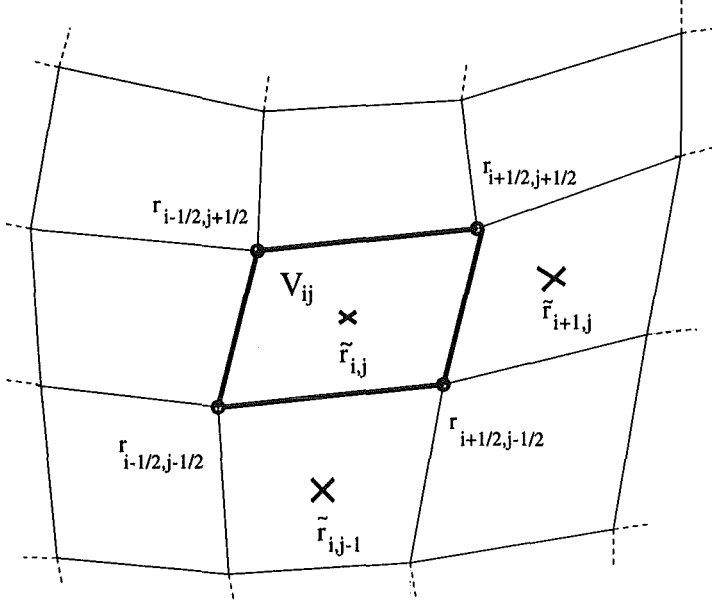


Figure 2: Example of grid notation for the grid cell V_{ij} : $r_{i,j}$ denotes the corners and $\tilde{r}_{i,j}$ is the barycentre of the grid zone.

lines towards specified points or lines can be achieved by specifying the functions P and Q . They control the density of grid lines in the interior of the physical area. Often, P and Q are chosen equal to zero.

The advantages of the elliptic grid generator systems are that the resulting grids are inherently smooth, the danger of overlapping grid lines is small, and they can easily be adapted to general boundary configurations. Furthermore, the concept of elliptic grid generators is not limited to two dimensions and can be extended to three-dimensional applications.

The standard approach of discretizing the equations (3.2) can be summarized as follows. For an equidistant grid in the (ξ, η) -plane, the derivatives in (3.2) are approximated by using central differences, which are second-order accurate with respect to the logical space:

$$(x_\xi)_{i-1/2,j-1/2} \approx \frac{1}{2\Delta\xi}(x_{i+1/2,j-1/2} - x_{i-3/2,j-1/2}), \quad (3.3a)$$

$$(x_\eta)_{i-1/2,j-1/2} \approx \frac{1}{2\Delta\eta}(x_{i-1/2,j+1/2} - x_{i-1/2,j-3/2}), \quad (3.3b)$$

$$(x_{\xi\xi})_{i-1/2,j-1/2} \approx \frac{1}{(\Delta\xi)^2}(x_{i+1/2,j-1/2} - 2x_{i-1/2,j-1/2} + x_{i-3/2,j-1/2}), \quad (3.3c)$$

$$(x_{\eta\eta})_{i-1/2,j-1/2} \approx \frac{1}{(\Delta\eta)^2}(x_{i-1/2,j+1/2} - 2x_{i-1/2,j-1/2} + x_{i-1/2,j-3/2}), \quad (3.3d)$$

$$(x_{\xi\eta})_{i-1/2,j-1/2} \approx \frac{1}{4\Delta\xi\Delta\eta}(x_{i+1/2,j+1/2} - x_{i+1/2,j-3/2} - x_{i-3/2,j+1/2} + x_{i-3/2,j-3/2}). \quad (3.3e)$$

The same discretization is used for y . The grid equations (3.2b), (3.2c) can be discretized according to (3.3) yielding at every grid point $r_{i,j}$ an equations of the form

$$\sum_{l=i-3/2}^{i+1/2} \sum_{m=j-3/2}^{j+1/2} c_{lm} A_{lm} = 0, \quad (3.4a)$$

where the coefficients c_{lm} are given by

$$\begin{aligned} c_{i-3/2,j-3/2} = c_{i+1/2,j+1/2} &= -c_{i+1/2,j-3/2} = -c_{i-3/2,j+1/2} = \frac{\Delta\xi\Delta\eta}{2} g^{12}, \\ c_{i-1/2,j-1/2\mp 1} &= (\Delta\xi)^2 \left[g^{22} \mp \frac{\Delta\eta}{2} Q \right], \\ c_{i-1/2\mp 1,j-1/2} &= (\Delta\eta)^2 \left[g^{11} \mp \frac{\Delta\xi}{2} P \right], \\ c_{i-1/2,j-1/2} &= -2 \left[(\Delta\eta)^2 g^{11} + (\Delta\xi)^2 g^{22} \right]. \end{aligned} \quad (3.4b)$$

The finite difference equation (3.4) is solved together with the Dirichlet boundary values by means of nonlinear SOR [22, 44, 54] or ad-hoc SOR [13] iteration schemes. In certain cases it may be possible that a more efficient multigrid scheme [42, 62] could be used.

3.2 Extended Grid Generation Strategies

As mentioned above the first idea of grid generation is to map a computational domain G , the so-called physical region in the (x, y) -plane, to a rectangle G^* , the so-called logical region in the (ξ, η) -plane. The inverse image of a regular monoblock grid in G^* thus becomes a boundary-fitted grid in G (Figure 3.1). However, this kind of grid generation is not applicable to all conceivable technical field problems, since there are multiply-connected regions and regions containing internal boundaries as well. Even in the case of simply-connected regions and using the possibilities of internal grid control via the functions P and Q in (3.1), the basic grid generation techniques summarized above does not always deliver reasonable grids.

A first extension of the basic concept is the introduction of a point attribute structure. Each grid point is supplied with an attribute. The location of a grid point

on a specified part of the boundary of G can be expressed by an associated value of its attribute. Thus G need no longer be the inverse image of a rectangle. For practical purposes, however, the image of G is embedded into a rectangle. The point attributes are used not only to fix grid points at the different parts of the boundary ∂G of G , but also to assign the different kinds of boundary conditions specified on ∂G . For most technical field problems suitable grids can be designed within this concept. Also multiply-connected regions need not be cut and internal boundaries can be easily taken into account [16].

Further aspects of extending the grid generation concepts in an appropriate manner, especially, if domains with very complex configurations should be handled or for field problems with highly varying demands of accuracy have to be considered. Strong distortions of the grid are often caused by the attempt to create a common grid in the entire computational region. Obviously, it could be of great advantage to design independently several grids for different parts of the physical domain. Therefore, a clever partition of the domain can particularly improve the grid generation process. Furthermore, it is possible to avoid internal boundaries for some grids if appropriate partitioning is performed and consequently highly efficient numerical procedures for field computations can be applied. In respect of modern parallel strategies in field computation, domain decomposition concepts seem to be very attractive. The power of computers with parallel processor architecture may be effectively used if the computational region is divided in a large number of parts, for example, according to obvious sub-domains with the corresponding BFC grids. However, some additional effort is necessary for the application of these grid generation methods: branch cut handling in the physical space as well as the connection of the field solvers on adjacent or overlapping sub-regions.

3.3 Interactive Grid Generation with InGrid

From a practical point of view, grid generation for technical field calculations is often cumbersome and time consuming. In order to achieve the desired accuracy in mapping the geometry, one requires an acceptable representation of the boundary of the considered domain, good control of the grid fineness and the avoidance of strong distortions of the grid. A suitable way to record the geometry of a technical device is to use one of the widespread CAD-systems. A new strategy combining this powerful construction tool (with all its auxiliaries like ZOOM-functions, etc.) directly with BFC grid generation techniques was recently proposed in [17] and enables us now to generate a computational grid in two dimensions in a very effective and comfortable manner. An appropriate CAD-system which satisfies our requirements is the well established AutoCAD system (version 12). This is a so-called open software tool which allows us to refer to self-written routines, necessary for the grid generation and optimization. The interplay of AutoCAD with extended BFC grid generation concepts is realized in the program package InGrid (**I**nteractive **G**rid generation) which is at the stage of preparation for distribution [18].

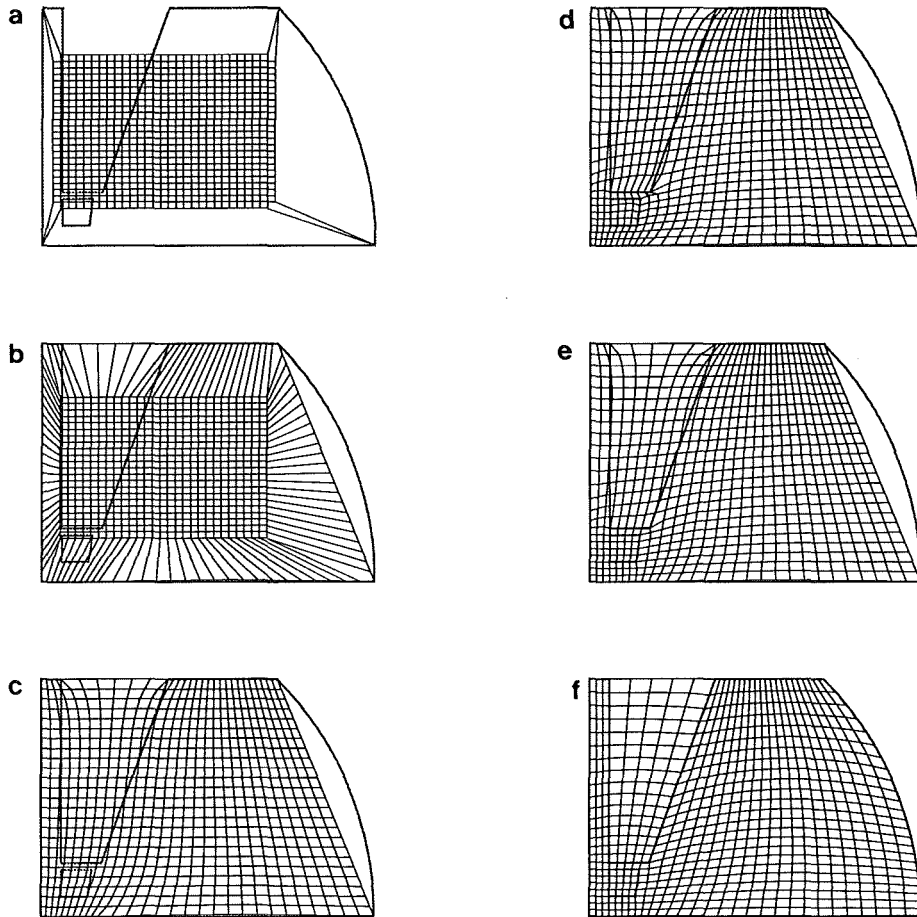


Figure 3: Interactive grid generation performed with the program InGrid. The sequence of intermediate steps usually seen on the screen, gives information about the numerous optional function keys available in and the advance of InGrid to generate a boundary-fitted grid.

The general operation method of the InGrid module is illustrated in Figure 3.3, where several grid generation steps for a special device are shown. The geometry is relatively simple and the generated grid is rather coarse, but nevertheless this example show the principal modes of operation of InGrid. First, a simple rectangular grid is posed optionally within the computational domain (Figure 3.3a). After pulling the four corners of this grid to appropriate positions, inner grid lines must be brought successively to coincidence with the border of the computational domain. Smoothing of the grid edges and the subsequent smoothing of the entire grid is shown in Figure 3.3b and 3.3c. Often numerical methods require that inner structures of the computational domain coincide with grid lines. This implies that single grid points, or sometimes, whole grid lines have to be projected onto these structures as is depicted in Figure 3.3d. Undesired distortions of the grid can influence effectively the accuracy and robustness of the applied numerical schemes. The disadvantageous run of the grid lines in Figure 3.3e can be removed if one grid line is pulled out of the right border of the distinct upper inner structure. After repeated relaxation and

appropriate mapping of the grid lines onto the border of the computational domain the boundary-fitted grid generation is finished (Figure 3.3f).

The essential advantages of the new grid generation module InGrid can be summarized as follows: In general, it turns out that the time spent on generating a computational grid becomes reasonably small. Since the grid generation is performed interactively, each intermediate step can be evaluated on the screen and suitable actions for a further optimization of the grid can be done directly. Therefore, it is planned for the future that this interactive method is put into action to generate the computational grid in a standardized way for all ion diodes under consideration. A modified version of InGrid which considers the special data structure of the BFCPIC code is now available.

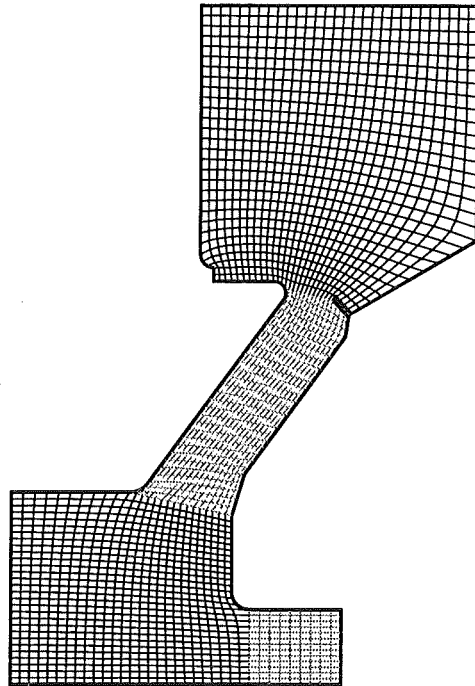


Figure 4: Interactive grid generation with InGrid for the B_{appl} ion diode. The computational grid consists of four different monoblock grids.

A typical use of InGrid for our special application of pulsed power ion diodes is depicted in Figure 3.4. The shown grid was created by InGrid after the domain was decomposed into four parts. Obviously, Figure 3.4 demonstrates the efficiency of the new grid generation technique for very complex geometries and the requirement of fine grid zones.

4 Numerical Concepts for the Maxwell Equations

A large variety of numerical methods are available for electromagnetic field computations [71]. A well established concept for the numerical solution of the field equations (2.3) in the context of plasma simulations is based on finite-difference (FD) methods on staggered grids [8]. A brief review of these FD methods is given in the second part of this section.

A new approach for numerically attacking the nonstationary Maxwell equations is based on high resolution finite-volume (FV) methods, originally developed in the context of computational fluid dynamics and hyperbolic partial differential equations [30]. The basic ideas of this approach for quadrilateral grids will be discussed in the first part of this section.

To obtain a discrete algebraic approximation of the nonstationary Maxwell equations (2.3a), (2.3b), the common starting point for the FD as well as the FV methods are the Maxwell curl equations written in the form (see Appendix A)

$$\partial_t u + \sum_{i=1}^3 \mathcal{K}_i \partial_{x_i} u = q(u) \quad (4.1a)$$

with the usual abbreviations $\partial_t = \frac{\partial}{\partial t}$ and $\partial_{x_i} = \frac{\partial}{\partial x_i}$, $i = 1, 2, 3$. The notation of the coordinates is $(x_1, x_2, x_3) = (x, y, z)$ and $(x_1, x_2, x_3) = (z, r, \varphi)$ for the Cartesian and the cylindrical system, respectively. Here, u denotes the vector of the conserved quantities established by the electric field and magnetic induction according to

$$u = (E_1, E_2, E_3, B_1, B_2, B_3)^T. \quad (4.1b)$$

The block-structured matrices $\mathcal{K}_i \in \mathbb{R}^{6 \times 6}$ are defined as

$$\mathcal{K}_i = \begin{pmatrix} \mathbf{0} & -c^2 \mathcal{M}_i \\ \mathcal{M}_i & \mathbf{0} \end{pmatrix}; \quad i = 1, 2, 3, \quad (4.1c)$$

where c denotes the velocity of light and the matrices $\mathcal{M}_i \in \mathbb{R}^{3 \times 3}$ are given by

$$\mathcal{M}_1 = \begin{pmatrix} 0 & 0 & 0 \\ 0 & 0 & -1 \\ 0 & 1 & 0 \end{pmatrix}, \quad \mathcal{M}_2 = \begin{pmatrix} 0 & 0 & 1 \\ 0 & 0 & 0 \\ -1 & 0 & 0 \end{pmatrix}, \quad \mathcal{M}_3 = \frac{1}{x_2^\kappa} \begin{pmatrix} 0 & -1 & 0 \\ 1 & 0 & 0 \\ 0 & 0 & 0 \end{pmatrix}. \quad (4.1d)$$

Here, the value of κ allows to write the equations for both the Cartesian and rotationally symmetrical case in compact form. Since the problems of interest should be solved for Cartesian ($\kappa = 0$) or cylindrically symmetric ($\kappa = 1$) geometries, the right-hand side (rhs) of (4.1a) is determined from

$$q(u) = -c^2 \mu_0 (J_1, J_2, J_3, 0, 0, 0)^T + \frac{\kappa}{x_2} (c^2 B_3, 0, 0, -E_3, 0, 0)^T, \quad (4.1e)$$

where μ_0 is the permeability of free space. In addition to the physical current densities $J_i = j_i^{sc} + j_i^{ext}$, the vector of the source terms $q(u)$ contains additionally

a geometric term with $\kappa = 1$ in the case of cylindrical coordinates. For Cartesian coordinates this term vanishes because $\kappa = 0$.

At the first stage of the Maxwell-Lorentz code development we restrict ourselves to a $2\frac{1}{2}$ -dimensional version. This means, that we assume the conserved quantities u to be independent of x_3 and, consequently, $\partial_{x_3}u = 0$. In that case, only the matrices \mathcal{K}_i , $i = 1, 2$, appear, which are constant and independent of the symmetry of the underlying physical problem.

4.1 Finite-Volume Approach

A finite-volume scheme for the Maxwell equations is an approximation of the integral form of the system (4.1a). At first we rewrite these equations into a system of conservation laws

$$\partial_t u + \operatorname{div} \mathcal{F}(u) = q(u) \quad (4.2a)$$

with the matrix

$$\mathcal{F}(u) = (\mathcal{K}_1 u, \mathcal{K}_2 u, \mathcal{K}_3 u) \in \mathbb{R}^{6 \times 3}, \quad (4.2b)$$

where the divergence of $\mathcal{F}(u)$ has to be interpreted columnwise:

$$\operatorname{div} \mathcal{F}(u) = \sum_{i=1}^3 \partial_{x_i} (\mathcal{K}_i u) = \begin{pmatrix} \sum_{i=1}^3 \partial_{x_i} \left(\sum_{j=1}^6 (\mathcal{K}_i)_{1,j} u_j \right) \\ \vdots \\ \sum_{i=1}^3 \partial_{x_i} \left(\sum_{j=1}^6 (\mathcal{K}_i)_{6,j} u_j \right) \end{pmatrix}. \quad (4.2c)$$

For the following considerations we restrict ourselves to the two-dimensional situation and assume that the physical area G is covered by a quadrilateral grid $V = \cup_{i,j} V_{ij}$ (cf. Figure 3.1 and 3.2) with the individual grid zones V_{ij} . Integrating each equation of (4.2a) over the space-time volume $V_{ij} \times [t_n, t_{n+1}]$, the following system of integral equations is obtained

$$\int_{t_n}^{t_{n+1}} \int_{V_{ij}} \partial_t u \, dV \, dt = - \int_{t_n}^{t_{n+1}} \int_{V_{ij}} \operatorname{div} \mathcal{F}(u) \, dV \, dt + \int_{t_n}^{t_{n+1}} \int_{V_{ij}} q(u) \, dV \, dt. \quad (4.3a)$$

Interchanging integration and differentiation on the left-hand side (lhs) and defining the cell average u_{ij} of u in the cell zone V_{ij} with the area $|V_{ij}|$ according to

$$u_{ij}(t) = \frac{1}{|V_{ij}|} \int_{V_{ij}} u(x, t) \, dV, \quad (4.3b)$$

the time-integration on the lhs can be performed directly. The first expression on the rhs of (4.3a) can be transformed to a line integral applying the Gauss's theorem. Furthermore using u_{ij}^n instead of $u_{ij}(t_n)$, equation (4.3a) finally reads as

$$u_{ij}^{n+1} = u_{ij}^n - \frac{1}{|V_{ij}|} \int_{t_n}^{t_{n+1}} \oint_{\partial V_{ij}} \mathcal{F}(u) n_{ij} \, dS \, dt + \frac{1}{|V_{ij}|} \int_{t_n}^{t_{n+1}} \int_{V_{ij}} q(u) \, dV \, dt, \quad (4.3c)$$

where $n_{ij} \in \mathbb{R}^2$ is the outer unit normal at the boundary ∂V_{ij} of the grid zone V_{ij} . As it is sketched out in Figure 4.1, the boundary of a quadrilateral grid cell is given by $\partial V_{ij} = \sum_{\beta=1}^4 S_{ij,\beta}$ and, therefore the line integral can be replaced by

$$\oint_{\partial V_{ij}} \mathcal{F}(u) n_{ij} dS = \sum_{\beta=1}^4 \int_{S_{ij,\beta}} \mathcal{F}(u) n_{ij,\beta} dS, \quad (4.3d)$$

where $n_{ij,\beta} = (n_{ij,\beta}^{(1)}, n_{ij,\beta}^{(2)})^T$ denotes the outwards directed unit normal at the edge $S_{ij,\beta}$. The integral equations (4.3c) establish the evolution equations for the integral

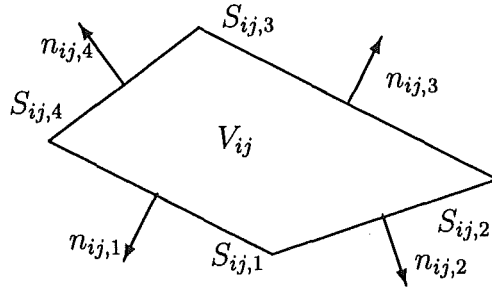


Figure 1: Grid cell V_{ij} of the quadrilateral grid $V = \cup_{ij} V_{ij}$

mean values u_{ij}^n . A finite-volume scheme is the direct approximation of the integral equations (4.3c) and is usually written in the form

$$u_{ij}^{n+1} = u_{ij}^n - \frac{\Delta t}{|V_{ij}|} \sum_{\beta=1}^4 G_{ij,\beta}^n + \Delta t q_{ij}^n, \quad (4.4a)$$

where $G_{ij,\beta}^n$ is the so-called numerical flux through the boundary segment $S_{ij,\beta}$ at the time level t_n and given as an approximation of the physical flux:

$$G_{ij,\beta}^n \approx \int_{S_{ij,\beta}} \mathcal{F}(u^n) n_{ij,\beta} dS. \quad (4.4b)$$

The vector q_{ij}^n approximates the source terms averaged over V_{ij} and the time interval $[t_n, t_{n+1}]$. Obviously, the main task in this connection is to find a suitable estimation of the numerical flux (4.4b) from the knowledge of the averaged conserved quantities. In order to construct an explicit FV scheme, only the quantities u_{ij}^n at the time level t_n should be used. The basic ideas to overcome this problem are briefly reviewed in the next subsection for a one-dimensional situation.

4.1.1 Solution of the Riemann Problem and the Flux Approximation

The key problem in developing efficient FV schemes is to find an appropriate numerical flux $G_{ij,\beta}^n$. For the sake of clarity, we discuss the principle features of the approximation process for the one-dimensional case under the assumption that the source

terms vanish, originally conceived by Godunov [15]. The situation on hand for a certain time level t_n is illustrated in Figure 4.2: in each grid zone $I_i = [x_{i-1/2}, x_{i+1/2}]$ we define $u^n(x)$ to be constant and given by the cell average u_i^n . This corresponds to a piecewise constant reconstruction of the solution from the integral values u_i^n and results in piecewise constant initial values for the following time step. As time proceeds, the jumps at the grid zone interfaces will break up and give rise to locally propagating waves as schematically depicted in the upper part of Figure 4.2. By constructing high resolution FV schemes the information of the local wave propagation structure of the problem is incorporated into the numerical solution. The structure of the problem may be obtained by solving local Riemann problems (RP).

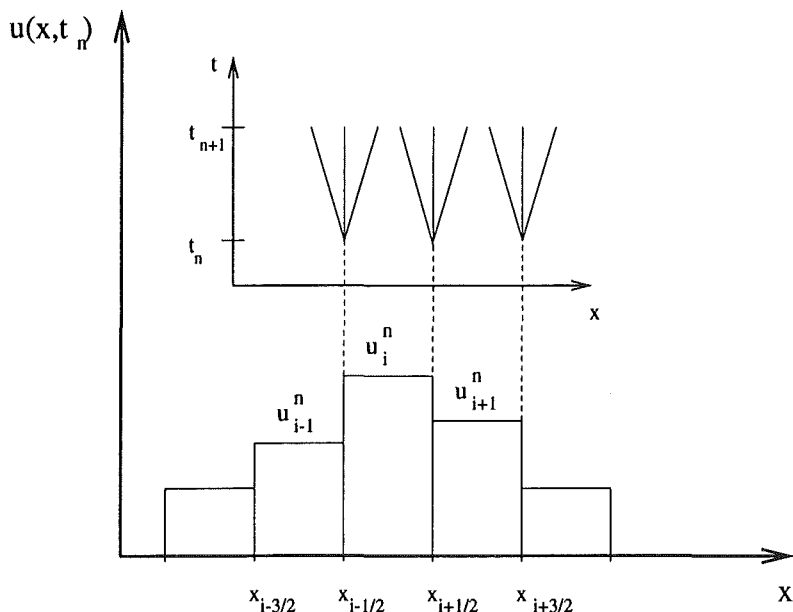


Figure 2: Piecewise constant initial data and (x, t) -diagrams of the schematic solution of local Riemann problems at the grid zone interfaces

The one-dimensional RP is an initial-value problem for the homogenous conservation law

$$\partial_t u + \partial_x F(u) = 0 \quad (4.5a)$$

with the piecewise constant initial data

$$u_0(x) = \begin{cases} u_L & x < 0 \\ u_R & x > 0 \end{cases} \quad (4.5b)$$

In the following we will review the solution procedure for a general case and specify the formulas for the Maxwell equations in Appendix D. With respect to the linear hyperbolic Maxwell equations, we restrict ourselves to the linear case where $F(u)$ is given by

$$F(u) = \mathcal{A}u, \quad (4.5c)$$

with $\mathcal{A} \in \mathbb{R}^{m \times m}$. If the matrix \mathcal{A} has a complete set of eigenvectors, the one-dimensional linear RP (4.5) can be solved exactly, applying the theory of characteristics (see, e.g., [30]). The solution consists of $m + 1$ constant states

$$u(x, t) = \begin{cases} u_0 & -\infty < \frac{x}{t} < \lambda_1 \\ \vdots & \\ u_k & \lambda_k < \frac{x}{t} < \lambda_{k+1} \\ \vdots & \\ u_m & \lambda_m < \frac{x}{t} < \infty \end{cases}, \quad (4.6a)$$

where $\lambda_1, \dots, \lambda_m$ denote the m eigenvalues of \mathcal{A} with $\lambda_1 \leq \lambda_2 \leq \dots \leq \lambda_m$ and $u_0 = u_L$, $u_m = u_R$. If $\lambda_n = \lambda_{n+1}$, the two states u_n and u_{n+1} coincide. As it is shown in Figure 4.3, the $m + 1$ constant states are separated by m elementary waves. An elegant way

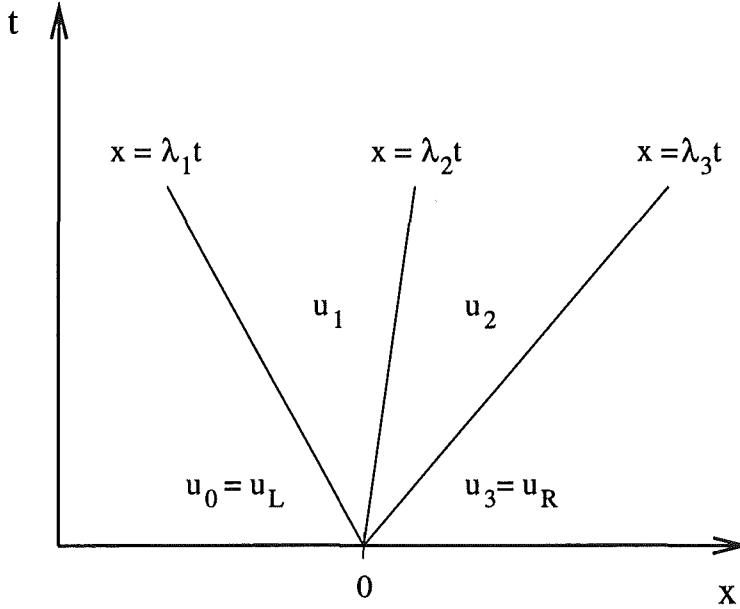


Figure 3: Solution of the one-dimensional, linear Riemann problem in the (x, t) -plane for $m=3$

to obtain the intermediate states u_1, u_2, \dots, u_{m-1} , is to decompose the jump $u_R - u_L$ into the sum of jumps across the curves $x = \lambda_j t$:

$$u_R - u_L = \sum_{j=1}^m \alpha_j r^j, \quad (4.6b)$$

where the r^j , $j = 1, \dots, m$, are the right eigenvectors of \mathcal{A} . Obviously, (4.6b) is a linear system of equations from which the coefficients α_j can be calculated. The constant states could be determined from

$$u_k = u_L + \sum_{j=1}^k \alpha_j r^j, \quad (4.6c)$$

or, alternatively, from

$$u_k = u_R - \sum_{j=0}^{m-k-1} \alpha_{m-j} r^{m-j}, \quad (4.6d)$$

where k runs from $k = 0, \dots, m$.

With the index sets $J_1 = \{j | \lambda_j < 0\}$ and $J_2 = \{j | \lambda_j > 0\}$, the solution of the RP at $x = 0$ is given by

$$\begin{aligned} u(0, t) &= u_L + \sum_{j \in J_1} \alpha_j r^j \\ &= u_R - \sum_{j \in J_2} \alpha_j r^j. \end{aligned} \quad (4.7a)$$

We note that $u(0, t)$ is independent of t , and hence, the flux at $x = 0$ is simply determined according to (4.5a) resulting in $\mathcal{A}u(0, t)$. Using (4.7a) it may be formulated as

$$\begin{aligned} F(u(0, t)) = \mathcal{A}u(0, t) &= \mathcal{A}u_L + \sum_{j \in J_1} \alpha_j \lambda_j r^j \\ &= \mathcal{A}u_R - \sum_{j \in J_2} \alpha_j \lambda_j r^j, \end{aligned} \quad (4.7b)$$

or, alternatively, with the arithmetic average of both expressions we obtain

$$\begin{aligned} F(u(0, t)) = \mathcal{A}u(0, t) &= \frac{1}{2} \mathcal{A}(u_L + u_R) - \frac{1}{2} \sum_{j=1}^m \alpha_j |\lambda_j| r^j \\ &= \frac{1}{2} \mathcal{A}(u_L + u_R) - \frac{1}{2} |\mathcal{A}| (u_R - u_L). \end{aligned} \quad (4.7c)$$

The idea of Godunov was to define the numerical fluxes of the FV scheme (4.4), which reads in one space dimension as

$$u_i^{n+1} = u_i^n - \frac{\Delta t}{\Delta x} (G_{i+1/2}^n - G_{i-1/2}^n), \quad (4.8)$$

to be the physical fluxes of the corresponding RP as given by (4.7c). With the definition

$$\mathcal{A}^\pm = \frac{1}{2} (\mathcal{A} \pm |\mathcal{A}|), \quad (4.9a)$$

the numerical flux can be written in the compact form

$$G_{i+1/2}^n = G(u_i^n, u_{i+1}^n) = \mathcal{A}^+ u_L + \mathcal{A}^- u_R. \quad (4.9b)$$

By the use of the RP solution the wave propagation is incorporated into the numerical approximation. Furthermore, the only approximation within the Godunov scheme in one spatial dimension is the approximation of the exact solution by a piecewise constant function. Except for this interpolation function, all other calculations are exact. Since in the flux calculation no smoothness of the solution is

assumed, the Godunov scheme is extraordinarily robust in regions where large gradients occur, or even if the solution is discontinuous. The Godunov scheme was developed originally for the equations of gas dynamics, in particular, to capture shock waves. For a more detailed description we refer to [30]. The accuracy of the Godunov scheme may be improved by replacing the piecewise constant distribution by a more structured one. This will be discussed in Section 4.1.3. For the Maxwell equations the relevant quantities such as α_j , r^j , \mathcal{A}^\pm , etc. are listed in Appendix D.

4.1.2 Two-dimensional FV Scheme on Structured Quadrilateral Grids

We now consider the Godunov scheme in two spatial dimensions. The grid covering the physical area consists of quadrilateral grid zones V_{ij} as illustrated in Figure 3.2. The advantage in constructing FV schemes for the conservation laws (4.2a), is that the approximation is directly performed in the physical area and no transformation of the equations to the logical domain is necessary (cf. Figure 3.1). Again, we assume that the solution is approximated by a piecewise constant function in each grid zone. To define the FV method, the numerical fluxes have to be specified in the evolution equation for the integral values (4.4). Therefore, we first assume the source terms to be zero. Then the integral over the boundary segments is approximated by the midpoint rule yielding the flux in normal direction at the midpoint $x = x_{MP,\beta}$ of $S_{ij,\beta}$ multiplied by the length $|S_{ij,\beta}|$ of this edge:

$$G_{ij,\beta}^n = |S_{ij,\beta}| \left(n_{ij,\beta}^{(1)} \mathcal{K}_1 + n_{ij,\beta}^{(2)} \mathcal{K}_2 \right) u(x_{MP,\beta}, t_n). \quad (4.10)$$

The value $u(x_{MP,\beta}, t_n)$ is obtained by solving locally the RP in the normal direction along the coordinate ζ . Similar to the RP (4.5) we find

$$\partial_t u + \mathcal{C}_{ij,\beta} \partial_\zeta u = 0, \quad (4.11a)$$

$$u(\zeta, 0) = \begin{cases} u_L & \text{for } \zeta < 0 \\ u_R & \text{for } \zeta > 0 \end{cases}, \quad (4.11b)$$

with

$$\mathcal{C}_{ij,\beta} = n_{ij,\beta}^{(1)} \mathcal{K}_1 + n_{ij,\beta}^{(2)} \mathcal{K}_2. \quad (4.11c)$$

This local consideration seems to be evident as long as no waves from the neighboring interfaces disturb the RP solution at $\zeta = 0$, which introduce the natural time step size restriction. Defining the matrices

$$C_{ij,\beta} = |S_{ij,\beta}| \mathcal{C}_{ij,\beta}, \quad (4.12a)$$

the numerical flux can be calculated analogously to the one-dimensional case and is obtained from

$$G_{ij,\beta} = C_{ij,\beta}^+ u_{L,\beta} + C_{ij,\beta}^- u_{R,\beta}, \quad (4.12b)$$

where $u_{L,\beta}$ and $u_{R,\beta}$ are given by

$$u_{L,\beta} = u_{ij}^n \quad \forall \beta, \quad (4.12c)$$

$$u_{R,\beta} \in \{u_{i,j-1}^n, u_{i+1,j}^n, u_{i,j+1}^n, u_{i-1,j}^n\}. \quad (4.12d)$$

The explicit form of the matrices $C_{ij,\beta}^\pm$ and $C_{ij,\beta}$ is found in Appendix D. Since the flux calculation (4.12) is based on values at the old time level t_n the two-dimensional scheme (4.4) is an explicit FV scheme. Calculating the numerical fluxes according to (4.12b), we directly take into account the local wave structure of the solution of the one-dimensional linear hyperbolic conservation laws (4.11), responsible for the robustness of these schemes. The formulas of a two-dimensional FV scheme for the situation where the underlying grid is Cartesian becomes much simpler and are given for completeness in Appendix B.

Up to now we assumed the source term q to be zero. In the nonzero case the averaged source term vector q_{ij}^n is incorporated into the scheme by applying a splitting method described by Marchuk in [34]. In a first step we solve the homogeneous Maxwell equations (4.2a), which means, q_{ij}^n is neglected in (4.4a). After this transport step, we take into account the influence of the source term vector. Therefore, we have to solve numerically the system of ordinary differential equations

$$\frac{du}{dt} = q(u), \quad (4.13)$$

with standard methods (see, e.g. [44]), where the initial values are provided by the solution of the homogeneous conservation laws.

4.1.3 Extention to higher order accuracy

So far, the FV schemes considered above are only first-order accurate in space and time. However, for most practical applications it is necessary to have at least a second-order accurate method. The basic idea behind the extension is that the accuracy of the arguments of the flux $\mathcal{F}(u)$ are improved instead of the flux \mathcal{F} itself. In the following, the principle features of accuracy improvement of a FV scheme will be briefly explained.

In one dimension, there is a well known extension to second-order accuracy, namely, the so-called MUSCL-schemes (Monotonic-upwind-schemes for conservation laws) proposed by van Leer [27]. The second-order is achieved by taking the distribution of the states to be piecewise linear rather than constant, to this compare Figure 4.2 and 4.4. The RP is then solved with the values extrapolated to the edges of the grid cell. The basic ideas of the procedure for the one-dimensional problem should now be explained in more detail. First, an appropriate approximation of the slope s_i^n within $[x_{i-1/2}, x_{i+1/2}]$ is needed; how to get this will be described later. With this slope, the values of $u(x, t)$ at the left and right cell edge can be approximated. Considering for simplicity an equidistant grid with cells of length Δx , the values are given by

$$u_{i\pm}^n = u_i^n \pm \frac{\Delta x}{2} s_i^n. \quad (4.14a)$$

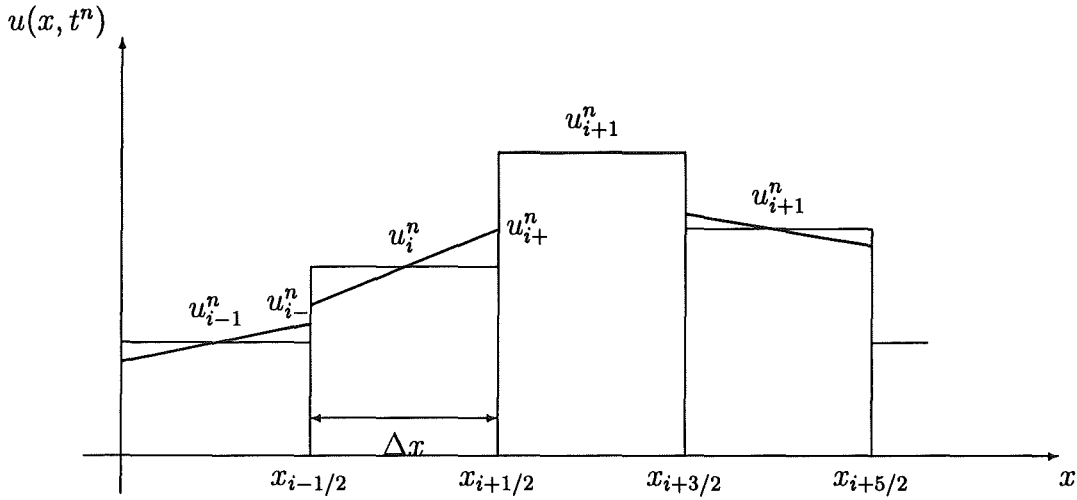


Figure 4: Piecewise linear distribution of the states in the one-dimensional case

To achieve second-order accuracy also in time, it is necessary to approximate the values at time $t_{n+1/2}$

$$u_{i\pm}^{n+1/2} = u_{i\pm}^n + \frac{\Delta t}{2} (\partial_t u)_i^n, \quad (4.14b)$$

where $(\partial_t u)_i^n$ should be an approximation of $\partial_t u$ in cell i at time t_n . Using the differential equation (cf. (4.5))

$$\partial_t u = -\mathcal{A} \partial_x u, \quad (4.14c)$$

an appropriate approximation will be

$$(\partial_t u)_i^n = -\mathcal{A} s_i^n, \quad (4.14d)$$

resulting in

$$u_{i\pm}^{n+1/2} = u_i^n \pm \frac{\Delta x}{2} \left(1 \mp \frac{\Delta t}{\Delta x} \mathcal{A} \right) s_i^n. \quad (4.14e)$$

With these extrapolated values the RP (4.5) is solved and the numerical fluxes are computed according to (4.9b), where $u_L = u_{i+}^{n+1/2}$ and $u_R = u_{(i+1)-}^{n+1/2}$.

The slope s_i^n has to be a first-order approximation of $\partial_x u(x_i, t_n)$ and should possess some monotonicity preserving properties. A more detailed review about slope calculation is given in [30, 38]. For our purposes, we estimate the slopes s_i^n from

$$s_i^n = \frac{1}{\Delta x} \text{SIGN}(a) \text{MAX} \{ |\text{minmod}(ka, b)|, |\text{minmod}(a, kb)| \}, \quad (4.15a)$$

with

$$a = u_{i+1}^n - u_i^n; \quad b = u_i^n - u_{i-1}^n, \quad (4.15b)$$

and

$$\text{minmod}(\alpha, \beta) = \begin{cases} \alpha & \text{if } |\alpha| < |\beta| \text{ and } \alpha\beta > 0 \\ \beta & \text{if } |\alpha| \geq |\beta| \text{ and } \alpha\beta > 0 \\ 0 & \text{if } \alpha\beta \leq 0 \end{cases} . \quad (4.15c)$$

Here, k is an arbitrary constant which can be chosen between one and two. This slope calculation leads to a second-order accurate scheme which is total variation diminishing (TVD). This means, that no new extrema are generated and the absolute values of the actual extrema do not increase [30, 38].

The question arise how the one-dimensional MUSCL-approach can be transferred to our two-dimensional problem on boundary-fitted coordinates. Therefore, we follow the ideas proposed by Collela [10] and proceed in two steps: First, we consider the construction of a second-order accurate FV scheme on two-dimensional Cartesian grids. In the second step, we will see how these principles can be transposed to boundary-fitted grids.

To demonstrate the ideas of the two-dimensional Cartesian MUSCL-ansatz, we start from the two-dimensional linear hyperbolic system (4.2a) where the rhs is neglected

$$\partial_t u + \mathcal{K}_1 \partial_x u + \mathcal{K}_2 \partial_y u = 0 , \quad (4.16a)$$

and assume that the first-order accurate scheme

$$u_{i,j}^{n+1} = u_{i,j}^n - \frac{\Delta t}{\Delta x} (g_{i+1/2,j} - g_{i-1/2,j}) - \frac{\Delta t}{\Delta y} (h_{i,j+1/2} - h_{i,j-1/2}) , \quad (4.16b)$$

is given. Here, $g_{i+1/2,j} = g(u_{i,j}^n, u_{i+1,j}^n)$ and $h_{i,j+1/2} = h(u_{i,j}^n, u_{i,j+1}^n)$ are the numerical fluxes in x - and y -direction, respectively, and are found explicitly in Appendix B. The extrapolated values of $u_{i,j}^n$ in the x - and y -directions (see Figure 4.4) are obtained in a very similar way to those in the one-dimensional case. For the sake of clarity, we outline the approximation procedure in the x -direction more explicitly. According to (4.14b) we calculate the second-order accurate values in space $\hat{u}_{i\pm,j}^{n+1/2}$, $\hat{u}_{i,j\pm}^{n+1/2}$, where the slopes $(s_x)_{i,j}^n$ and $(s_y)_{i,j}^n$ are realized by the minmod-limiter (4.15). Being also second-order accurate in time, we use (4.16a) and replace $\partial_t u$ by $-\mathcal{K}_1 \partial_x u - \mathcal{K}_2 \partial_y u$ and approximate immediately $\mathcal{K}_1 \partial_x u$ by $\mathcal{K}_1 (s_x)_{i,j}^n$. Taking into account the values $u_{i,j}^n$, we approximate the dimensionality influence term $\mathcal{K}_2 \partial_y u$ according to

$$\mathcal{K}_2 \partial_y u \approx \frac{1}{\Delta y} [h(u_{i,j}^n, u_{i,j+1}^n) - h(u_{i,j-1}^n, u_{i,j}^n)] . \quad (4.17a)$$

Hence, with the last equation the appropriate approximation of $\partial_t u$ in the cell zone $V_{i,j}$ at t_n is obtained from

$$\partial_t u \approx -\mathcal{K}_1 (s_x)_{i,j}^n - \frac{1}{\Delta y} [h(u_{i,j}^n, u_{i,j+1}^n) - h(u_{i,j-1}^n, u_{i,j}^n)] . \quad (4.17b)$$

With the abbreviation

$$u_{i\pm,j}^{n+1/2} = u_{i,j}^n \pm \frac{\Delta x}{2} \left(1 \mp \frac{\Delta t}{\Delta x} \mathcal{K}_1\right) (s_x)_{i,j}^n , \quad (4.18a)$$

we finally find for the two-dimensional second-order time and space accurate conserved quantity in the x -direction

$$\hat{u}_{i\pm,j}^{n+1/2} = u_{i\pm,j}^{n+1/2} \mp \frac{\Delta t}{2\Delta y} \left[h(u_{i,j}^n, u_{i,j+1}^n) - h(u_{i,j-1}^n, u_{i,j}^n) \right] \quad (4.18b)$$

Treating the y -direction analogously, we obtain

$$u_{i,j\pm}^{n+1/2} = u_{i,j}^n \pm \frac{\Delta y}{2} \left(1 \mp \frac{\Delta t}{\Delta y} \mathcal{K}_2 \right) (s_y)_{i,j}^n, \quad (4.19a)$$

$$\hat{u}_{i,j\pm}^{n+1/2} = u_{i,j\pm}^{n+1/2} \mp \frac{\Delta t}{2\Delta x} \left[g(u_{i,j}^n, u_{i+1,j}^n) - g(u_{i-1,j}^n, u_{i,j}^n) \right]. \quad (4.19b)$$

The values \hat{u} can be interpreted as values which are one-dimensional second-order in space and time corrected by a term describing the influence of the second dimension. Inserting the (4.18b), (4.19b) as arguments into the Lipschitz continuous fluxes g and h , we obtain the following extended FV scheme from the two-dimensional MUSCL-ansatz

$$\begin{aligned} u_{i,j}^{n+1} = u_{i,j}^n & - \frac{\Delta t}{\Delta x} \left[g(\hat{u}_{i+,j}^{n+1/2}, \hat{u}_{(i+1)-,j}^{n+1/2}) - g(\hat{u}_{(i-1)+,j}^{n+1/2}, \hat{u}_{i-,j}^{n+1/2}) \right] \\ & - \frac{\Delta t}{\Delta y} \left[h(\hat{u}_{i,j+}^{n+1/2}, \hat{u}_{i,(j+1)-}^{n+1/2}) - h(\hat{u}_{i,(j-1)+}^{n+1/2}, \hat{u}_{i,j-}^{n+1/2}) \right], \quad (4.20) \end{aligned}$$

accurate to second-order in space and time. A closer inspection of $g(\hat{u}_{i+,j}^{n+1/2}, \hat{u}_{(i+1)-,j}^{n+1/2})$, for example, reveals that this flux is a combination of three terms: the simple first-order flux, the space and time improved flux, and the dimensionality of the problem considering flux.

The explicit two-dimensional first-order accurate FV scheme for curvilinear coordinates is given by (4.4a), where the numerical fluxes (4.12) along the outer normals are obtained by solving local RPs (cf. Section 4.1.2). To improve the accuracy of the scheme we have to find an appropriate extrapolation of $u(x, y, t_n)$ within each local grid zone $V_{i,j}$ in the physical area. Adopting the concept of piecewise linear states, we approximate $u(x, y, t_n)$ according to

$$u(x, y, t_n) \approx u_{i,j}^n + du_{i,j}^n, \quad (4.21a)$$

where $du_{i,j}^n$ denotes the linear growth of u given by

$$du_{i,j}^n = \text{grad} u^n|_{i,j} dr. \quad (4.21b)$$

Performing the approximation from the grid points in the physical area obtained by an elliptical grid generator (see Section 3.1), it is necessary to specify the mapping depicted in Figure 3.1 more properly. Therefore, let T be a continuous and at least two times differentiable transformation $T : G^* \rightarrow G$ with $x = x(\xi, \eta)$ and $y = y(\xi, \eta)$ where $(\xi, \eta) \in G^* \subseteq \mathbb{R}^2$ and $(x, y) \in G \subseteq \mathbb{R}^2$. Since $du_{i,j}^n$ is independent of the

coordinate system, it is convenient for our considerations to estimate the growth in this coordinate system in G whose basis consists of the tangent vectors at the parameter lines:

$$du_{i,j}^n = (r - \tilde{r}_{i,j})_\xi \partial_\xi u^n + (r - \tilde{r}_{i,j})_\eta \partial_\eta u^n, \quad (4.21c)$$

where the subscripts ξ and η denotes the components of the representation of $r - \tilde{r}_{i,j}$ in the basis mentioned above. Along the isoline $\eta = \eta_{i,j}$, for example, the growth can be approximated by

$$du_{i\pm,j}^n \approx (\xi_{i\pm 1/2,j} - \xi_{i,j}) (s_\xi)_{i,j}^n, \quad (4.21d)$$

where the slope $(s_\xi)_{i,j}^n$ is calculated from (4.15a) with $a = u_{i+1,j}^n - u_{i,j}^n$, $b = u_{i,j}^n - u_{i-1,j}^n$ and Δx is substituted by $\Delta x_{i+1/2,j}$ and $\Delta x_{i-1/2,j}$, respectively (see Figure 4.5). However, proceeding in this way leads to an inconsistency since we need the

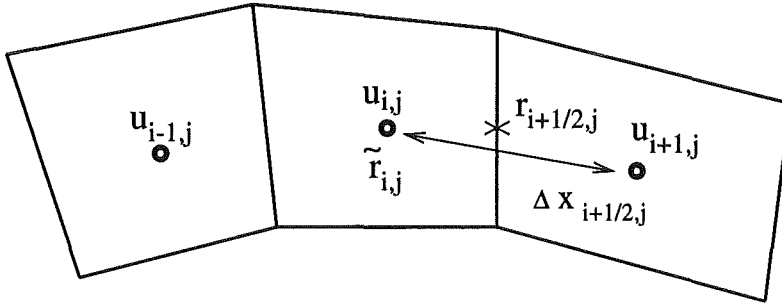


Figure 5: Notation for the slope approximation in the two-dimensional case.

coordinates of $r = r_{i+1/2,j}$ in the (ξ, η) -basis at the midpoint of the boundary segment $S_{i,j,\beta}$ in the physical area (see Section 4.1.2) which are not known. At the moment we manage this problem by an additional approximation, namely, we replace

$$r_{i+1/2,j} \approx \tilde{r}_{i,j} + \frac{\Delta x_{i+1/2,j}}{2}. \quad (4.21e)$$

In doing this, we obtain rather good numerical results as demonstrated in [41]. However, further investigations are necessary to overcome the mentioned difficulty.

For completeness as well as in view of the numerical results presented in Section 6, two additional remarks may be useful at this stage.

First, there is another way to achieve second-order accuracy by combining two one-dimensional (cf. equation (4.8)) second-order schemes by way of dimensional splitting. Using (4.14e), an intermediate result is calculated considering only the x -direction:

$$\tilde{u}_{i,j}^n = u_{i,j}^n - \frac{\Delta t}{\Delta x} \left[g(u_{i+,j}^{n+1/2}, u_{(i+1)-,j}^{n+1/2}) - g(u_{(i-1)+,j}^{n+1/2}, u_{i-,j}^{n+1/2}) \right]. \quad (4.22a)$$

Afterwards, the y -direction is taken into account. By using the result (4.22a), we obtain

$$u_{i,j}^{n+1} = \tilde{u}_{i,j}^n - \frac{\Delta t}{\Delta y} \left[h(\tilde{u}_{i,j+}^{n+1/2}, \tilde{u}_{i,(j+1)-}^{n+1/2}) - h(\tilde{u}_{i,(j-1)+}^{n+1/2}, \tilde{u}_{i,j-}^{n+1/2}) \right] \quad (4.22b)$$

for the evolution of $u_{i,j}$ within one time step, where the fluxes g and h are given in Appendix B. Interchanging in the following time step the way of calculating (4.22), the dimensional splitting method proposed by Strang [55] is obtained. Within this scheme, all flux calculations are performed with second-order accuracy. Compared to the MUSCL-ansatz discussed above, the dimensional splitting has the advantage that only half of the number of RPs have to be solved, but it can suffer due to its asymmetric structure. Nevertheless, we obtain good results from both schemes on Cartesian grids as shown in Section 6. Further it should be mentioned, that the splitting-ansatz could also be applied to the boundary-fitted coordinates. Secondly, by a similar procedure as discussed above, one obtains FV schemes of the order n if n -th order interpolation polynomials are used. For a more detailed review of these ENO-schemes (Essential-Non-Oscillatory schemes) we refer to [20].

4.1.4 Boundary Conditions

An important part of solving numerically Maxwell equations is to specify the boundary conditions properly. The numerical realization of both physically and computationally motivated boundary conditions are hence the item of this section. Physical boundary conditions are associated with material properties prescribed inside or at the contour of an electrical device as well as certain symmetry considerations. Computational boundary conditions are necessary for limiting the computational domain and are known as nonreflecting or open boundary conditions. For our applications conditions like "perfectly conducting boundary", "axial symmetry", "periodic boundary" and "open boundary" are important.

First of all, we discuss the numerical realization of a perfectly conducting boundary in a FV scheme, where we assume that the boundaries are parallel to the coordinate axes. This is not a restriction since a curved boundary parallel to the direction of a boundary-fitted coordinate line can be treated in a similar way. On a perfectly conducting wall the electric field tangential to and the magnetic induction normal to the surface vanish. This means (see, e.g. [24]),

$$\mathbf{n} \times \mathbf{E} = 0, \quad (4.23a)$$

$$\mathbf{n} \cdot \mathbf{B} = 0, \quad (4.23b)$$

where \mathbf{n} denotes the normal to the conducting surface. Looking at the situation depicted in Figure 4.5 where a perfect conducting wall extends along the x_1 -axis, the conditions (4.23) at $x_2 = 0$ reads as

$$E_1 = 0, \quad E_3 = 0, \quad B_2 = 0. \quad (4.24)$$

The other components of the fields are arbitrary and should not be prescribed. For the boundary condition implementation there is at least one further grid zone outside the actual computational domain available, where a yet unknown state u_L can be specified. Solving the RP (cf. Section 4.1.1)

$$\partial_t u + \mathcal{K}_2 \partial_x u = 0, \quad (4.25a)$$

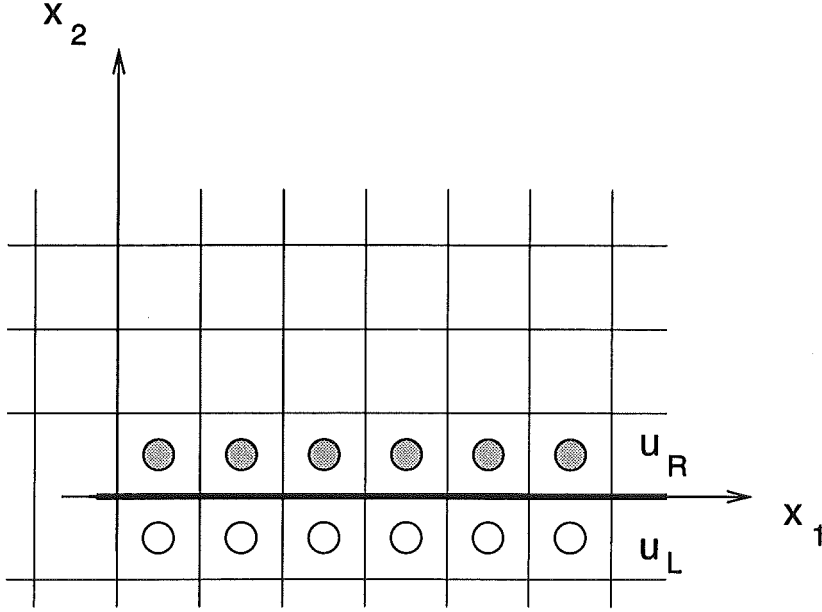


Figure 6: Boundary treatment of a perfectly conducting wall at $x_2 = 0$.

$$u(x_1, 0, 0) = \begin{cases} u_L & x_1 < 0 \\ u_R & x_1 > 0 \end{cases}, \quad (4.25b)$$

the solution at the boundary $x_2 = 0$ can be obtained which still depends on the unknown value u_L in the additional grid zone. Since the eigenvalue $\lambda = 0$ of \mathcal{K}_2 (see Appendix D), two characteristics coincide with the boundary and the solution is not defined. To overcome this problem, we define the mean of the states left and right of the boundary (see Figure 4.3) and obtain with (4.6c)

$$u|_{x_2=0} = u_L + \alpha_1 r^1 + \alpha_2 r^2 + \frac{1}{2} (\alpha_3 r^3 + \alpha_4 r^4). \quad (4.26)$$

Now we can choose u_L such that the requirements (4.24) are fulfilled at the conducting wall at $x_2 = 0$. Specifying the values of the left state u_L according to

$$(E_1)_L = -(E_1)_R \quad (4.27a)$$

$$(E_2)_L = (E_2)_R \quad (4.27b)$$

$$(E_3)_L = -(E_3)_R \quad (4.27c)$$

$$(B_1)_L = (B_1)_R \quad (4.27d)$$

$$(B_2)_L = -(B_2)_R \quad (4.27e)$$

$$(B_3)_L = (B_3)_R, \quad (4.27f)$$

we find for the solution at the conducting boundary surface

$$u^{PC}|_{x_2=0} = \begin{pmatrix} 0 \\ (E_2)_R \\ 0 \\ -\frac{1}{c}(E_3)_R + (B_1)_R \\ 0 \\ \frac{1}{c}(E_1)_R + (B_3)_R \end{pmatrix}, \quad (4.28a)$$

and for the associated numerical flux

$$g^{PC} = \mathcal{K}_2 u^{PC}|_{x_2=0} = \begin{pmatrix} -c(E_1)_R - c^2(B_3)_R \\ 0 \\ -c(E_3)_R + c^2(B_1)_R \\ 0 \\ 0 \\ 0 \end{pmatrix}. \quad (4.28b)$$

Replacing in (4.25a) \mathcal{K}_2 by \mathcal{K}_1 and repeating the outlined procedure for $x_1 = \text{constant}$, we can construct the boundary conditions for a computational domain surrounded by a perfectly conducting wall. Second-order boundary conditions for a perfectly conducting wall may be obtained by the aid of a second auxiliary grid zone outside the computational domain. To fulfill the boundary conditions at $x_2 = 0$ require that we have to relate the values u_{L-1} to those at u_{R+1} according to (4.27).

Physical problems are often much easier to handle if a certain symmetry condition with respect to a plane or an axis exists. For the devices under consideration we have rotational symmetry with respect to the x_1 -axis. Hence, the components of the vector of conserved quantities obeys the following symmetry relations

$$E_1(x_1, -x_2, x_3) = E_1(x_1, x_2, x_3) \quad (4.29a)$$

$$E_2(x_1, -x_2, x_3) = -E_2(x_1, x_2, x_3) \quad (4.29b)$$

$$E_3(x_1, -x_2, x_3) = -E_3(x_1, x_2, x_3) \quad (4.29c)$$

$$B_1(x_1, -x_2, x_3) = B_1(x_1, x_2, x_3) \quad (4.29d)$$

$$B_2(x_1, -x_2, x_3) = -B_2(x_1, x_2, x_3) \quad (4.29e)$$

$$B_3(x_1, -x_2, x_3) = -B_3(x_1, x_2, x_3). \quad (4.29f)$$

Since the electric field and the magnetic induction have to be continuous, it is obvious that

$$E_2(x_1, 0, x_3) = 0 \quad (4.30a)$$

$$E_3(x_1, 0, x_3) = 0 \quad (4.30b)$$

$$B_2(x_1, 0, x_3) = 0 \quad (4.30c)$$

$$B_3(x_1, 0, x_3) = 0 \quad (4.30d)$$

at the x_1 -axis. From the solution of the RP (4.25) it is easy to verify that by choosing

$$(E_1)_L = (E_1)_R \quad (4.31a)$$

$$(E_2)_L = -(E_2)_R \quad (4.31b)$$

$$(E_3)_L = -(E_3)_R \quad (4.31c)$$

$$(B_1)_L = (B_1)_R \quad (4.31d)$$

$$(B_2)_L = -(B_2)_R \quad (4.31e)$$

$$(B_3)_L = -(B_3)_R, \quad (4.31f)$$

the conditions (4.30) are fulfilled at the axis. Explicitly, the conserved vector u and the numerical flux at the x_1 -axis is given by

$$u^{RS}|_{x_2=0} = \begin{pmatrix} (E_1)_R + c(B_3)_R \\ 0 \\ 0 \\ -\frac{1}{c}(E_3)_R + (B_1)_R \\ 0 \\ 0 \end{pmatrix}, \quad (4.32a)$$

and

$$g^{RS} = \mathcal{K}_2 u^{RS}|_{x_2=0} = \begin{pmatrix} 0 \\ 0 \\ -c(E_3)_R + c^2(B_1)_R \\ 0 \\ 0 \\ -(E_1)_R - c(B_3)_R \end{pmatrix}, \quad (4.32b)$$

respectively.

In analytical investigations it is convenient to use for simplicity periodic boundary conditions, for example, at the lower and upper border of the physical area in the x_2 -direction [66]. For comparison, it is important to specify such a condition optionally in the computer code under development. Suppose the cell numbering in the x_2 -direction runs from $j = 1, \dots, J$ for grid cells within the computational domain. Immediately, we can impose the values of the additional two auxiliary grid zones outside the lower and upper boundary line according to

$$u_{i,0} = u_{i,J}, \quad (4.33a)$$

$$u_{i,-1} = u_{i,J-1}, \quad \forall i, \quad (4.33b)$$

and

$$u_{i,J+1} = u_{i,1}, \quad (4.33c)$$

$$u_{i,J+2} = u_{i,2}, \quad \forall i. \quad (4.33d)$$

These guarantee that first and second-order periodic boundary conditions are established.

Open boundaries are numerically motivated conditions and are needed to limit artificially the computational domain. A useful criterion of an open boundary is given by the definition of Hedstrom [21]: There, the amplitudes of the incoming waves should be constant in time, and consequently, no wave runs into the computational domain. Following the ideas of Thompson [58], incoming and outgoing travelling waves can be identified by the use of characteristic variables. To demonstrate the basic features, we consider the system

$$\partial_t u + \mathcal{A} \partial_x u = 0, \quad (4.34a)$$

with a boundary at $x = x_0$, $x_0 > 0$, and assume that an open boundary occurs at the right side of the computational domain. Further, it is assumed that \mathcal{A} has the eigenvalues

$$\lambda_1 \leq \dots \leq \lambda_{k_0} < 0 \leq \dots \leq \lambda_m \quad (4.34b)$$

and the right eigenvectors written in matrix notation

$$\mathcal{R} = (r^1, \dots, r^m). \quad (4.34c)$$

With the characteristic variables

$$v = \mathcal{R}^{-1} u, \quad (4.35a)$$

equation (4.34a) decouples into m independent equations:

$$\partial_t v + \Lambda \partial_x v = 0, \quad (4.35b)$$

with

$$\Lambda = \text{diag}(\lambda_1, \dots, \lambda_m). \quad (4.35c)$$

Waves belonging to the eigenvalues $\lambda < 0$ move to the left, i.e., inside the computational domain, and those with $\lambda > 0$ travel to the right outside the computational domain. Replacing the incoming waves at the open boundary, namely, the first k_0 equations in (4.35b) by

$$\partial_t (v_i) = 0; \quad i = 1, \dots, k_0, \quad (4.35d)$$

and transforming back to the conserved variables u , yields two systems of equations

$$\partial_t u + \mathcal{A}^+ \partial_x u = 0, \quad x \text{ at the boundary}, \quad (4.36a)$$

$$\partial_t u + \mathcal{A} \partial_x u = 0, \quad x \text{ elsewhere}, \quad (4.36b)$$

with

$$\mathcal{A}^+ = \mathcal{R}^{-1} \Lambda^+ \mathcal{R}; \quad \Lambda^+ = \text{diag}(0, \dots, \lambda_{k_0+1}, \dots, \lambda_m). \quad (4.36c)$$

The discretization of the latter system can be performed according to the equations (4.8) and (4.9). Since $(\mathcal{A}^+)^+ = \mathcal{A}^+$ and $(\mathcal{A}^+)^- = 0$ (cf. equation (4.9a)), the first system (4.36a) can be discretized using the numerical flux

$$G_{i+1/2}^{OB} = \mathcal{A}^+ u_L \quad (4.37)$$

at the open boundary. The outlined method is one possibility, namely, to use a modified flux calculation at the boundary of interest. The other approach we used is based on the additional auxiliary grid zones outside the computational domain. There, adequate values have to be prescribed in order to use the flux calculation (4.9) for both boundary as well as inner grid zones. Therefore, we first solve a RP with \mathcal{A}^+ at the open boundary at $x_1 = \text{constant}$, resulting in $\tilde{u}^{OB}|_{x_1=\text{const.}} = u_L$ because \mathcal{A}^+ has only positive eigenvalues. With this knowledge and the solution $u|_{x_1=\text{const.}}$ of the RP for the matrix \mathcal{A} which is similar to the case of a perfect conducting boundary, we demand that the numerical fluxes at the open boundary are equal:

$$\mathcal{A} \tilde{u}^{OB}|_{x_1=\text{const.}} = \mathcal{A} u^{OB}|_{x_1=\text{const.}} \quad (4.38a)$$

$$\Rightarrow \mathcal{A} u_L = \mathcal{A}^+ u_L + \mathcal{A}^- u_R. \quad (4.38b)$$

Hence, with $\mathcal{A} = \mathcal{A}^+ + \mathcal{A}^-$ it is sufficient to set

$$u_R = u_L \quad (4.38c)$$

in the auxiliary grid zone and to apply the usual FV scheme (4.8) with the flux calculation (4.9).

4.2 Staggered-Leapfrog FDTD Approach

An attractive method for solving numerically the time-dependent Maxwell equations in the context of plasma simulations [8] is based on finite-difference (FD) time-domain (TD) approach on staggered grids, proposed originally by Yee [70]. Especially, in the well established Quicksilver code used for ion diode simulations, FD methods on Cartesian grids have been successfully applied [43]. Although it has been found out that an implicit discretization of Maxwell equations is necessary in order to obtain numerical stability, a FD based field solver is an approved standard approach, helpful to evaluate further improvements in this area. To have the opportunity to acquire experience with a $2\frac{1}{2}$ -dimensional Maxwell-Lorentz simulation program running with a FV as well as with a FD Maxwell solver, we decided to implement the canonical Yee-scheme for orthogonal grids also.

Depending on the test results of the Maxwell-Lorentz program system for both field solvers an extension of the standard FD schemes could be made. One possibility of the extension from Cartesian to arbitrary quadrilateral grids can be performed by applying transformation methods discussed, for example, in [23]. A more obvious generalization of the standard FD schemes to unstructured grids with a modified finite-volume or a discrete surface integral method has been recently given in [32, 33].

In the following we will briefly outline the basic FD approach for Cartesian coordinates, which is second-order accurate in space and time. For our purpose, we assume again that the conserved quantities u are constant with respect to x_3 , namely $\partial_3 u = 0$, and starting our discussions from the equations (4.1). Applying simple central differences to approximate the first-order spatial derivatives in 4.1a, we first

have to specify the computational grid. A natural way to obtain the staggered grid shown in Figure 7, is to apply Stokes's theorem to Maxwell's curl equations [60, 61]. Obviously, from Figure 7, the electric and magnetic quantities are defined on the

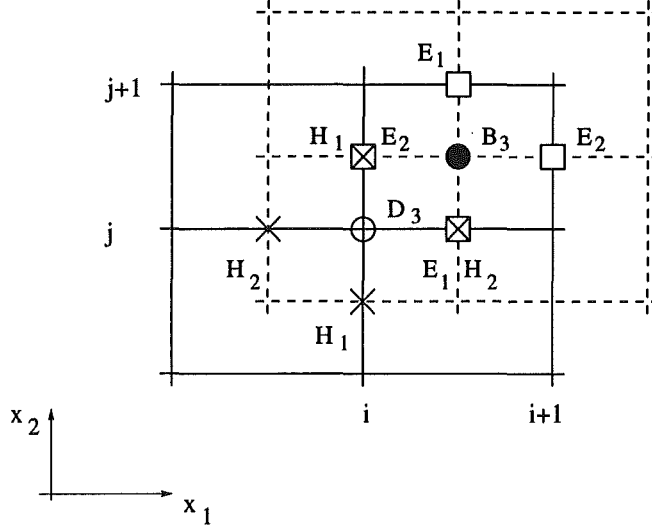


Figure 7: Original (—) and dual grid (- - -) grid in the (x_1, x_2) -plane. The electric E_1, E_2 (\square) and magnetic H_1, H_2 (\times) fields are specified at the edges, while the magnetic induction B_3 (\bullet) and electrical displacement D_3 (\circ) are associated with the faces of the original and dual grid, respectively.

so-called original or "electric" and dual or "magnetic" grid, respectively. It is important to note that the association of the electric field with the original and the magnetic field with the dual grid is arbitrary and could be interchanged, depending on the boundary conditions imposed at the exterior boundary surface. In order to obtain the discrete equations, we rewrite (4.1) for the sake of clarity once again, and obtain the following formulas

$$\partial_t \mathbf{D} = \sum_{\mu=1}^2 \mathcal{M}_{\mu} \partial_{x_{\mu}} \mathbf{H} - \mathbf{J} + \frac{\kappa}{x_2} (H_3, 0, 0)^T, \quad (4.39a)$$

$$\partial_t \mathbf{B} = - \sum_{\mu=1}^2 \mathcal{M}_{\mu} \partial_{x_{\mu}} \mathbf{E} - \frac{\kappa}{x_2} (E_3, 0, 0)^T, \quad (4.39b)$$

where $\mathbf{D} = \epsilon_0 \mathbf{E}$ and $\mathbf{H} = \frac{\mathbf{B}}{\mu_0}$ denotes the electrical displacement and magnetic field, respectively, and the matrices \mathcal{M}_{μ} are given by (4.1d). For the situation of two equidistant grids as depicted in Figure 7 where Δx_1 and Δx_2 are constant, we assign the lower left corner of the original grid with $((x_1)_i, (x_2)_j)^T = (i\Delta x_1, j\Delta x_2)^T$ and use for a field quantity \mathbf{V} given at that point the notation $\mathbf{V}(i\Delta x_1, j\Delta x_2) = \mathbf{V}_{i,j}$. Guided by Figure 7, we replace the spatial derivatives in (4.39) by central differences yielding the following approximations for the temporal derivatives of the electrical displacement

$$\begin{aligned}
(\partial_t D_1)_{i+1/2,j} &= \frac{1}{\Delta x_2} [(H_3)_{i+1/2,j+1/2} - (H_3)_{i+1/2,j-1/2}] \\
&\quad - (J_1)_{i+1/2,j} + \frac{\kappa}{(x_2)_j} (H_3)_{i+1/2,j} , \tag{4.40a}
\end{aligned}$$

$$\begin{aligned}
(\partial_t D_2)_{i,j+1/2} &= -\frac{1}{\Delta x_1} [(H_3)_{i+1/2,j+1/2} - (H_3)_{i-1/2,j+1/2}] \\
&\quad - (J_2)_{i,j+1/2} , \tag{4.40b}
\end{aligned}$$

$$\begin{aligned}
(\partial_t D_3)_{i,j} &= \frac{1}{\Delta x_1} [(H_2)_{i+1/2,j} - (H_2)_{i-1/2,j}] \\
&\quad - \frac{1}{\Delta x_2} [(H_1)_{i,j+1/2} - (H_1)_{i,j-1/2}] - (J_3)_{i,j} , \tag{4.40c}
\end{aligned}$$

and the magnetic induction

$$\begin{aligned}
(\partial_t B_1)_{i+1,j+1/2} &= -\frac{1}{\Delta x_2} [(E_3)_{i+1,j+1} - (E_3)_{i+1,j}] \\
&\quad - \frac{\kappa}{(x_2)_{j+1/2}} (E_3)_{i+1,j+1/2} , \tag{4.41a}
\end{aligned}$$

$$(\partial_t B_2)_{i+1/2,j+1} = \frac{1}{\Delta x_1} [(E_3)_{i+1,j+1} - (E_3)_{i,j+1}] \tag{4.41b}$$

$$\begin{aligned}
(\partial_t B_3)_{i+1/2,j+1/2} &= -\frac{1}{\Delta x_1} [(E_2)_{i+1,j+1/2} - (E_2)_{i,j+1/2}] \\
&\quad + \frac{1}{\Delta x_2} [(E_1)_{i+1/2,j+1} - (E_1)_{i+1/2,j}] . \tag{4.41c}
\end{aligned}$$

For the subsequent time integration of the electromagnetic fields itself, we use a time-centered leapfrog-style technique, seen in Figure 8. Combining the lhs of (4.40) to

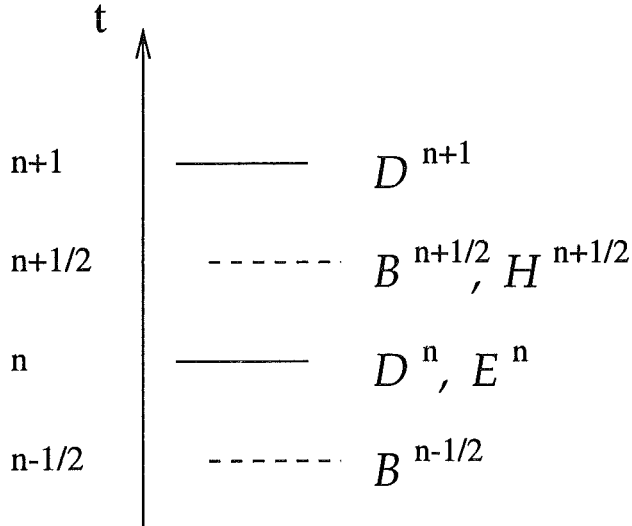


Figure 8: Leapfrog type scheme for the electromagnetic fields.

the vector \mathcal{D}^n taken at the time level $t_n = n\Delta t$ and those of (4.41) to a vector $\mathcal{B}^{n-1/2}$ at half-integer times $t_{n-1/2}$, the step-by-step leapfrog integration finally reads as

$$\mathcal{D}^{n+1} = \mathcal{D}^n + \Delta t \mathbf{f}(\mathbf{H}^{n+1/2}), \quad (4.42a)$$

$$\mathcal{B}^{n+1/2} = \mathcal{B}^{n-1/2} + \Delta t \mathbf{g}(\mathbf{E}^n), \quad (4.42b)$$

where \mathbf{f} and \mathbf{g} are the abbreviations of the rhs of (4.40) and (4.41), respectively. The equations (4.40)-(4.42) set up the two-dimensional Yee-scheme for Cartesian ($\kappa = 0$) and rotationally symmetric ($\kappa = 1$) geometries, which is fully explicit second-order accurate and non-diffusive. For special problems it is important to improve the robustness of this scheme. Therefore, artificial viscosity terms are added or additional implicit iterations are performed [51].

As already mentioned above, appropriate boundary conditions have to be specified and properly transposed into the numerical algorithm. Although the FD method based scheme can be written in conservation form, it turns out that it is different from the vector-splitting scheme. Therefore, somewhat other techniques have to be applied to impose the boundary conditions. Perfectly conducting wall, axial symmetry and periodic boundary conditions are algorithmically established in the same manner as given in the literature (see, e.g., [8]). Limiting artificially the computational domain, one has to specify open or so-called absorbing boundary conditions. For formulating and applying these conditions we can refer to the experience already discussed in [26]. There, several strategies to overcome the difficulties arising with open boundary conditions are discussed and appropriate algorithms within a FD approach are given, based on the works of Lindman, Enquist and Majda, and Wagatha [31, 14, 59]. The basic ideas of these investigations can be summarized as follows: Each component of the electromagnetic field satisfies a scalar wave equation which can be decomposed into an incoming and outgoing part at a certain boundary using projection operators. The remaining main task is finally to construct appropriate approximations of a pseudo-differential operator to filter out incoming waves at the surface boundary to avoid disagreeable reflections.

5 Particle Treatment

In addition to the nonstationary Maxwell field solver a further important building block for the numerical realization of the Maxwell-Lorentz system (2.2), (2.3) is the particle treatment. Well-known techniques, generally called particle methods [22], are applied.

The particle-in-cell (PIC) method [4, 22] is an attractive computational tool for studying kinetic phenomena, in particular in plasma physics: The orbits of electrically charged particles have to be determined with respect to externally applied as well as self-generated electromagnetic fields. Especially, for pulsed power ion diodes the magnitude of the self-generated fields is of the same order than this of the applied ones. The problem of particle handling is that the electromagnetic fields are sampled on discrete Eulerian grid points whereas the particle position can be continuous within this computational grid.

The basic idea of the PIC method is that the particle movement consists of four steps: The fields given at mesh points are interpolated onto the particle position producing the forces acting upon the charged particle (Interpolation). When the electric and magnetic forces on the particle position are known, each particle is transported further by solving the Lorentz equation (Particle pushing). After arriving at the new position the particles have to be localized within the grid, by computing the relative coordinates with respect to the cell the particle is located in (Localization). On the basis of the new phase space coordinates the charge and current densities can be calculated at the mesh points to serve as source terms for the next step of the field solver (Density Assignment).

As long as the computational grid used consists of equidistant grid lines, the algorithms for interpolation and localization are simple. However, when using boundary-fitted coordinate systems (see Section 3), the grid cells are not equidistant and standard methods can no longer be applied directly.

In the following, extended algorithms for interpolation and localization as well as particle pushing will be reported. For a detailed investigation of these particular algorithms as well as alternative algorithms we refer to the References [50, 65, 63].

Most steps of the particle handling have already been realized in the well established stationary Maxwell-Lorentz solver for boundary-fitted coordinates [67] and published in several papers [50, 63, 65]. For the sake of completeness, only a brief overview of the basic procedure of particle treatment is given in the following. However, the well-tested BFCPIC subroutines require a careful adaptation to the new data structure fixed by the solution method of the instationary Maxwell equations.

5.1 Interpolation

If a particle P with the coordinates (α_1, α_2) is located in the unit square cell $I^2 = [0, 1] \times [0, 1]$ as shown in Figure 5.1a, the fields u_P (see equation (4.1b)) at the particle

position is calculated from the fields $u_{00}, u_{10}, u_{11}, u_{01}$ given at the mesh points using the standard area-weighting method [36]

$$\begin{aligned} u_P &= (1 - \alpha_1)(1 - \alpha_2) u_{00} + \alpha_1(1 - \alpha_2) u_{10} \\ &+ (1 - \alpha_1)\alpha_2 u_{01} + \alpha_1\alpha_2 u_{11} . \end{aligned} \quad (5.1)$$

In order to apply the area weighting method in an arbitrary quadrilateral grid zone V_{IJ} as depicted in Figure 5.1b, proper interpolation weights have to be calculated. Geometrically the interpolation weight α_1 can be found by determining the line l_1 through point P intersecting line \overline{DC} with the same ratio as line \overline{AB} . In the same way, α_2 can be constructed by line l_2 intersecting line \overline{AD} and \overline{BC} with the same ratio. If $S_{AB}, S_{BC}, S_{DC}, S_{AD}$ are these intersection points then

$$\alpha_1 = \frac{\overline{AS}_{AB}}{\overline{AB}} = \frac{\overline{DS}_{DC}}{\overline{DC}} \quad (5.2a)$$

$$\alpha_2 = \frac{\overline{AS}_{AD}}{\overline{AD}} = \frac{\overline{BS}_{BC}}{\overline{BC}} . \quad (5.2b)$$

Let $(x, y) \in V_{IJ}$ be the position of the particle in cell (I, J) with corners $A =$

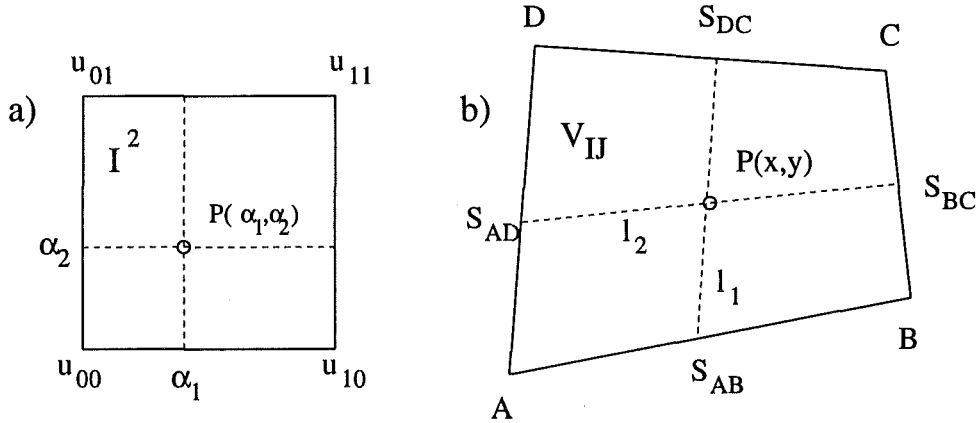


Figure 1: Geometrical interpretation of the interpolation weights (α_1, α_2) in a unit square cell I^2 (a) and in a quadrilateral grid zone V_{IJ} (b).

$r_{i-1/2, j-1/2}$, $B = r_{i+1/2, j-1/2}$, $C = r_{i+1/2, j+1/2}$, and $D = r_{i-1/2, j+1/2}$, where $r_{i, j} = (x_{i, j}, y_{i, j})^T$. The interpolation weights $(\alpha_1, \alpha_2) \in I^2$ are then given by the following formulas:

$$\alpha_2 = \frac{-p + \sqrt{p^2 + q}}{x_{i+1/2, j+1/2}^s - 1} \quad \text{for } x_{i+1/2, j+1/2}^s \neq 1 , \quad (5.3a)$$

$$\alpha_2 = \frac{y^s}{1 + x^s(y_{i+1/2, j+1/2}^s - 1)} \quad \text{for } x_{i+1/2, j+1/2}^s = 1 , \quad (5.3b)$$

$$\alpha_1 = \frac{x^s}{1 + \alpha_2(x_{i+1/2, j+1/2}^s - 1)} , \quad (5.3c)$$

where

$$p = \frac{1}{2} \left[1 + x^s \left(y_{i+1/2, j+1/2}^s - 1 \right) - y^s \left(x_{i+1/2, j+1/2}^s - 1 \right) \right], \quad (5.3d)$$

$$q = y^s \left(x_{i+1/2, j+1/2}^s - 1 \right). \quad (5.3e)$$

The quantities x^s, y^s are obtained from the matrix equation

$$\begin{pmatrix} x^s \\ y^s \end{pmatrix} := \begin{pmatrix} x_{10} - x_{00} & x_{01} - x_{00} \\ y_{10} - y_{00} & y_{01} - y_{00} \end{pmatrix}^{-1} \begin{pmatrix} x - x_{00} \\ y - y_{00} \end{pmatrix}, \quad (5.3f)$$

where the subscripts are the abbreviation for: $(00) = (i - 1/2, j - 1/2)$, $(10) = (i + 1/2, j - 1/2)$ and $(01) = (i - 1/2, j + 1/2)$. A more theoretical treatment can be found in [50]. The proposed interpolation weights together with the area-weighting method as the interpolation scheme have the characteristic feature that linear functions are represented exactly; for a proof see also [50].

5.2 Particle Pushing

As already discussed in Section 2, the equations of motion for charged macro particles in electromagnetic fields are set up by (2.5) with the Lorentz force \mathbf{F}_L (2.1b). Since electrons and the corresponding macro particles reach velocities near the speed of light, the relativistic equation of motion (2.5) must be solved for the case in which the ratio $Q_i/M_i = q_e/m_e$ with the initial conditions

$$\mathbf{x}_{i0} = \mathbf{x}_i(0), \quad (5.4a)$$

$$\mathbf{U}_{i0} = \mathbf{U}(0) = \gamma(0)\mathbf{v}(0). \quad (5.4b)$$

Calculating the phase space coordinates of the ion macro particles, the relevant equation is the non-relativistic Lorentz equation, obtained from (2.5) by setting $\gamma = 1$ and using the ratio q_i/m_i for the ions.

For the numerical solution of both relativistic and non-relativistic equations the leapfrog-scheme is used:

$$\frac{\mathbf{U}^{n+1/2} - \mathbf{U}^{n-1/2}}{\Delta t} = \frac{\mathbf{F}_L^n}{m_\alpha}, \quad (5.5a)$$

$$\frac{\mathbf{x}^{n+1} - \mathbf{x}^n}{\Delta t} = \mathbf{v}^{n+1/2}, \quad (5.5b)$$

where Δt is the time step size and n the time level. \mathbf{F}_L^n is the force at time $t = t_n$ due to the electric field \mathbf{E}^n and the magnetic field \mathbf{B}^n at the particle position \mathbf{x}^n . The first equation is centered around $n \times \Delta t$ and the second one around $(n + 1/2) \times \Delta t$. The advantage of this second-order scheme is its time-centeredness and, hence, its time reversibility.

By solving the equation of motion the special structure of the electromagnetic force is taken into account [8]: After a "half-acceleration" (acceleration by $\Delta t/2$) with

the electric field \mathbf{E}^n the vector \mathbf{U}^n is obtained. With this quantity together with the magnetic field \mathbf{B}^n the rotation is computed. A final half-acceleration by the electric field produces $\mathbf{U}^{n+1/2}$. Using $\mathbf{U}^{n+1/2}$ and the additional averaging $\mathbf{x}^{n+1/2} = \frac{1}{2}(\mathbf{x}^{n+1} + \mathbf{x}^n)$ the phase space coordinates $(\mathbf{v}_i^{n+1/2}, \mathbf{x}_i^{n+1/2})$ of each macro particle P_i can be computed. After the particles have been advanced and time has been updated, all the particles have to be localized inside the computational grid.

5.3 Localization

In order to identify cells within a grid, the addresses of the lower left grid point of each cell are assigned to the cell as a pair of numbers (I, J) . For our applications, the interpolation scheme is also used in order to find the particle position with respect to the grid: After the new coordinates of the particle P_i have been computed, the interpolation weights (α_1, α_2) are determined by transforming the cell (I_0, J_0) the particle was located in at the previous time step. With knowledge of these interpolation weights (α_1, α_2) one can decide whether the particle still lies inside the same cell or whether it has moved outside:

- $(\alpha_1, \alpha_2) \in I^2 \quad \Leftrightarrow$ Particle P is still inside cell (I_0, J_0) .
- $(\alpha_1, \alpha_2) \notin I^2 \quad \Leftrightarrow$ Particle P has left cell (I_0, J_0) .

When using non-equidistant grids it is of course not guaranteed that the particle is found by calculating the weights corresponding to the old cell addresses. When the particle has left the cell, this algorithm must be applied iteratively until the correct interpolation weights $(\alpha_1, \alpha_2) \in I^2$ are found. The applied particle search algorithm consists of four steps and reads as

Search algorithm

- Step 1: Let $(I, J) = (I_0, J_0)$ be the cell the particle was located in at the previous time step,
- Step 2: Compute the interpolation weights (α_1, α_2) with respect to cell (I, J) ,
- Step 3: Add the interpolation weights to the cell address $(I + \alpha_1, J + \alpha_2)$,
- Step 4: Set $(I, J) = (INT(I + \alpha_1), INT(J + \alpha_2))$,
- Repeat steps 2 to 4 k times,

where INT denotes the usual integer function.

The iteration parameter k depends on the structure of the grid. In case of an equidistant grid, k can be chosen to be 1. (In this case, however, it is advisable to determine the cell in a direct manner.) For the situation of a non-equidistant grid our experience indicates that $k=3$ is usually sufficient.

5.4 Charge and Current Density Assignment

Depending on the solution method of the nonstationary Maxwell equations, we have different data structure for the FV and FD approach (see Section 2). Therefore, we have to specify where the charge Q_i and the velocity v_i of the macro particle P_i is actually needed, in order to compute the source terms (charge and current density) of the Maxwell equations.

In the FV approach the electromagnetic fields u as well as the current density q are quantities averaged over the grid zone $V_{i,j}$, represented at the barycenter $\tilde{r}_{i,j}$ of $V_{i,j}$. Hence, we need the interpolation weights ($\tilde{\alpha}_1, \tilde{\alpha}_2$) to calculate the charge and current density at the barycenters, taking into account the relative position of the macro particle P_i within the cell established by these barycenters (see Figure 5.2). When the macro particle P_i is pushed and localized within the grid zone,

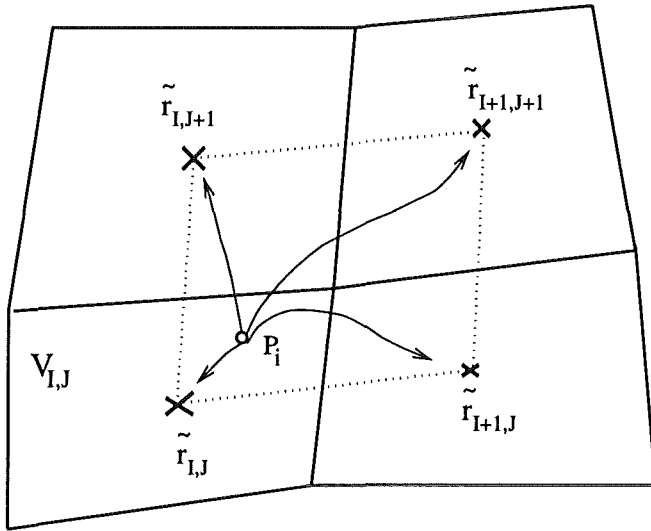


Figure 2: Charge and current density assignment to the barycenters \tilde{r}_{ij} surrounding the macro particle P_i .

the interpolation weights (α_1, α_2) are computed with respect to the new grid cell $V_{I,J}$. From these weights we can conclude in which quadrant of $V_{I,J}$ the macro particle is located. For the situation depicted in Figure 5.2 $\alpha_1 > \frac{1}{2}$ and $\alpha_2 > \frac{1}{2}$, and consequently P_i is surrounded by the barycenters $\tilde{r}_{I,J}$, $\tilde{r}_{I+1,J}$, $\tilde{r}_{I+1,J+1}$ and $\tilde{r}_{I,J+1}$. The interpolation weights ($\tilde{\alpha}_1, \tilde{\alpha}_2$) for these coordinates are calculated from equations (5.3). The contribution of the macro particle P_i to the charge and current density $\Delta D \in \{\Delta\rho, \Delta j\}$ at the four barycenter corners is given according to

$$\begin{aligned}\Delta D_{I,J} &= \frac{g_{I,J}}{|V_{I,J}|} \delta D_i, \\ \Delta D_{I+1,J} &= \frac{g_{I+1,J}}{|V_{I+1,J}|} \delta D_i, \\ \Delta D_{I+1,J+1} &= \frac{g_{I+1,J+1}}{|V_{I+1,J+1}|} \delta D_i,\end{aligned}$$

$$\Delta D_{I,J+1} = \frac{g_{I,J+1}}{|V_{I,J+1}|} \delta D_i, \quad (5.6a)$$

where $\delta D_i \in \{Q_i, Q_i \mathbf{v}_i\}$. The weights are obtained from

$$\begin{aligned} g_{I,J} &= (1 - \tilde{\alpha}_1)(1 - \tilde{\alpha}_2) \\ g_{I+1,J} &= \tilde{\alpha}_1(1 - \tilde{\alpha}_2) \\ g_{I,J+1} &= (1 - \tilde{\alpha}_1)\tilde{\alpha}_2 \\ g_{I+1,J+1} &= \tilde{\alpha}_1\tilde{\alpha}_2 \end{aligned} \quad (5.6b)$$

and $|V_{I,J}|$ is the volume assigned to $\tilde{r}_{I,J}$.

6 Results

Although the implementation of the algorithms of the field solvers as well as the particle treatment is finished, we have yet less experience in the interplay of both parts of the Maxwell-Lorentz program system. However, extensive calculations with both the FV and FD Maxwell field solver have been performed and the results of several test problems are reported in this paper.

Each version of the field solver is the algorithmical realization of one of the numerical methods discussed in Section 4.1 and 4.2, respectively. Optionally, Maxwell's equations can be solved for Cartesian, cylindrical and boundary-fitted coordinates. Furthermore, using the FV Maxwell solver one can switch between the dimensional splitting and the two-dimensional MUSCL-ansatz method (see Section 4.1.3). To increase the confidence and to demonstrate the possibilities and capabilities of the field solvers we proceed in the following in two steps: First, we present the results based on the solution of the homogeneous, and secondly, on the inhomogeneous Maxwell equations. These examples will also show the quality of the clearly formulated and numerically realized boundary conditions (see Section 4.1.4).

6.1 Numerical Results for the homogeneous Maxwell Equations

As a first test example we consider a typical initial-boundary-value (IBV) problem, where the $2\frac{1}{2}$ -dimensional field solvers based on FV and FD methods, respectively, solve numerically the homogeneous Maxwell equations for Cartesian coordinates. The computational domain $G = \{(x, y) \mid 0 \leq x \leq 200\text{m}; 0 \leq y \leq 200\text{m}\}$ is surrounded by a perfectly conducting wall, which means that we are testing the "perfect conducting boundary" condition. The IBV problem is set up by the assumptions that the electromagnetic fields are independent of the z -coordinate, that $B_3 = 0$ everywhere, and that E_3 vanishes at the boundary ∂G of the computational domain. With the initial conditions

$$E_{3,0}(x, y) = E_0 e^{-\frac{(x-x_0)^2 + (y-y_0)^2}{2\tau^2 c^2}}, \quad (6.1a)$$

$$\partial_t E_{3,0}(x, y) = 0, \quad (6.1b)$$

the wave equation for $E_3(x, y, t)$ can be solved exactly resulting in the so-called TM waves, as is outlined in Appendix E. The corresponding transverse magnetic induction $\mathbf{B}_\perp = (B_1, B_2, 0)^T$ is obtained in a simple manner from the solution of E_3 (see also Appendix E). For the numerical experiment we excite the third component of the electrical field according to the Gaussian (6.1a) with the height $E_0 = 1\text{V/m}$ and the width $\tau = 50\text{ns}$ at $x_0 = y_0 = 100\text{m}$. An overview of the numerical solution for this IBV problem obtained from the FV solver for $\Delta x = \Delta y = 1\text{m}$ is given in Figure 1. There, the temporal evolution of E_3 and B_1 is depicted in the upper part for the times $t \in \{0, 100\text{ns}, 200\text{ns}, 300\text{ns}\}$ as a function of y sliced at $x = 100\text{m}$. Obviously, we find that the initial pulse moves towards the conducting wall, where

E_3 remains zero for all times. The contour plots in the lower part of Figure 1 are recorded at $t = 200\text{ns}$ and $t = 300\text{ns}$ and give an impression of the spatial distribution of the fields E_3 and B_1 .

A quantitative comparison between the exact (solid lines) and numerical (open symbols) solution of the IBV problem is presented in Figure 2. For five different but fixed space points within the computational domain ($P_1 = (100.5\text{m}; 100.5\text{m})$, $P_2 = (119.5\text{m}; 119.5\text{m})$, $P_3 = (49.5\text{m}; 49.5\text{m})$, $P_4 = (149.5\text{m}; 24.5\text{m})$, $P_5 = (24.5\text{m}; 179.5\text{m})$) the electric field E_3 is plotted as a function of time on the nano-second time scale. The numerical results shown in the left part of Figure 2 are obtained with a field solver based on a first-order accurate FV scheme covering with 160 iterations a time-period of 400ns. Obviously, for the space points far away from the maximum height of the initial Gaussian pulse (P_3, P_4 , and P_5), numerical damping is observed. If one uses a second-order improved FV dimensional-splitting field solver (right part of Figure 2) the exact and numerical results are in nearly perfect agreement.

The magnetic induction B_3 for TE waves is derived in Appendix E in a manner similar to the solution of the IBV problem for the electric field component E_3 for TM waves. In this case the normal derivative of B_3 vanishes at the boundary ∂G and the initial conditions are the same as specified by (6.1) with the difference that E_0 is replaced by $B_0 = 1\text{Vns/m}^2 (= 10^{-9} \text{ T})$. The numerical calculations with a first- (left) and a second-order (right) accurate FV scheme (open symbols) are compared in Figure 3 with the exact solutions (solid lines). Clearly, the same features as already discussed for the TM waves shown in Figure 2 are evident. The comparison between the exact and numerical TM and TE wave calculations demonstrates that the algorithmical realization and implementation of the FV algorithms is properly done. Furthermore, we can conclude that the second-order space and time accurate FV field solver produce excellent results for a Cartesian computational grid surrounded by a perfectly conducting wall.

We subjected the FD staggered-leapfrog based approach to the same series of numerical tests. A typical result for the third component of the electric field E_3 is presented in Figure 4, which is initially excited according to a Gaussian profile (6.1). For this example, the computational domain $G = \{(x, y) \mid 0 \leq x \leq 20\text{m}; 0 \leq y \leq 20\text{m}\}$ is covered by an equidistant grid with $\Delta x = \Delta y = 0.1\text{m}$. The upper two pictures of Figure 4 give an overview of the numerical solution of the field distribution $E_3(x, y, t)$ at two different times. The time step size is fixed to $\Delta t = 0.472\text{ns}$ resulting in 500 and 2000 iterations for $t = 236\text{ns}$ and $t = 944\text{ns}$, respectively. A quantitative comparison between the exact (solid line) and numerical calculated (open circles) solution is given in the lower part of Figure 4. There, E_3 is plotted along a slice parallel to the y -axis at $x = 10\text{m}$ for $t = 236\text{ns}$ (left) and $t = 944\text{ns}$ (right). Obviously, the numerical solution obtained with the FD Maxwell field solver is in excellent agreement with the exact result. This demonstrates the proper implementation of the standard FD-Yee algorithm for a Cartesian computational grid when perfectly conducting boundaries are assumed.

The results discussed above encouraged us to continue with a comparison of two different second-order FV schemes: We repeated the TM wave calculations with the second-order dimensional-splitting method and used the results as reference solutions. With the same computational parameters given above, we perform the calculations with a FV field solver based on the two-dimensional, second-order space and time accurate MUSCL-ansatz method (see Section 4.1.3) and compare the results with the reference solutions. The results are presented in Figure 5 and 6 for the electric field E_3 and the magnetic induction B_1 , respectively. There, four slices parallel to the y -axis ($x \in \{100\text{m}, 150\text{m}, 180\text{m}, 190\text{m}\}$) recorded at the time $t = 400\text{ns}$ are shown for a TM calculation. A closer inspection of these Figures reveals that the results of the field solver using the MUSCL-ansatz approach are nearly identical to those of the reference solution for Cartesian coordinates.

Later on, the Maxwell-Lorentz program system will be applied to ion diode simulations, a cylinder symmetrical device. Therefore, it is important to test the Maxwell field solvers based on FV as well as FD methods for rotationally symmetric geometries with all their additional options in a very early stage of the program development. To check the field solvers for this case, we choose the standard problem of a cylindrical resonant cavity (see, e.g., [24]), whose corresponding formulas for the TM as well as TE fields are summarized in Appendix E. The dimension of the cavity, and hence, the computational domain is fixed according to $G = \{(z, r) \mid 0 \leq z \leq 100\text{m}; 0 \leq r \leq 100\text{m}\}$. At the end faces and at the surface of the cylinder perfect electrical conducting boundary conditions are imposed, while $r = 0$ is a symmetry axis.

In the following, we restrict ourselves to the TM fields calculation which is initialized at $t = 0$ by the exact electromagnetic fields with $\nu = n = 3$ (cf. Appendix E). The spatial behavior of the electric field $E_z(z, r, t)$ is depicted as a contour plot in Figure 7 for two snapshots recorded at $t = 50\text{ns}$ and $t = 150\text{ns}$. There, the results of a second-order accurate FV field solver based on a dimensional-splitting scheme are seen (lower two pictures) together with the exact calculations (upper two pictures) for comparison. For this test calculation we choose an equidistant grid spacing, namely, $\Delta z = \Delta r = 1\text{m}$ and the time step size Δt was fixed equal to 2.5ns , covering with 80 iterations a time period of 200ns . The arbitrary constant k used for the slope calculation (cf. equation (4.15a)) extending the FV scheme to second-order accuracy was set to 1.4 instead of one for the IBV example. A more quantitative comparison between exact and numerical results is obtained if slices parallel to the z - and r -axes are considered. Therefore, in Figure 8 and 9 the first component of the electric field E_z is shown for four different times sliced parallel to the z -axis at $z = 50\text{m}$ and parallel to the r -axis at $r = 50\text{m}$, respectively. Obviously, the agreement between the FV method based results (open circles) and the analytical solutions (solid lines) is very acceptable. The same statement holds for the other two field components E_r and B_φ (not shown here). Further extensive test calculations for the cylindrical resonant cavity have been performed, for example, by choosing different and larger ν and n , or increasing the number of time iterations to study the long-time behavior of the numerical solutions. Experience indicates

that the extended FV Maxwell solvers, treating the geometrical source terms in the cylinder symmetrical case (cf. equation (4.1e)) via a splitting method works in a very reliable and robust way.

6.2 Numerical Results for the inhomogeneous Maxwell Equations

With respect to ion diode simulations with the Maxwell-Lorentz code it is very important to have a field solver not only for the homogeneous but also for the inhomogeneous Maxwell's equations. This becomes obvious from the fact that in a self-consistent description of charged particles in the electromagnetic field the particle response enters as source terms in the field equations. Hence, we will consider in this section two simple test cases to demonstrate that the source term splitting proposed in Section 4.1.2 is an appropriate method for the numerical realization of an inhomogeneous field solver. Furthermore, it turns out that the considered test problems are good examples to check the numerical treatment of the open boundary conditions in the framework of FV methods (cf. Section 4.1.4).

First, we consider the model of a simple planar dipole which could be solved analytically as it is outlined in Appendix F. We assume that the electromagnetic system is excited perpendicular to the (x, y) -plane by the current density

$$J_z(x, y, t) = I_0 \delta(x - x_0) \delta(y - y_0) \cos(\omega t) \quad (6.2)$$

located at $x_0 = y_0 = 24.875\text{m}$, where the current $I_0 = 1\text{A}$ and the frequency $\omega = 0.1508/\text{ns}$ ($\nu = 24\text{MHz}$). In addition to these parameters, open boundary conditions are imposed at the border of the finite computational domain $G = \{(x, y) | 0 \leq x \leq 50\text{m}; 0 \leq y \leq 50\text{m}\}$. This domain is covered by an equidistant grid with a spacing of $\Delta x = \Delta y = 0.25\text{m}$. The long-time behavior of the third component of the electric field $E_3(x, y, t)$ calculated with a second-order FV scheme (open circles) is depicted in Figure 10 together with the exact (solid lines) cylindrical wave solution (cf. Appendix F). To that end, with a time step size of $\Delta t = 0.625\text{ns}$ 640 time-cycles have been performed. Figure 10 clearly indicates that the agreement between the exact and numerical solution is for all times very acceptable, especially, for the long range field which is the field far away from the location of the 2d-dipole. Since the plots of Figure 10 are recorded for $x = x_0$, we can conclude that no visible reflections propagate into the computational domain. The results of a more careful open boundary investigation are shown in Figure 11. There, different cuts parallel to the y -axis at $t = 400\text{ns}$ are presented, comparing the numerical results (open circles) with the exact solution (solid lines) of $E_3(x, y, t)$. Obviously, small derivations from the exact cylinder waves are visible; these result from reflections at the corners of the computational domain. The exact origin of this phenomenon is not completely understood up to now. A global comparison of the spatial behavior between the exact cylinder wave solution and the numerically

obtained electric field E_3 at $t = 400\text{ns}$ is given in Figure 12. The general features discussed above can also be seen in more detail from this snapshot.

The second test case treats the so-called enlarged dipole which means that the electromagnetic fields are excited by the time-dependent current density of the form

$$J_x(t) = \begin{cases} J_0 \cos(\omega t) & (x, y) \in \mathcal{D} \\ 0 & \text{elsewhere} \end{cases}, \quad (6.3)$$

where J_0 and ω are chosen equal to 1A/m^2 and $0.1508/\text{ns}$, respectively. \mathcal{D} is a discrete set of points given by

$$\mathcal{D} = \{(x_i, y_j) \mid x_i = 49.75\text{m} + i\Delta x; y_j = 49.75\text{m} + j\Delta y; -3 \leq i \leq 3, -1 \leq j \leq 1\}.$$

The grid spacing for this example is $\Delta x = \Delta y = 0.5\text{m}$. This enlarged dipole problem does not have an exact analytical solution. However, the long range fields of this problem should be similar to those of the Hertz dipole (cf. Appendix F). In this paper we circumvent the analytical solution and proceed in the following way: First, we generate a numerical solution for the large domain $G_L = \{(x, y) \mid 0 \leq x \leq 100\text{m}; 0 \leq y \leq 100\text{m}\}$ as a reference. To avoid possible influence of the boundary ∂G_L , we consider only times for which the electromagnetic signals do not reach this border. Secondly, we compute the results for the small computational domain $G_S = \{(x, y) \mid 30\text{m} \leq x \leq 70\text{m}; 30\text{m} \leq y \leq 70\text{m}\}$ and compare these so-called "spot check" result with the reference solutions. At the surface ∂G_S open boundary conditions are imposed. Typical results for the enlarged dipole test block are shown in Figures 13 to 15 at the time $t = 150\text{ns}$, where the time-step size Δt is set equal to 1.25ns . The field solver used for these calculations is based on second-order extended FV methods, where the slopes are computed with the aid of a limiter proposed by van Leer (see, e.g. [39]). A quantitative comparison between the spot check (open circles) and reference solution for the electric field E_1 and the magnetic induction B_3 is shown in Figure 13 and 15, respectively. Each of the four slices parallel to the y -axis indicates that the agreement between both numerical results is quite acceptable. Nevertheless, the cut close to the open boundary of the small domain ∂G_S reveals reflections from the boundary, especially in the B_1 -plot of Figure 15. The qualitative spatial behavior of E_2 for the spot check as well as the reference solution at $t = 150\text{ns}$ is given in Figure 14. We observe deviations of the spot check from the reference solution where the amplitudes are small compared to the absolute maximum amplitudes.

To assess the numerical results of the two test cases, we can conclude that the FV field solver for the inhomogeneous Maxwell equations works rather well and is very robust. Nevertheless, further investigations are necessary to increase the reliability of the numerical realization of the open boundary conditions. A further possible test problem for this study may be the exactly solvable half-plane diffraction problem [53].

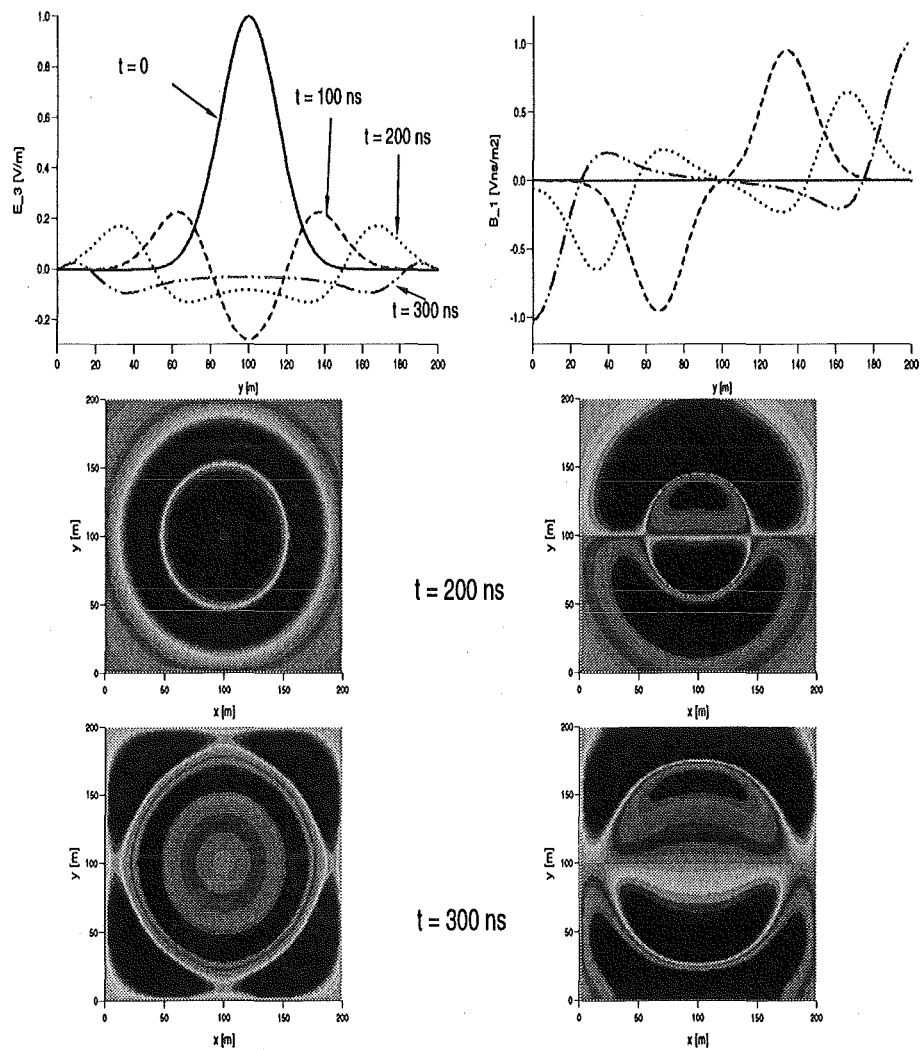


Figure 1: Overview of the numerical results of a TM wave calculation where the computational domain is surrounded by a perfectly conducting wall. For the B_2 -field along the x -axis (not shown here) similar features are found to those of B_1 .

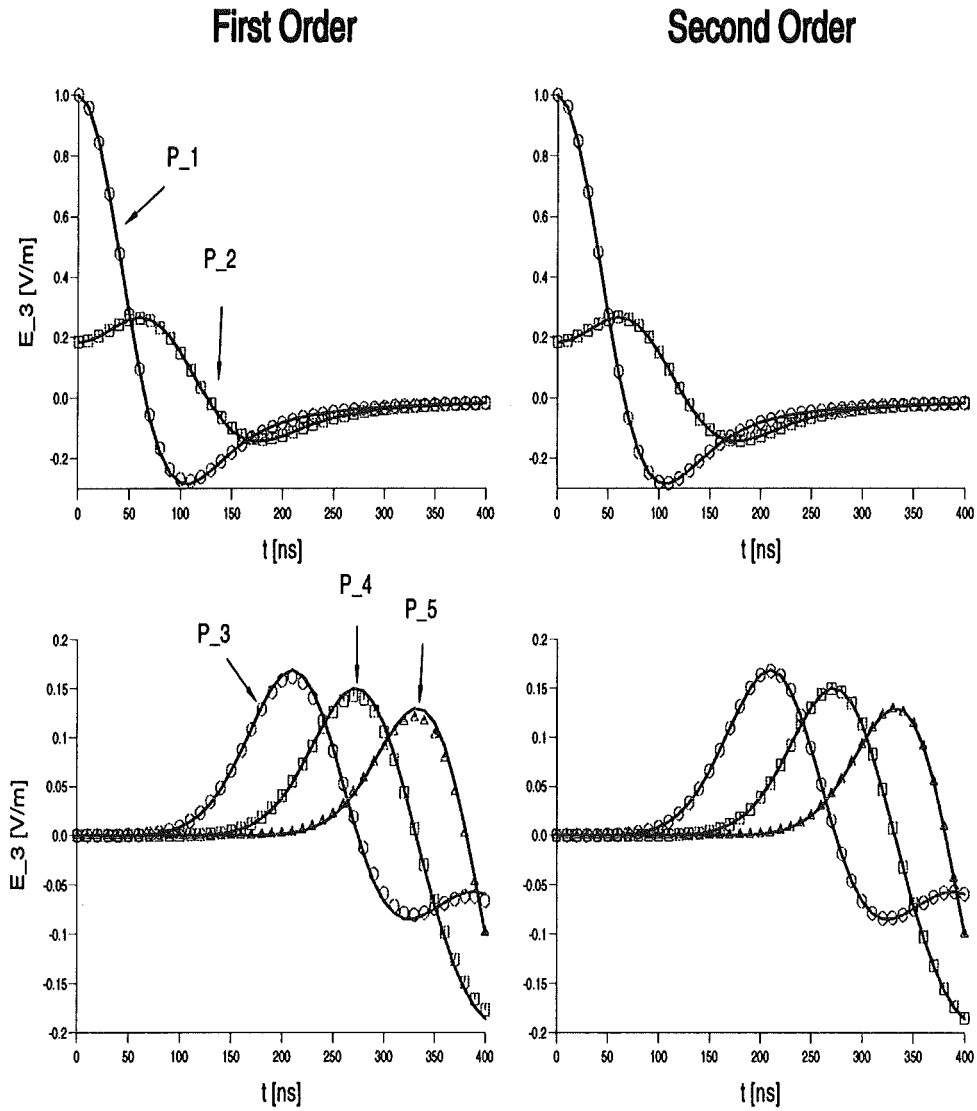


Figure 2: Temporal evolution of the third component of the electric field E_3 on the nanosecond time scale for five different but fixed points in space obtained from a TM wave calculation. The numerical results from a first- (left) and second-order (right) accurate FV scheme are compared with the exact solutions (solid lines).

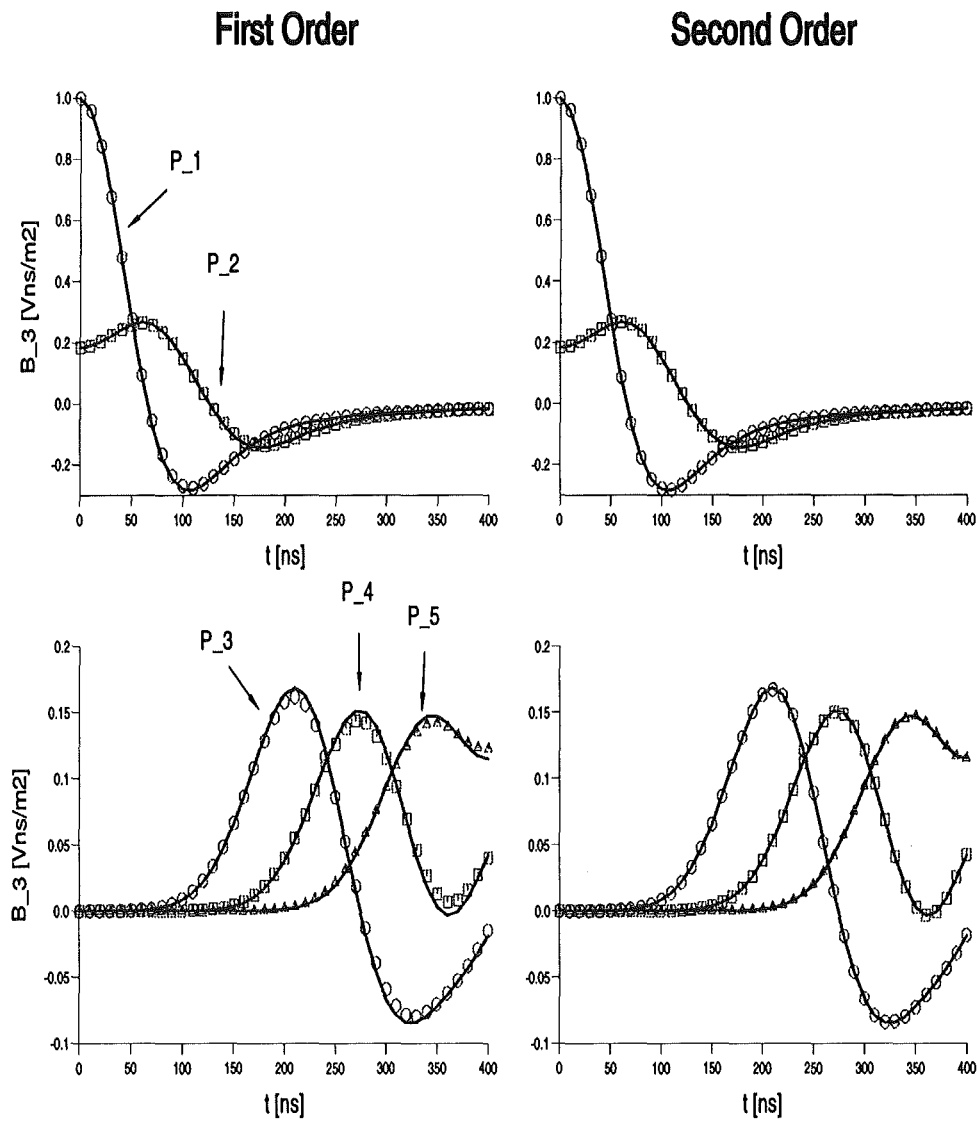


Figure 3: Temporal evolution of the third component of the magnetic induction B_3 on the nanosecond time scale for five different but fixed points in space found from a TE wave calculation. The numerical results obtained from a first- (left) and second-order (right) FV dimensional-splitting scheme are compared with the exact solutions (solid lines).

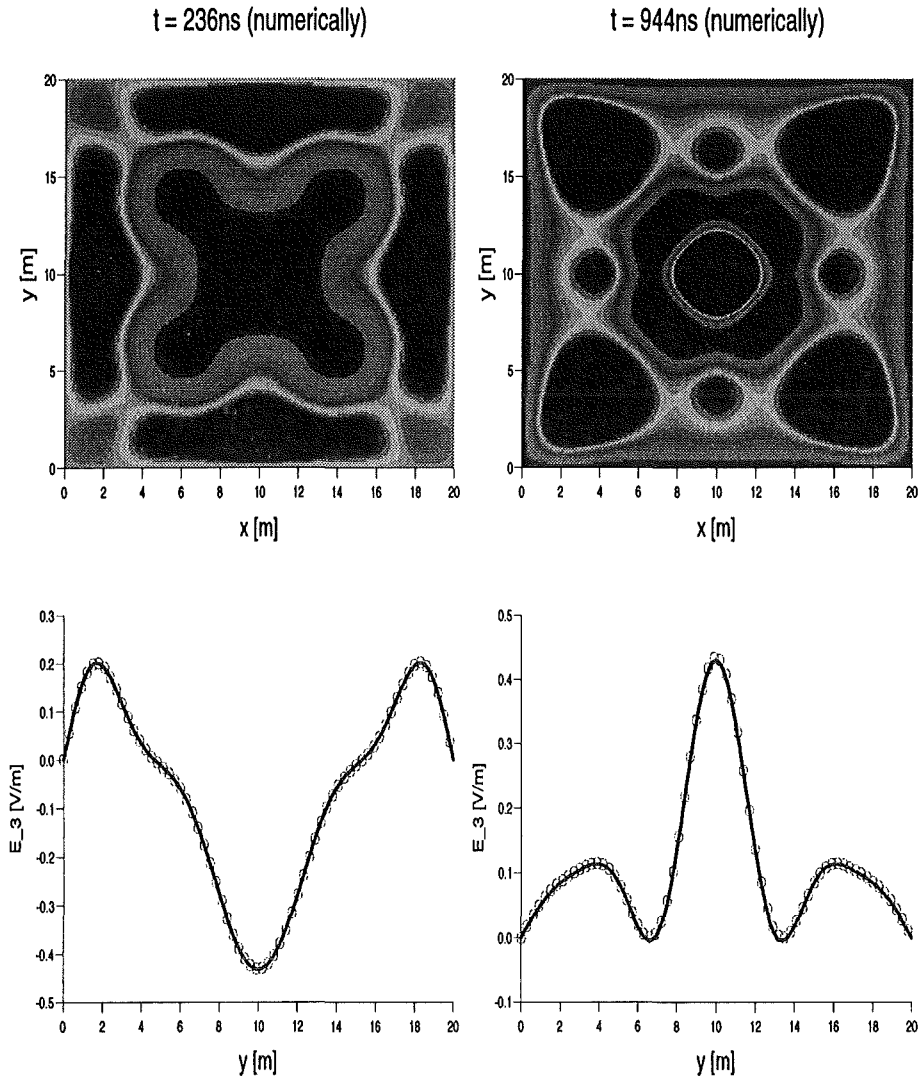


Figure 4: Contour plot of the electric field $E_3(x, y, t)$ for two different times which is initially excited by a Gaussian profile. In the lower part a comparison between the exact (solid line) and numerical calculated (open circles) solution is given for a slice parallel to the y -axis at $x = 10\text{m}$ for $t = 236\text{ns}$ (left) and $t = 944\text{ns}$ (right). The numerical results are obtained with a FD based Maxwell field solver.

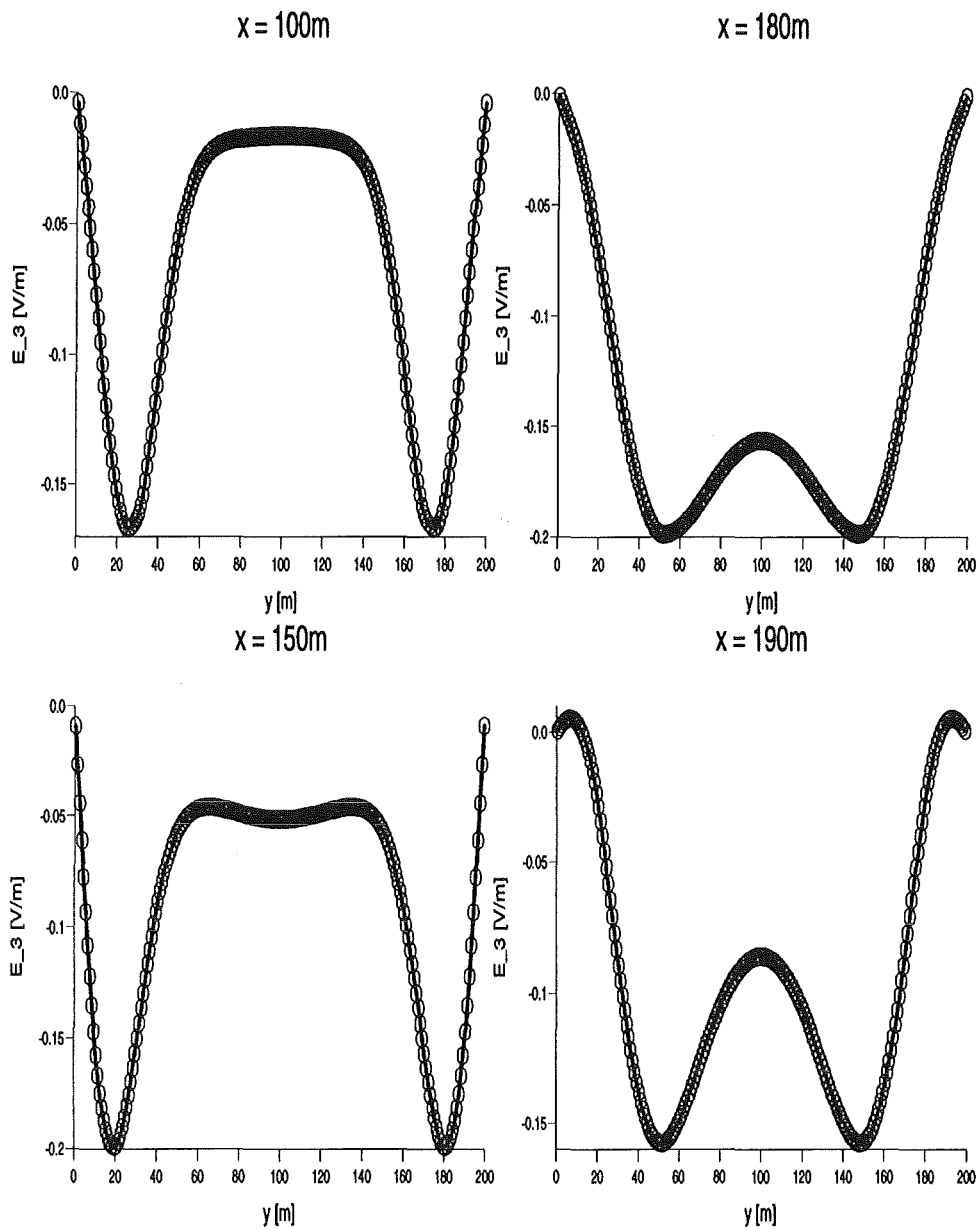


Figure 5: Comparison of the results obtained from the field solvers based on the MUSCL-ansatz (open circles) and the dimensional-splitting (reference solution; solid lines) method. Four slices parallel to the y -axis are shown of the electric field E_3 at $t = 400\text{ns}$.

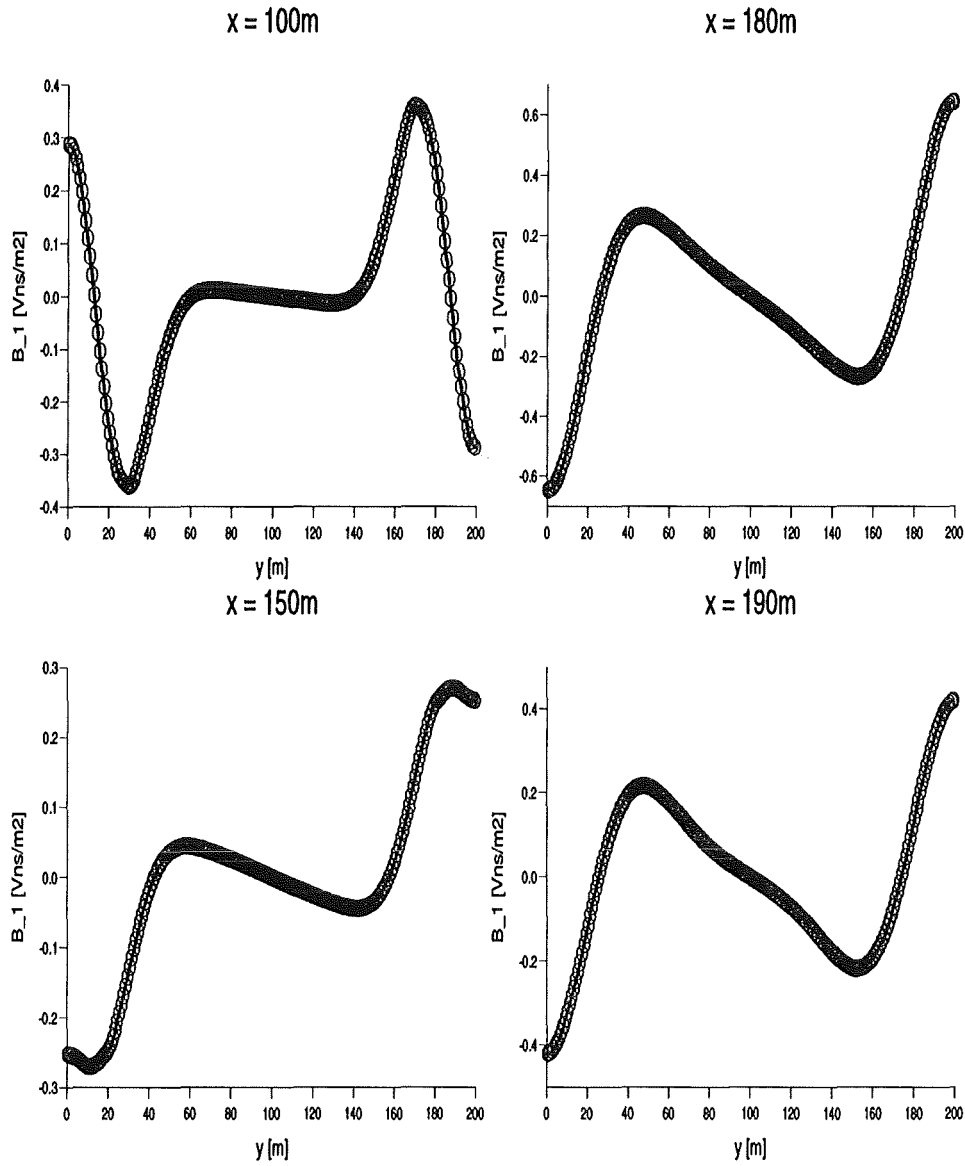


Figure 6: Comparison of the results obtained from the field solvers based on the MUSCL-ansatz (open circles) and the dimensional-splitting (reference solution; solid lines) method. Four slices parallel to the y -axis are shown of the magnetic induction B_1 at $t = 400\text{ns}$.

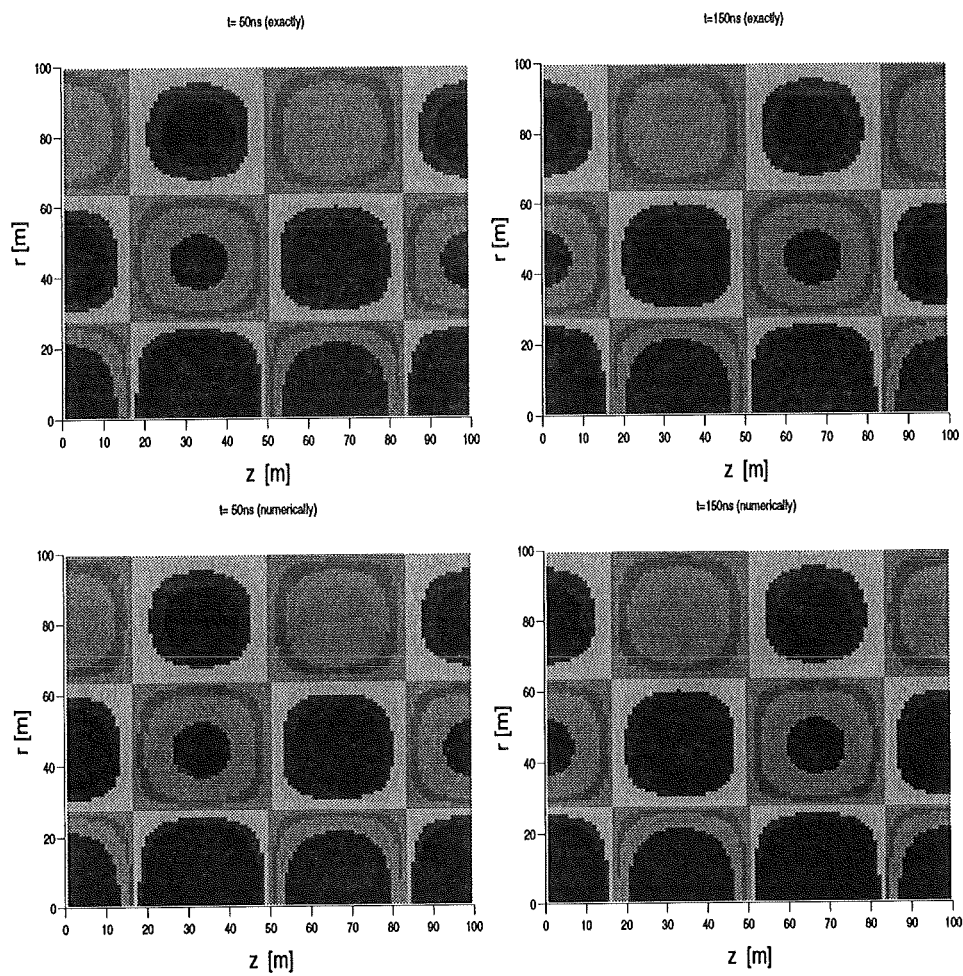


Figure 7: Contour plots of the TM electric field $E_z(z, r, t)$ obtained from a second-order accurate FV method field solver using the dimensional-splitting ansatz at $t = 50\text{ns}$ and $t = 150\text{ns}$. For comparison the exact solutions at these times are shown in the upper two pictures.

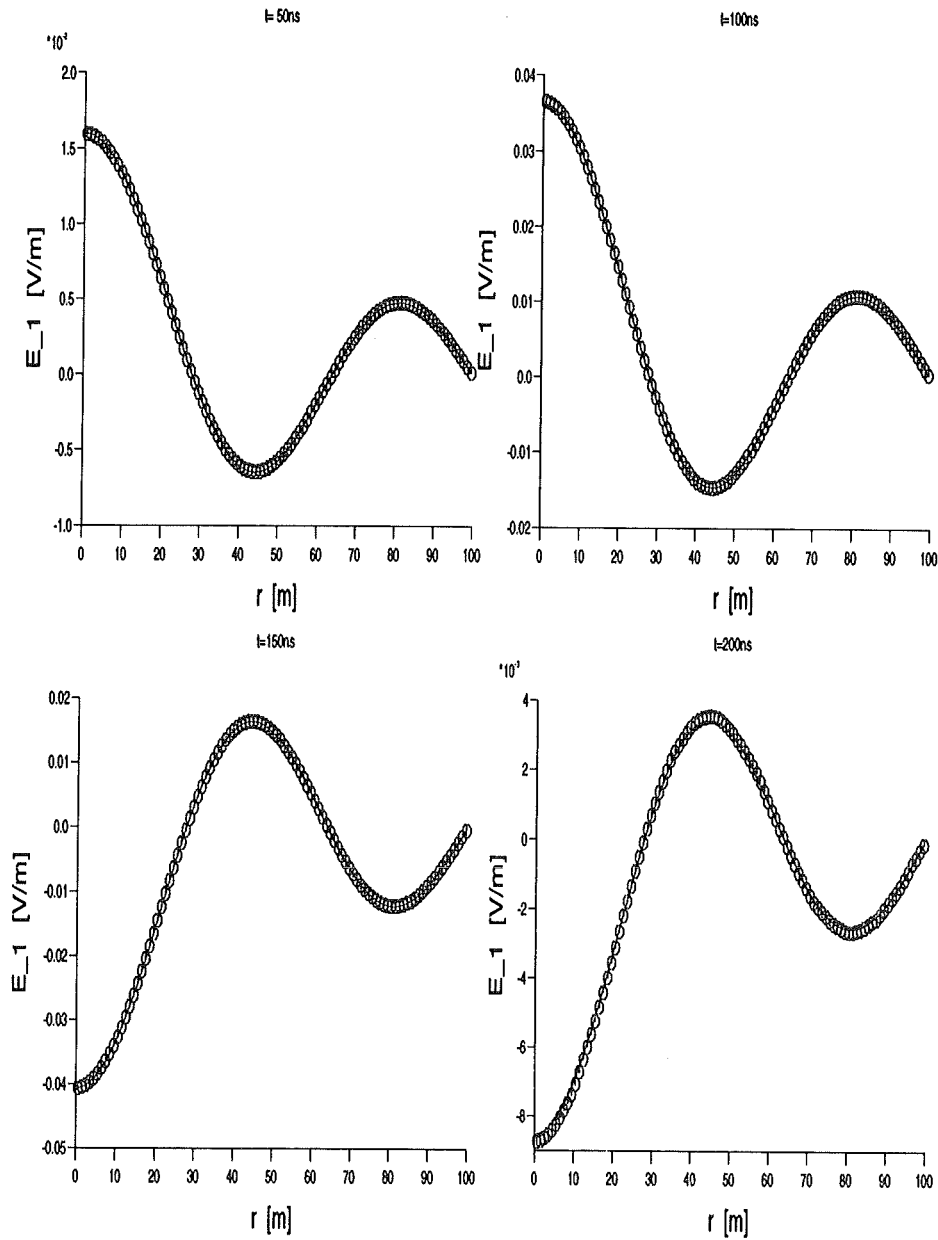


Figure 8: Comparison between the electric field $E_z(z, r, t)$ calculated for a TM wave with a second-order accurate FV field solver (open circles) and the exact solution (solid lines) for four different times. The plots are recorded for $z = 50$ m.

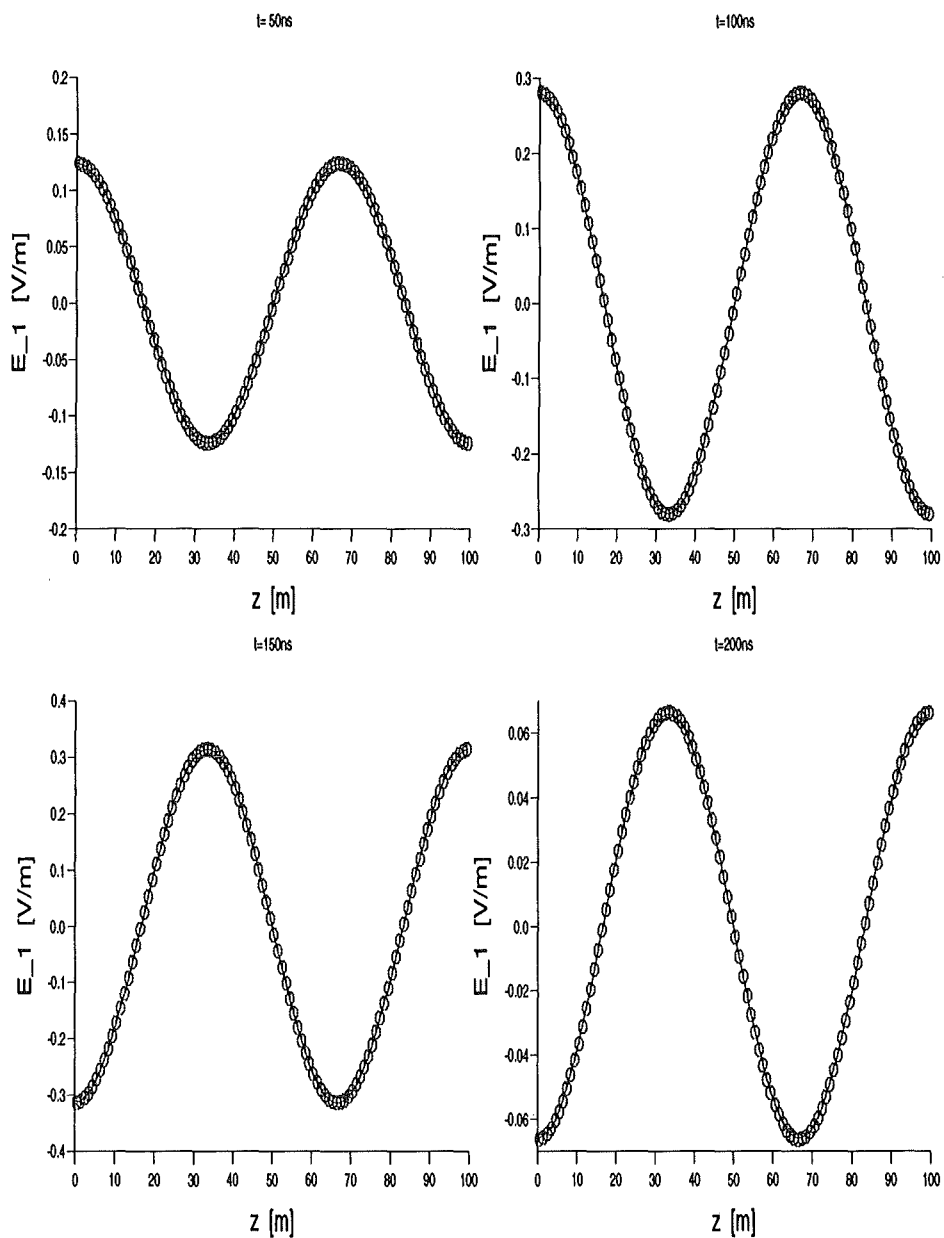


Figure 9: Comparison between the electric field $E_z(z, r, t)$ calculated for a TM wave with a second-order accurate FV field solver (open circles) and the exact solution (solid lines) for four different times. The plots are recorded for $r = 50\text{m}$.

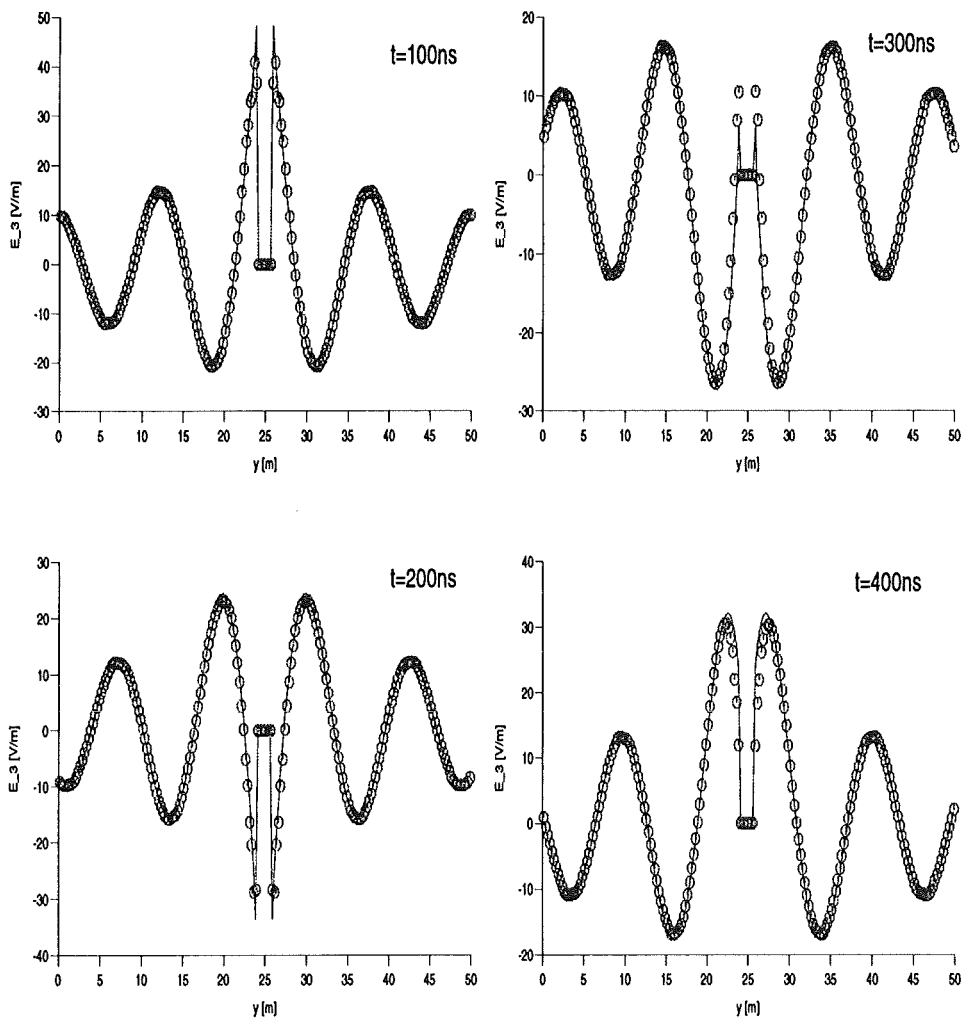


Figure 10: Comparison between the exact cylinder wave solution (solid lines) and the second-order FV result (open circles) for the third component of the electric field for a two-dimensional dipole. The plots show $E_3(x_0, y, t)$ for $x_0 = 24.875$ m.

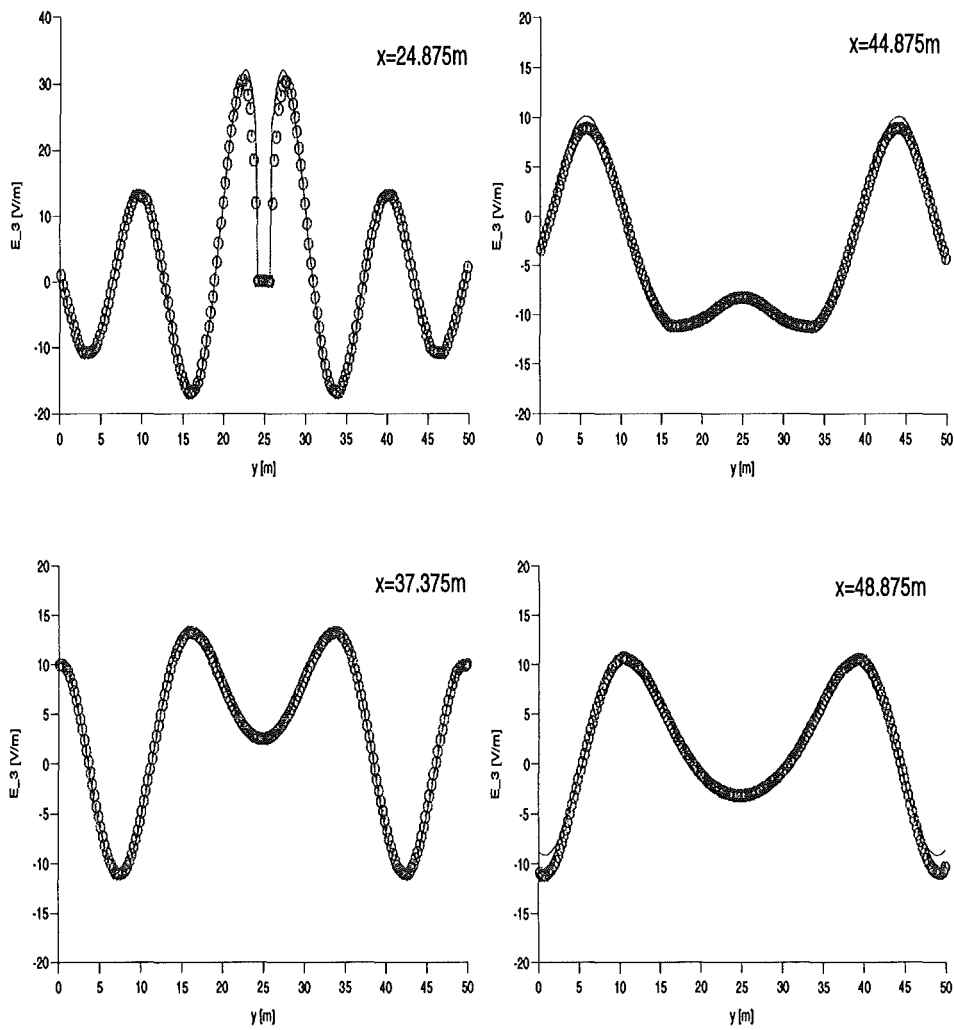


Figure 11: Four slices parallel to the y -axis to compare the numerical (open circles) and exact (solid lines) solution of the two-dimensional dipole at $t = 400\text{ns}$. The numerical results are obtained from a second-order accurate FV scheme.

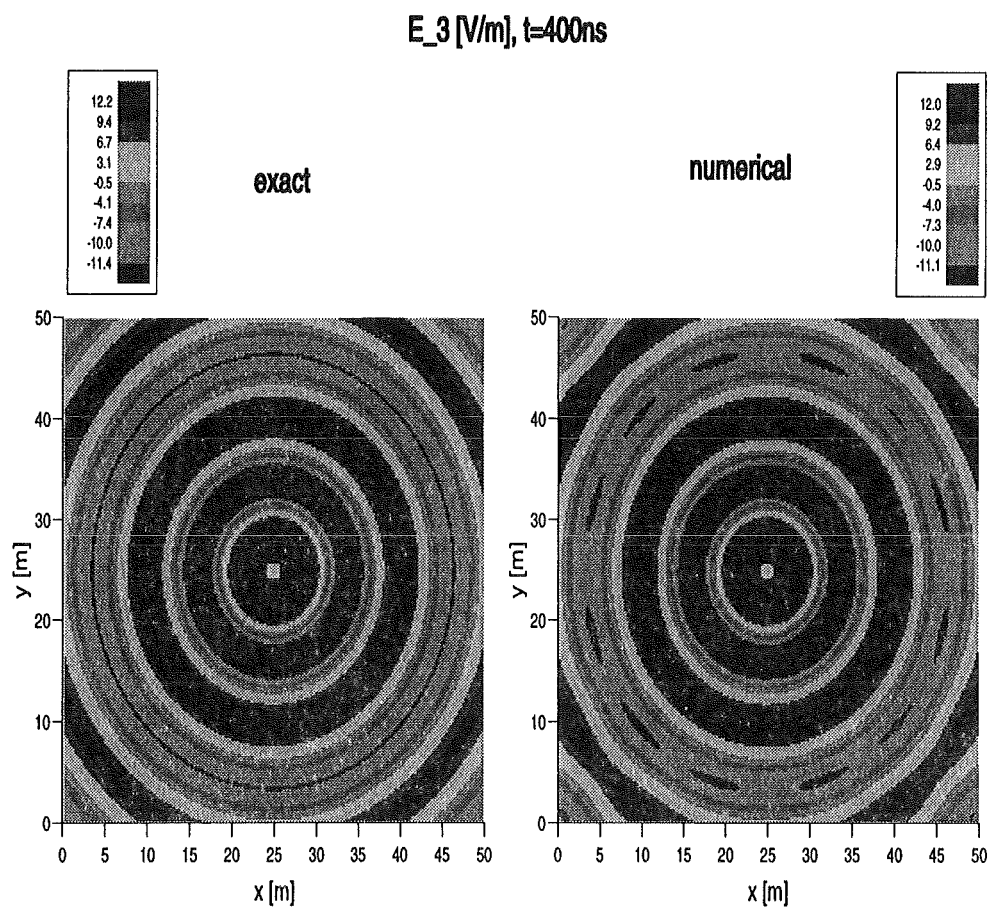


Figure 12: Contour plots of the electric field $E_3(z, r, t)$ at $t = 400\text{ns}$ for the two-dimensional dipole. The numerical results are obtained with a second-order accurate FV method field solver.

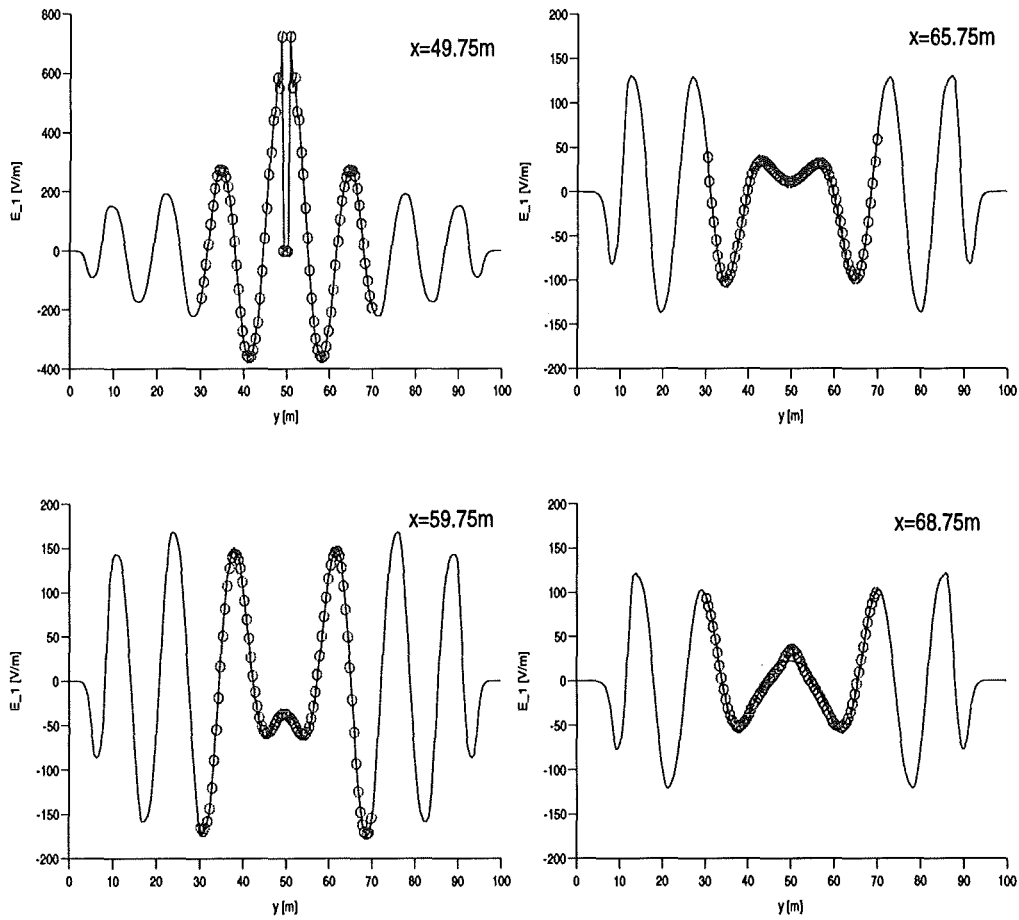


Figure 13: Comparison of the spot check (open circles) and reference (solid lines) solution of E_1 at $t = 150$ ns for four cuts parallel to the y -axis. Both enlarged dipole results are obtained with a second-order FV field solver.

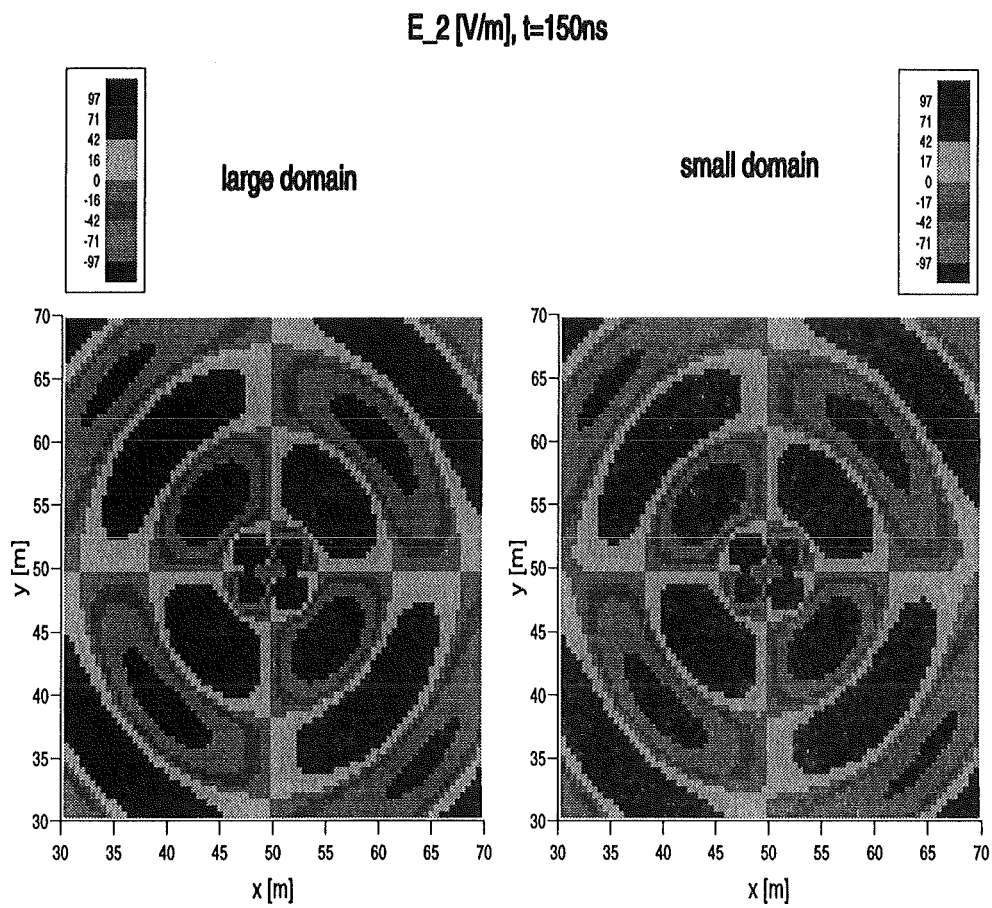


Figure 14: Contour plot of the enlarged electric dipole field E_2 at $t = 150\text{ns}$ for a large (left) and small (right) computational domain. The numerical calculations are carried out with a FV field solver.

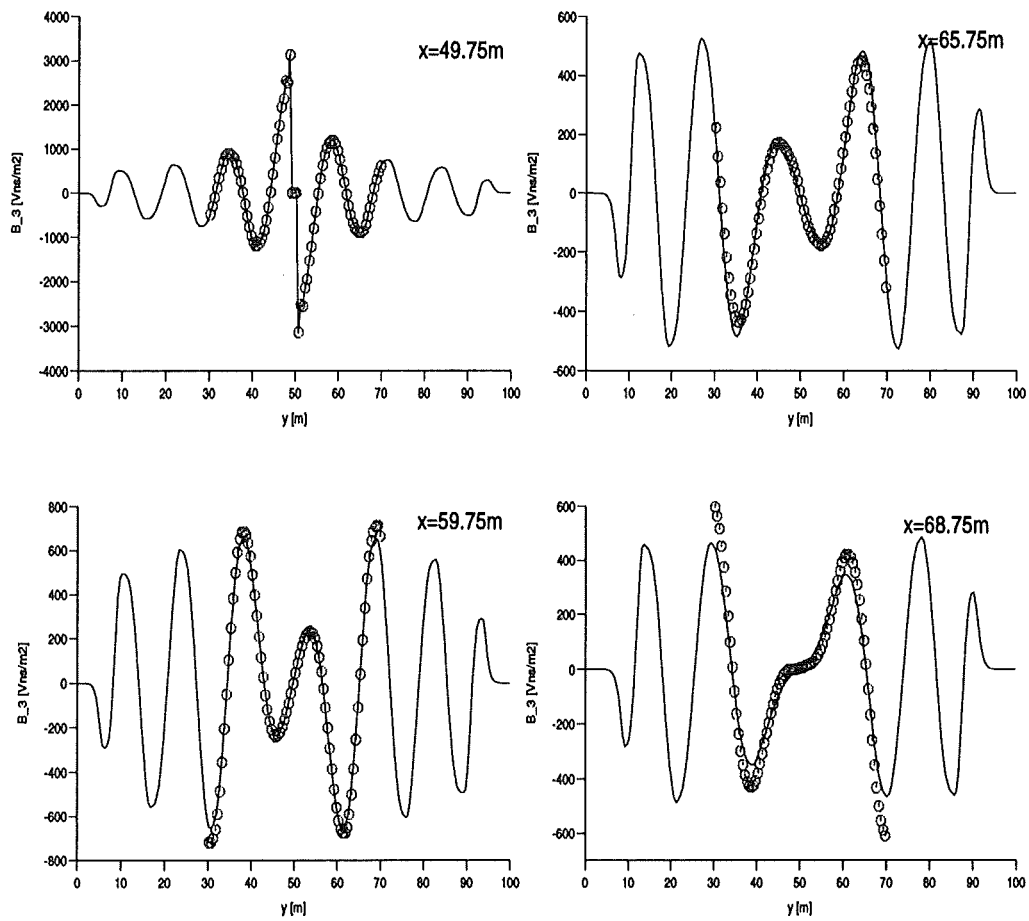


Figure 15: Second-order FV field solver results for the magnetic induction B_3 at $t = 150\text{ns}$ for a small (open circles) and a large (solid lines) computational domain. The slices are recorded parallel to the y -axis.

7 Conclusion and Outlook

Following the modular construction of the newly developed $2\frac{1}{2}$ -dimensional stationary Maxwell-Lorentz program system, the basic strategies in this code are discussed and summarized in this paper.

When computing discrete solutions of a practical field problem in ion diode simulations it is important to model very accurately the complex shape of the technical devices where different kinds of boundary conditions have to be imposed. Therefore, we use extended boundary-fitted coordinate techniques which are integrated in an open CAD-system resulting in the interactive grid generation module InGrid. Beyond the helpful standard auxiliary CAD-tools a lot of additional grid generation tools are realized in this program package. For example, to improve the geometrical accuracy in physically important regions, multizoning techniques are available. Further, InGrid enables us to generate computational grids in two spatial dimensions in a very effective and comfortable manner and delivers suitable computational grids for the existing BFCPIC code in a standardized way. Another aspect which will be important for our future work concerns the adaptivity concept: to get accurate results the spatial resolution has to be refined in regions of pronounced changes of the relevant physical variables. Hence, suitable concepts which allows dynamical local mesh refinement are under consideration. Furthermore, the extension of InGrid to three-dimensional applications is planned for the near future.

The main part of the present report concerns the numerical solution of the nonstationary Maxwell equations in time domain. Because of the nonlinear response of the charged particles, the linear nature of the Maxwell equations is strongly influenced by nonlinear source terms. With respect to this fact, we focussed our attention on the well-known finite-difference (FD) and on finite-volume (FV) methods as suitable concepts to attack Maxwell's equations numerically. Our FV approach is based on the so-called high resolution upwind schemes which are established recently in computational fluid dynamics (CFD), and are known to be very robust even when strong gradients are present. We emphasize that these CFD-based techniques are a new approach in electromagnetics and self-consistent particles simulation. For both the FD as well as the FV approach Maxwell's curl equations are recast in the convenient conservation form as the starting point for numerical approximations. The new FV approach is especially discussed in the scope of two-dimensional quadrilateral grids in more detail; an extension to three spatial dimensions is straightforward. Basic techniques for the FV approximation such as the solution of the Riemann problem and the improvement to higher-order accuracy via well-established MUSCL-schemes are reviewed. Furthermore, different possible boundary conditions such as "perfect conductor", "outer" and "periodic" boundaries etc., are formulated clearly and realized numerically in a proper way. The standard staggered-leapfrog FD approach proposed by Yee is summarized for orthogonal grids in the conservation law frame. This method is non-diffusional

and second-order accurate with respect to time and space. This field solver needs less computational effort, but it is known that it may become unstable in particle simulations and artificial dissipation or implicit stabilization techniques have to be introduced [43, 51]. But, especially, in sub-regions where no strong gradients of the electromagnetic field occur it may be a good alternative. A generalization of the standard FD schemes to boundary-fitted grids is given in [23]; see also [32, 33] for unstructured grids.

Extensive numerical experiments have been performed for test problems formulated for Cartesian as well as cylindrical coordinates. These calculations indicate that the algorithmic transposition of the different methods and the implementation of the resulting algorithms is performed properly and the numerical results agree with analytical solutions in a very acceptable and encouraging way.

First experience has been made with a FV-based field solver where the computational domain is covered by a structured curvilinear quadrilateral grid. The results reveal the strength of the formulation and the robustness of the FV approach. The details of the calculation will be discussed elsewhere [41]. However, further improvements and extensions seem to be important: high-order boundary conditions in the non-reflecting outer case should be reinvestigated and essentially non-oscillatory FV schemes [20] should be available. Furthermore, it should be found out by means of concrete test problems with the entire Maxwell-Lorentz code which of the two field solvers works better and is the most suitable for the final application to ion diode simulations.

The particle treatment is based on the modules of the well-established stationary PIC-code for boundary-fitted coordinates BFCPIC [67]. The new modules are written in such a way that the FV as well as FD schemes are supported. Standard test situations have been checked out to deliver satisfactory results.

The divergence preserving properties of the Maxwell-Lorentz equations are still under investigation. This is a more theoretical problem but has practical impact on the numerical efforts.

An important building block to close the chain of field and particle treatment and consequently to verify the entire Maxwell-Lorentz program system is the particle generation module. At the moment, the field emission of electrically charged particles from the plasma surface is established by applying Gaussian law under the Child-Langmuir condition. However, more realistic scenarios of the response of the plasma surface to the fields inside the computational domain are under discussion [48, 45].

Pre- and post-processing improvements will be pursued throughout the course of this code development. However, it is important to combine different applications to a preliminary graphics package for qualitative and quantitative post-processing. To handle the vast amount of data produced by the Maxwell-Lorentz code, portable

data analyzing tools such as line, surface and volume integrals of the field quantities, differentiation, filtering, Fourier transformation, etc. are absolutely necessary. Hence, a concept containing the foreseeable requirements will be formulated in the course of this year.

Acknowledgements

It is a pleasure to thank S. Illy and E. Borie for numerous stimulating and very helpful discussions and for advice concerning technical details in testing the field solver. Furthermore the authors thank E. Borie for carefully reading the manuscript.

A Maxwell's Equations in Conservation Form

In this appendix we derive the form of Maxwell's equations which is used for the discretization in the finite-difference as well as finite-volume approach. Since we are interested in time-dependent phenomena it is sufficient to consider Maxwell's and Faraday's equation (2.3a), (2.3b), respectively, where the sum of self-consistent and external current density is now replaced by

$$\mathbf{J}(\mathbf{x}, t) = \mathbf{j}^{sc}(\mathbf{x}, t) + \mathbf{j}^{ext}(\mathbf{x}, t) \quad . \quad (1.1)$$

Symmetry considerations play an important role for a lot of physical problems. For our purposes, it is sufficient to investigate the curl of the vector field $\mathbf{V}(x_1, x_2, x_3) = (V_1, V_2, V_3)^T$; $V_i = V_i(x_1, x_2, x_3)$, $i = 1, 2, 3$; for the Cartesian and rotationally symmetrical case. Explicitely, $\nabla \times \mathbf{V}$ is given by

$$(\nabla \times \mathbf{V})_1 = \partial_{x_2} V_3 - \partial_{x_3} V_2 \quad , \quad (1.2a)$$

$$(\nabla \times \mathbf{V})_2 = \partial_{x_3} V_1 - \partial_{x_1} V_3 \quad , \quad (1.2b)$$

$$(\nabla \times \mathbf{V})_3 = \partial_{x_1} V_2 - \partial_{x_2} V_1 \quad , \quad (1.2c)$$

for Cartesian problems, where $(x_1, x_2, x_3) = (x, y, z)$. For cylindrically symmetric problems $\nabla \times \mathbf{V}$ is determined from

$$(\nabla \times \mathbf{V})_1 = \frac{1}{x_2} \partial_{x_2} (x_2 V_3) - \frac{1}{x_2} \partial_{x_3} V_2 \quad , \quad (1.3a)$$

$$(\nabla \times \mathbf{V})_2 = \frac{1}{x_2} \partial_{x_3} V_1 - \partial_{x_1} V_3 \quad , \quad (1.3b)$$

$$(\nabla \times \mathbf{V})_3 = \partial_{x_1} V_2 - \partial_{x_2} V_1 \quad , \quad (1.3c)$$

with $(x_1, x_2, x_3) = (z, r, \varphi)$. Defining the matrices $\mathcal{M}_i \in \mathbb{R}^{3 \times 3}$, $i = 1, 2, 3$, according to

$$\mathcal{M}_1 = \begin{pmatrix} 0 & 0 & 0 \\ 0 & 0 & -1 \\ 0 & 1 & 0 \end{pmatrix} \quad , \quad (1.4a)$$

$$\mathcal{M}_2 = \begin{pmatrix} 0 & 0 & 1 \\ 0 & 0 & 0 \\ -1 & 0 & 0 \end{pmatrix} \quad , \quad (1.4b)$$

$$\mathcal{M}_3 = \frac{1}{x_2^\kappa} \begin{pmatrix} 0 & -1 & 0 \\ 1 & 0 & 0 \\ 0 & 0 & 0 \end{pmatrix} \quad , \quad (1.4c)$$

the curl of the vector field \mathbf{V} can expressed for both, the Cartesian ($\kappa = 0$) and the rotationally symmetric ($\kappa = 1$) case in one formula

$$\nabla \times \mathbf{V} = [\mathcal{M}_1 \partial_{x_1} + \mathcal{M}_2 \partial_{x_2} + \mathcal{M}_3 \partial_{x_3}] \mathbf{V} + \mathbf{S}^{geo} \quad , \quad (1.5a)$$

with

$$\mathbf{S}^{geo} = \left(\kappa \frac{V_3}{x_2}, 0, 0 \right)^T . \quad (1.5b)$$

Since the special structure of the matrices \mathcal{M}_i , it is important to note, especially for notational reasons (see below) that they commute with ∂_{x_i} ; this means that $\mathcal{M}_i \partial_{x_i} \mathbf{V} = \partial_{x_i} \mathcal{M}_i \mathbf{V}$

After this excursion we return to the Maxwell equations (2.3a), (2.3b). Introducing the so-called vector of conserved quantities

$$u = (E_1, E_2, E_3, B_1, B_2, B_3)^T , \quad (1.6a)$$

and defining with (1.4) the block-structured matrices $\mathcal{K}_i \in \mathbb{R}^{6 \times 6}$

$$\mathcal{K}_i = \begin{pmatrix} \mathbf{0} & -c^2 \mathcal{M}_i \\ \mathcal{M}_i & \mathbf{0} \end{pmatrix} ; i = 1, 2, 3 , \quad (1.6b)$$

it is possible to combine (2.3a) and (2.3b) to one very compact equation which reads as

$$\partial_t u + \sum_{i=1}^3 \partial_{x_i} F_i(u) = q(u) . \quad (1.6c)$$

The fluxes \mathcal{F}_i are calculated according to a simple matrix-vector multiplication

$$F_i(u) = \mathcal{K}_i u , \quad (1.6d)$$

and the vector of the source terms ($c^2 \epsilon_0 \mu_0 = 1$)

$$q(u) = -\frac{1}{\epsilon_0} (J_1, J_2, J_3, 0, 0, 0)^T + \frac{\kappa}{x_2} (c^2 B_3, 0, 0, -E_3, 0, 0)^T \quad (1.6e)$$

consists of the sum of the physical (current densities) and geometrical (in the case of rotational symmetry) sources. Sometimes it is desirable to have a more obvious notation for equation (1.6c). Defining the divergence operator and the flux vector, respectively, according to

$$div = (\partial_{x_1}, \partial_{x_2}, \partial_{x_3})^T , \quad (1.7a)$$

$$\mathcal{F} = (F_1, F_2, F_3)^T , \quad (1.7b)$$

we find for (1.6c)

$$\partial_t u + div \mathcal{F}(u) = q(u) . \quad (1.7c)$$

The equations (1.6c) and (1.7c) both have the form of an evolution equation, and will be called in the following as the conservation form of the nonstationary Maxwell equations (2.3a) and (2.3b).

Restricting ourselves to two spatial dimensions, the conservation form for curvilinear coordinates can easily be derived for the conservation law (1.6c). Let T be the transformation $T : G^* \rightarrow G$ with $(\xi, \eta) \mapsto (x, y)$; $(\xi, \eta) \in G^* \subseteq \mathbb{R}^2$, $(x, y) \in G \subseteq \mathbb{R}^2$ (cf. Figure 3.1). Suppose that the derivation of the mappings $x = x(\xi, \eta)$, $y = y(\xi, \eta)$

are continuous. Then the matrix \mathcal{T} and the inverse matrix \mathcal{T}^{-1} of the transformation T are given by

$$\mathcal{T} = \begin{pmatrix} x_\xi & x_\eta \\ y_\xi & y_\eta \end{pmatrix}, \quad (1.8a)$$

$$\mathcal{T}^{-1} = \frac{1}{|\mathcal{T}|} \begin{pmatrix} y_\eta & -x_\eta \\ -y_\xi & x_\xi \end{pmatrix} = \begin{pmatrix} \xi_x & \xi_y \\ \eta_x & \eta_y \end{pmatrix}, \quad (1.8b)$$

where it is assumed that the determinant of \mathcal{T}

$$|\mathcal{T}| = x_\xi y_\eta - x_\eta y_\xi \quad (1.8c)$$

is not equal to zero. Applying the chain rule we obtain, for example, for

$$\frac{\partial F_i}{\partial x} = \frac{\partial F_i(u(\xi, \eta))}{\partial \xi} \xi_x + \frac{\partial F_i(u(\xi, \eta))}{\partial \eta} \eta_x. \quad (1.9)$$

Since (1.6d), $F_i(\alpha u) = \alpha F_i(u)$. Assuming that this property holds also for q , we find with (1.8b), the abbreviation

$$\hat{u} = |\mathcal{T}|u, \quad (1.10a)$$

and the additional assumption that the transformation is two times continuous differentiable

$$\partial_t \hat{u} + \partial_\xi [\xi_x F_1(\hat{u}) + \xi_y F_2(\hat{u})] + \partial_\eta [\eta_x F_1(\hat{u}) + \eta_y F_2(\hat{u})] = q(\hat{u}). \quad (1.10b)$$

This is the conservation form of the Maxwell equations for curvilinear coordinates generated by the transformation T in the two-dimensional case. Introducing the two-dimensional operator

$$\text{div}_{\xi, \eta} = (\partial_\xi, \partial_\eta)^T, \quad (1.11a)$$

and defining the new flux vector $\tilde{\mathcal{F}}$ according to

$$\tilde{\mathcal{F}}(\hat{u}) = (\tilde{F}_1(\hat{u}), \tilde{F}_2(\hat{u}))^T, \quad (1.11b)$$

with

$$\tilde{F}_1 = \xi_x F_1 + \xi_y F_2, \quad (1.11c)$$

$$\tilde{F}_2 = \eta_x F_1 + \eta_y F_2, \quad (1.11d)$$

equation (1.10b) can be written in a compact form which reads as

$$\partial_t \hat{u} + \text{div}_{\xi, \eta} \tilde{\mathcal{F}}(\hat{u}) = q(\hat{u}), \quad (1.11e)$$

and is the two-dimensional counterpart of (1.7c) for curvilinear coordinates.

B Two-dimensional FV Scheme in Cartesian Grids

This appendix summarizes briefly the basic formulas of an explicit two-dimensional FV-scheme based directly on the approximation from an equidistant rectangular grid. The situation under consideration is seen in Figure B.1 for the grid zone V_{ij} . Obviously, the area of V_{ij} is given by $|V_{ij}| = \Delta x \Delta y$ and the length of to opposite edges is $|S_{ij,1}| = |S_{ij,3}| = x_{i+1/2} - x_{i-1/2} = \Delta x$ and $|S_{ij,2}| = |S_{ij,4}| = y_{i+1/2} - y_{i-1/2} = \Delta y$. For the special grid zone depicted in Figure B.1, the outward directed unit

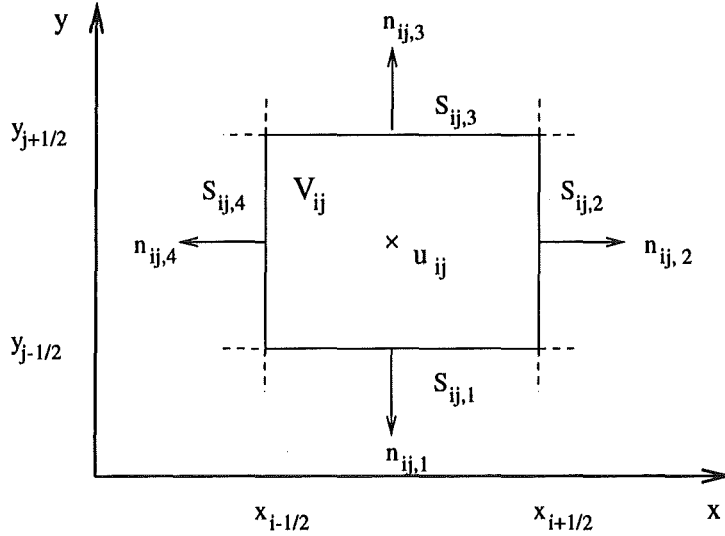


Figure 1: Grid cell V_{ij} of a rectangular cartesian grid

normals are given by $n_{ij,2} = (1, 0)^T$, $n_{ij,3} = (0, 1)^T$, $n_{ij,1} = -n_{ij,3}$ and $n_{ij,4} = -n_{ij,2}$. With that, the sum in equation (4.3d) can be approximated by

$$\sum_{\beta=1}^4 \int_{S_{ij,\beta}} \mathcal{F}(u) n_{ij,\beta} dS = \frac{\Delta t}{\Delta x} \mathcal{K}_1 [u(x_{i+1/2}, y_j, t_n) - u(x_{i-1/2}, y_j, t_n)] + \frac{\Delta t}{\Delta y} \mathcal{K}_2 [u(x_i, y_{j+1/2}, t_n) - u(x_i, y_{j-1/2}, t_n)] . \quad (2.1)$$

The solution of u has to be determined at the interface of four neighboring grid cells. Solving RPs analogous to Section 4.1.1 at each edge $S_{ij,\beta}$ of the rectangular grid zone V_{ij} , the numerical fluxes $g_{i+1/2,j}$ and $h_{i,j+1/2}$ can be calculated as follows

$$\begin{aligned} g_{i+1/2,j} &= \mathcal{K}_1 u(x_{i+1/2}, y_j, t_n) \\ &= \mathcal{K}_1^+ u_{i,j}^n + \mathcal{K}_1^- u_{i+1,j}^n , \end{aligned} \quad (2.2a)$$

and

$$\begin{aligned} h_{i,j+1/2} &= \mathcal{K}_2 u(x_i, y_{j+1/2}, t_n) \\ &= \mathcal{K}_2^+ u_{i,j}^n + \mathcal{K}_2^- u_{i,j+1}^n . \end{aligned} \quad (2.2b)$$

Inserting (2.2a), (2.2b) into the sum (2.1), we get the following scheme for the cell average u_{ij}^n

$$u_{ij}^{n+1} = u_{ij}^n - \frac{\Delta t}{\Delta x} (g_{i+1/2,j} - g_{i-1/2,j}) - \frac{\Delta t}{\Delta y} (h_{i,j+1/2} - h_{i,j-1/2}) + \Delta t q_{i,j}^n. \quad (2.2c)$$

This is the two-dimensional explicit FV scheme for rectangular cartesian grids.

C Unit Normals and Area of a quadrilateral Grid Zone

Inspecting equation (4.11), it is obvious that we need the components of the normals $n_{ij,\beta}$ at the middle of each edge $S_{ij,\beta}$ and the area $|V_{ij}|$ of the quadrilateral grid cell V_{ij} . For sake of notational clarity, a part of the grid shown in Figure 3.2 is given in Figure C.1. The area $|V_{ij}|$ is obtained by dividing the quadrilateral grid cell first

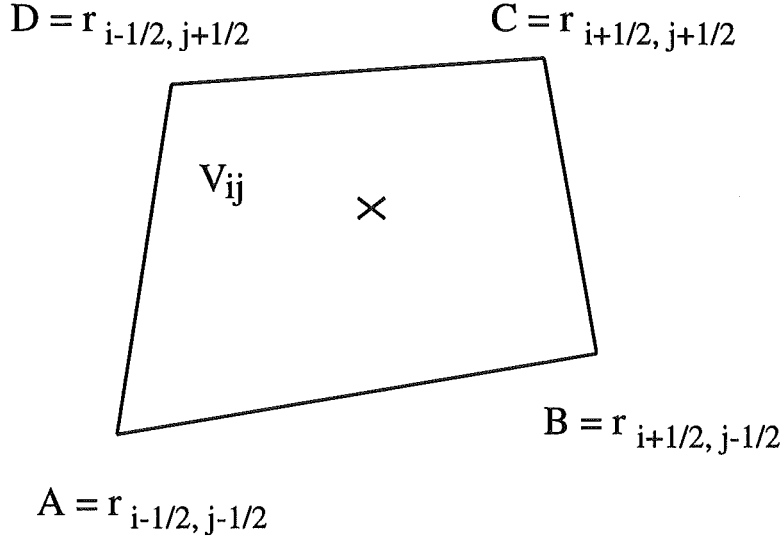


Figure 1: Notation for a quadrilateral grid zone: $r_{i,j} = (x_{i,j}, y_{i,j})^T$.

into triangles, for example, ABC and CDA . Calculating the area of each triangle and summing up these areas results in

$$\begin{aligned}
 |V_{ij}| &= \frac{1}{2} \left\{ x_{i-1/2, j-1/2} (y_{i+1/2, j-1/2} - y_{i-1/2, j+1/2}) \right. \\
 &\quad + x_{i+1/2, j-1/2} (y_{i+1/2, j+1/2} - y_{i-1/2, j-1/2}) \\
 &\quad + x_{i+1/2, j+1/2} (y_{i-1/2, j+1/2} - y_{i+1/2, j-1/2}) \\
 &\quad \left. + x_{i-1/2, j+1/2} (y_{i-1/2, j-1/2} - y_{i+1/2, j+1/2}) \right\}, \quad (3.3)
 \end{aligned}$$

for the quadrilateral grid zone, where the notation is given in Figure C.1.

The unit normals at the middle of each edge can be expressed with the aid of the transformation T introduced in Appendix A. If T is at least two times differentiable and not singular, we find

$$n = \frac{1}{\sqrt{x_\eta^2 + y_\eta^2}} \begin{pmatrix} -y_\eta \\ x_\eta \end{pmatrix}, \quad (3.4a)$$

for a normal on ξ =constant lines and

$$n = \frac{1}{\sqrt{x_\xi^2 + y_\xi^2}} \begin{pmatrix} -y_\xi \\ x_\xi \end{pmatrix} \quad (3.4b)$$

on lines where $\eta=\text{constant}$. The derivatives occuring in (3.4) are approximated according to

$$(x_\xi)_{i,j+1/2} = \frac{x_{i+1/2,j+1/2} - x_{i-1/2,j+1/2}}{\Delta\xi}, \quad (3.5a)$$

$$(x_\eta)_{i+1/2,j} = \frac{x_{i+1/2,j+1/2} - x_{i+1/2,j-1/2}}{\Delta\eta}, \quad (3.5b)$$

$$(y_\xi)_{i,j+1/2} = \frac{y_{i+1/2,j+1/2} - y_{i-1/2,j+1/2}}{\Delta\xi}, \quad (3.5c)$$

$$(y_\eta)_{i+1/2,j} = \frac{y_{i+1/2,j+1/2} - y_{i+1/2,j-1/2}}{\Delta\eta}, \quad (3.5d)$$

where $\Delta\xi$ and $\Delta\eta$ denote the distance of the grid lines in the logical grid. When calculating the unit normals from

$$(x_\xi)_{i,j} = \frac{1}{2} \left((x_\xi)_{i,j+1/2} + (x_\xi)_{i,j-1/2} \right), \quad (3.6a)$$

$$(x_\eta)_{i,j} = \frac{1}{2} \left((x_\eta)_{i+1/2,j} + (x_\eta)_{i-1/2,j} \right), \quad (3.6b)$$

$$(y_\xi)_{i,j} = \frac{1}{2} \left((y_\xi)_{i,j+1/2} + (y_\xi)_{i,j-1/2} \right), \quad (3.6c)$$

$$(y_\eta)_{i,j} = \frac{1}{2} \left((y_\eta)_{i+1/2,j} + (y_\eta)_{i-1/2,j} \right), \quad (3.6d)$$

the values $\Delta\xi$ and $\Delta\eta$ are not needed. The determinant of the transformation matrix \mathcal{T} can be approximated according to

$$(|\mathcal{T}|)_{i,j} = (x_\xi)_{i,j}(y_\eta)_{i,j} - (x_\eta)_{i,j}(y_\xi)_{i,j}, \quad (3.7)$$

which is another possibility to calculate $|V_{ij}|$ with (3.6a-d).

D Miscellaneous Properties of the Matrices \mathcal{K}_i

In the following we summarize the essential properties of the matrices \mathcal{K}_1 and \mathcal{K}_2 , explicitly given by

$$\mathcal{K}_1 = \begin{pmatrix} 0 & 0 & 0 & 0 & 0 & 0 \\ 0 & 0 & 0 & 0 & 0 & c^2 \\ 0 & 0 & 0 & 0 & -c^2 & 0 \\ 0 & 0 & 0 & 0 & 0 & 0 \\ 0 & 0 & -1 & 0 & 0 & 0 \\ 0 & 1 & 0 & 0 & 0 & 0 \end{pmatrix}, \quad (4.1a)$$

$$\mathcal{K}_2 = \begin{pmatrix} 0 & 0 & 0 & 0 & 0 & -c^2 \\ 0 & 0 & 0 & 0 & 0 & 0 \\ 0 & 0 & 0 & c^2 & 0 & 0 \\ 0 & 0 & 1 & 0 & 0 & 0 \\ 0 & 0 & 0 & 0 & 0 & 0 \\ -1 & 0 & 0 & 0 & 0 & 0 \end{pmatrix}, \quad (4.1b)$$

where c denotes the velocity of light. It is found that the eigenvalues of both matrices are the same:

$$\Lambda = \text{diag}(-c, -c, 0, 0, c, c), \quad (4.1c)$$

where Λ is a diagonal matrix. Since two eigenvalues coincide, respectively, three classes of waves with different propagating velocities $\lambda_1 = \lambda_2 = -c$, $\lambda_3 = \lambda_4 = 0$ and $\lambda_5 = \lambda_6 = c$ occur. The right and left eigenvectors of \mathcal{K}_1 are the columns and rows of the matrices

$$\mathcal{R}_1 = (r^1, \dots, r^6)_{\mathcal{K}_1} = \begin{pmatrix} 0 & 0 & 1 & 0 & 0 & 0 \\ -c & 0 & 0 & 0 & c & 0 \\ 0 & c & 0 & 0 & 0 & -c \\ 0 & 0 & 0 & 1 & 0 & 0 \\ 0 & 1 & 0 & 0 & 0 & 1 \\ 1 & 0 & 0 & 0 & 1 & 0 \end{pmatrix}, \quad (4.2a)$$

$$\mathcal{R}_1^{-1} = (l^1, \dots, l^6)_{\mathcal{K}_1}^T = \frac{1}{2c} \begin{pmatrix} 0 & -1 & 0 & 0 & 0 & c \\ 0 & 0 & 1 & 0 & c & 0 \\ 2c & 0 & 0 & 0 & 0 & 0 \\ 0 & 0 & 0 & 2c & 0 & 0 \\ 0 & 1 & 0 & 0 & 0 & c \\ 0 & 0 & -1 & 0 & c & 0 \end{pmatrix}, \quad (4.2b)$$

respectively. For the right and left eigenvectors of \mathcal{K}_2 we get

$$\mathcal{R}_2 = (r^1, \dots, r^6)_{\mathcal{K}_2} = \begin{pmatrix} c & 0 & 0 & 0 & -c & 0 \\ 0 & 0 & 1 & 0 & 0 & 0 \\ 0 & c & 0 & 0 & 0 & -c \\ 0 & -1 & 0 & 0 & 0 & -1 \\ 0 & 0 & 0 & 1 & 0 & 0 \\ 1 & 0 & 0 & 0 & 1 & 0 \end{pmatrix}, \quad (4.3a)$$

$$\mathcal{R}_2^{-1} = (l^1, \dots, l^6)_{\mathcal{K}_2}^T = \frac{1}{2c} \begin{pmatrix} 1 & 0 & 0 & 0 & 0 & c \\ 0 & 0 & 1 & -c & 0 & 0 \\ 0 & 2c & 0 & 0 & 0 & 0 \\ 0 & 0 & 0 & 0 & 2c & 0 \\ -1 & 0 & 0 & 0 & 0 & c \\ 0 & 0 & -1 & -c & 0 & 0 \end{pmatrix}. \quad (4.3b)$$

Since the eigenvalues of \mathcal{K}_1 and \mathcal{K}_2 are elements of \mathbb{R} and the right eigenvectors are linearly independent, the system $\partial_t u + \mathcal{K}_i \partial_x u = 0$, $i = 1, 2$ is strictly hyperbolic.

With (4.2), (4.3) and

$$|\Lambda| = \text{diag}(c, c, 0, 0, c, c), \quad (4.4a)$$

we obtain

$$|\mathcal{K}_i| = \mathcal{R}_i |\Lambda| \mathcal{R}_i^{-1} \quad (4.4b)$$

and from that, the matrices

$$\mathcal{K}_i^\pm = \frac{1}{2} (\mathcal{K}_i \pm |\mathcal{K}_i|), \quad i = 1, 2, \quad (4.4c)$$

can be calculated. Explicitly \mathcal{K}_1^\pm and \mathcal{K}_2^\pm are given by:

$$\mathcal{K}_1^\pm = \frac{1}{2} \begin{pmatrix} 0 & 0 & 0 & 0 & 0 & 0 \\ 0 & \pm c & 0 & 0 & 0 & c^2 \\ 0 & 0 & \pm c & 0 & -c^2 & 0 \\ 0 & 0 & 0 & 0 & 0 & 0 \\ 0 & 0 & -1 & 0 & \pm c & 0 \\ 0 & 1 & 0 & 0 & 0 & \pm c \end{pmatrix}, \quad (4.4d)$$

$$\mathcal{K}_2^\pm = \frac{1}{2} \begin{pmatrix} \pm c & 0 & 0 & 0 & 0 & -c^2 \\ 0 & 0 & 0 & 0 & 0 & 0 \\ 0 & 0 & \pm c & c^2 & 0 & 0 \\ 0 & 0 & 1 & \pm c & 0 & 0 \\ 0 & 0 & 0 & 0 & 0 & 0 \\ -1 & 0 & 0 & 0 & 0 & \pm c \end{pmatrix}. \quad (4.4e)$$

The decomposition of the jump $\Delta u = u_R - u_L$ (see (4.6b)) can be written as

$$\Delta u = \mathcal{R}_i \tilde{\alpha}_i, \quad (4.5a)$$

where $\tilde{\alpha}_i = (\alpha_1, \dots, \alpha_6)_{\mathcal{K}_i}^T$ is a yet unknown vector of coefficients. Simple matrix multiplication leads to

$$\tilde{\alpha}_i = \mathcal{R}_i^{-1} \Delta u, \quad (4.5b)$$

and, explicitly, for $i = 1, 2$ we find:

$$\tilde{\alpha}_1 = \frac{1}{2c} \begin{pmatrix} -\Delta u_2 + c\Delta u_6 \\ \Delta u_3 + c\Delta u_5 \\ 2c\Delta u_1 \\ 2c\Delta u_4 \\ \Delta u_2 + c\Delta u_6 \\ -\Delta u_3 + c\Delta u_5 \end{pmatrix}, \quad (4.5c)$$

$$\tilde{\alpha}_2 = \frac{1}{2c} \begin{pmatrix} \Delta u_1 + c\Delta u_6 \\ -\Delta u_3 + c\Delta u_4 \\ 2c\Delta u_2 \\ 2c\Delta u_5 \\ -\Delta u_1 + c\Delta u_6 \\ \Delta u_3 + c\Delta u_4 \end{pmatrix}. \quad (4.5d)$$

In particular, for the two-dimensional FV scheme we need the matrices $\mathcal{C}_{ij,\beta}$ defined by equation (4.11). For our purposes we omit the subscripts in this appendix and get with the abbreviations

$$a = n_{ij,\beta}^{(1)}; \quad b = n_{ij,\beta}^{(2)}; \quad a^2 + b^2 = 1, \quad (4.6a)$$

$$\mathcal{C}(a, b) = a\mathcal{K}_1 + b\mathcal{K}_2 = \begin{pmatrix} & & & 0 & 0 & -c^2b \\ & & & 0 & 0 & c^2a \\ & & & c^2b & -c^2a & 0 \\ 0 & 0 & b & & & \\ 0 & 0 & -a & & 0 & \\ -b & a & 0 & & & \end{pmatrix}. \quad (4.6b)$$

This matrix has the same eigenvalues as the matrices \mathcal{K}_i , $i = 1, 2$, and are given by (4.1c). The right and left eigenvectors of $\mathcal{C}(a, b)$ are obtained from

$$\mathcal{R}_c = (r^1, \dots, r^6)_c = \begin{pmatrix} cb & 0 & a & 0 & -cb & 0 \\ -ca & 0 & b & 0 & ca & 0 \\ 0 & c & 0 & 0 & 0 & -c \\ 0 & -b & 0 & a & 0 & -b \\ 0 & a & 0 & b & 0 & a \\ 1 & 0 & 0 & 0 & 1 & 0 \end{pmatrix}, \quad (4.6c)$$

$$\mathcal{R}_c^{-1} = (l^1, \dots, l^6)_c^T = \frac{1}{2c} \begin{pmatrix} b & -a & 0 & 0 & 0 & c \\ 0 & 0 & 1 & -cb & ca & 0 \\ 2ca & 2cb & 0 & 0 & 0 & 0 \\ 0 & 0 & 0 & 2ca & 2cb & 0 \\ -b & a & 0 & 0 & 0 & c \\ 0 & 0 & -1 & -cb & ca & 0 \end{pmatrix}, \quad (4.6d)$$

leading with (4.4a), (4.4b) to

$$\mathcal{C}^\pm(a, b) = \frac{1}{2} \begin{pmatrix} \pm cb^2 & \mp cab & 0 & 0 & 0 & -c^2b \\ \mp cab & \pm ca^2 & 0 & 0 & 0 & c^2a \\ 0 & 0 & \pm c & c^2b & -c^2a & 0 \\ 0 & 0 & b & \pm cb^2 & \mp cab & 0 \\ 0 & 0 & -a & \mp cab & \pm ca^2 & 0 \\ -b & a & 0 & 0 & 0 & \pm c \end{pmatrix}. \quad (4.6e)$$

Obviously, (4.4d) and (4.4e) are obtained if $a = 1$, $b = 0$ and $a = 0$, $b = 1$, respectively.

E Test Problems for the homogeneous Maxwell Equations

Two typical problems based on the homogeneous Maxwell equations are solved analytically in this appendix, and are used as reference solutions testing the applied numerical methods discussed in Section 4. For theoretical investigations it is convenient to decompose the vector field $\mathbf{V} = (V_x, V_y, V_z)^T$ into a parallel and transverse part with respect to the z -axis:

$$\mathbf{V} = \mathbf{V}_\perp + V_z \mathbf{e}_z; \quad \mathbf{V}_\perp = (\mathbf{e}_z \times \mathbf{V}) \times \mathbf{e}_z, \quad (5.1)$$

where \mathbf{e}_z is the unit vector parallel to this axis. Following [24], Maxwell's equations can be written according to

$$\nabla_\perp H_z - \partial_z \mathbf{H}_\perp = \mathbf{e}_z \times \partial_t \mathbf{D}_\perp, \quad (5.2a)$$

$$\mathbf{e}_z \cdot (\nabla_\perp \times \mathbf{H}_\perp) = \partial_t D_z, \quad (5.2b)$$

$$\nabla_\perp \cdot \mathbf{D}_\perp = -\partial_z D_z, \quad (5.2c)$$

$$\nabla_\perp E_z - \partial_z \mathbf{E}_\perp = -\mathbf{e}_z \times \partial_t \mathbf{B}_\perp, \quad (5.2d)$$

$$\mathbf{e}_z \cdot (\nabla_\perp \times \mathbf{E}_\perp) = -\partial_t B_z, \quad (5.2e)$$

$$\nabla_\perp \cdot \mathbf{B}_\perp = -\partial_z B_z, \quad (5.2f)$$

where ∇_\perp is the transverse part of the gradient operator and \mathbf{E} and \mathbf{B} denote the electric field and magnetic induction, respectively. For our purpose, the displacement \mathbf{D} and magnetic field \mathbf{H} are simply given by:

$$\mathbf{D} = \epsilon_0 \mathbf{E}, \quad (5.2g)$$

$$\mathbf{H} = \frac{1}{\mu_0} \mathbf{B}. \quad (5.2h)$$

The first test problem is obtained from (5.2) by assuming that the fields are independent of the z -coordinate and $B_z = 0$ everywhere. Further, the boundary condition

$$E_z|_{\partial G} = 0, \quad (5.3a)$$

is imposed, which means that the field component E_z vanishes at the boundary surface ∂G of the domain $G = \{(x, y) | 0 \leq x \leq a, 0 \leq y \leq b\}$. Since Maxwell's equations decouple, we can neglect for the further considerations the transverse field \mathbf{E}_\perp and find

$$\left(\nabla_\perp^2 - \frac{1}{c} \partial_t^2 \right) E_z(x, y, t) = 0, \quad (5.3b)$$

$$\partial_t \mathbf{B}_\perp(x, y, t) = \mathbf{e}_z \times \nabla_\perp E_z, \quad (5.3c)$$

where $\nabla_\perp^2 = \partial_x^2 + \partial_y^2$. The general general solution of the wave equation (5.3b) with the boundary condition (5.3a) is given by

$$E_z(x, y, t) = \sum_{m,n=1}^{\infty} [A_{mn} \cos(\omega_{mn}t) + B_{mn} \sin(\omega_{mn}t)] \sin(a_m x) \sin(b_n y), \quad (5.4a)$$

with

$$a_m = m \frac{\pi}{a}, \quad b_n = n \frac{\pi}{b}, \quad \omega_{mn}^2 = c^2 (a_m^2 + b_n^2). \quad (5.4b)$$

The as yet unknown coefficients A_{mn} and B_{mn} are determined from

$$A_{mn} = \frac{4}{ab} \int_0^a \int_0^b E_{z0}(x, y) \sin(a_m x) \sin(b_n y) dx dy, \quad (5.4c)$$

$$B_{mn} = \frac{4}{ab\omega_{mn}} \int_0^a \int_0^b \dot{E}_{z0}(x, y) \sin(a_m x) \sin(b_n y) dx dy, \quad (5.4d)$$

where

$$E_{z0}(x, y) = E_z(x, y, t)|_{t=0}, \quad (5.4e)$$

$$\dot{E}_{z0}(x, y) = \partial_t E_z(x, y, t)|_{t=0}, \quad (5.4f)$$

are the initial conditions of the electric field E_z . Hence, (5.3b) with (5.3a) and (5.4e), (5.4f) form an initial-boundary-value (IVB) problem for the so-called TM waves. Simple standing waves are obtained if $E_{z0} = E_0 \sin(a_\mu x) \sin(b_\nu y)$ and $\dot{E}_{z0} = 0$, resulting in $A_{mn} = \delta_{\mu m} \delta_{\nu n}$ and $B_{mn} = 0$. For our applications we choose Gaussian shaped initial conditions for E_z :

$$E_{z0}(x, y) = E_0 e^{-\frac{(x-x_0)^2 + (y-y_0)^2}{2\tau^2 c^2}}, \quad (5.5a)$$

$$\dot{E}_{z0}(x, y) = 0, \quad (5.5b)$$

where the height E_0 , the location (x_0, y_0) and the width τ of the initial pulse are arbitrary parameters. Inserting (5.5a), (5.5b) into (5.4c), (5.4d) results in

$$B_{mn} = 0, \quad (5.5c)$$

$$\begin{aligned} A_{mn} &= \frac{4E_0}{ab} I_m(x_0, a) I_n(y_0, b) \\ &= \frac{4E_0}{ab} \left(\int_0^a e^{-\frac{(x-x_0)^2}{2\tau^2 c^2}} \sin(a_m x) dx \right) \left(\int_0^b e^{-\frac{(y-y_0)^2}{2\tau^2 c^2}} \sin(b_n y) dy \right). \end{aligned} \quad (5.5d)$$

The integration can be performed in closed form [1], yielding

$$\int_0^\Omega e^{-A(z-z_0)^2} \begin{Bmatrix} \sin(Kz) \\ \cos(Kz) \end{Bmatrix} dz = \frac{1}{2} \sqrt{\frac{\pi}{A}} e^{-\frac{K^2}{4A}} \begin{Bmatrix} \text{Im}(f) \\ \text{Re}(f) \end{Bmatrix}, \quad (5.6a)$$

$$f = e^{iKz_0} \left\{ \text{erf} \left[\sqrt{A} \left(\Omega - z_0 - i \frac{K}{2A} \right) \right] - \text{erf} \left[\sqrt{A} \left(-z_0 - i \frac{K}{2A} \right) \right] \right\}. \quad (5.6b)$$

Assuming that $B_x(x, y, 0) = B_y(x, y, 0) = 0$, the analytical solution of (5.3b), (5.3c) reads as

$$E_z(x, y, t) = \sum_{m,n=1}^{\infty} A_{mn} \cos(\omega_{mn} t) \sin(a_m x) \sin(b_n y), \quad (5.7a)$$

$$B_x(x, y, t) = - \sum_{m,n=1}^{\infty} \frac{A_{mn} b_n}{\omega_{mn}} \sin(\omega_{mn} t) \sin(a_m x) \cos(b_n y), \quad (5.7b)$$

$$B_y(x, y, t) = \sum_{m,n=1}^{\infty} \frac{A_{mn} a_m}{\omega_{mn}} \sin(\omega_{mn} t) \cos(a_m x) \sin(b_n y), \quad (5.7c)$$

where a_m , b_n , ω_{mn} and A_{mn} are obtained from (5.4b) and (5.5d), respectively. Under the assumption that $E_z = 0$ everywhere and the boundary condition $\partial_n B_z|_{\partial G} = 0$, we found for the solution of the so-called TE waves:

$$B_z(x, y, t) = \sum_{m,n=0}^{\infty} \tilde{A}_{mn} \cos(\omega_{mn} t) \cos(a_m x) \cos(b_n y), \quad (5.8a)$$

$$E_x(x, y, t) = -c^2 \sum_{m,n=0}^{\infty} \frac{\tilde{A}_{mn} b_n}{\omega_{mn}} \sin(\omega_{mn} t) \cos(a_m x) \sin(b_n y), \quad (5.8b)$$

$$E_y(x, y, t) = c^2 \sum_{m,n=0}^{\infty} \frac{\tilde{A}_{mn} a_m}{\omega_{mn}} \sin(\omega_{mn} t) \sin(a_m x) \cos(b_n y), \quad (5.8c)$$

where

$$\begin{aligned} \tilde{A}_{mn} &= \frac{4B_0}{ab} \tilde{I}_m(x_0, a) \tilde{I}_n(y_0, b) \\ &= \frac{4B_0}{ab} \left(\int_0^a e^{-\frac{(x-x_0)^2}{2r^2c^2}} \cos(a_m x) dx \right) \left(\int_0^b e^{-\frac{(y-y_0)^2}{2r^2c^2}} \cos(b_n y) dy \right). \end{aligned} \quad (5.8d)$$

As the second example, we consider the TM and TE modes of a cylindrical resonant cavity with the radius $0 \leq r \leq R$ and the length $0 \leq z \leq L$. With the simple time dependence of the electromagnetic fields

$$V(\mathbf{x}, t) = V(\mathbf{x}) e^{-i\omega t} \quad (5.9)$$

we follow the analysis of [24] using equation (5.2) and obtain

• TM fields:

$$E_z(z, r, t) = E_0 \cos(k_\nu z) J_0(\gamma_{0n} r) \cos(\omega_{0n\nu} t), \quad (5.10a)$$

$$E_r(z, r, t) = E_0 \frac{k_\nu}{\gamma_{0n}} \sin(k_\nu z) J_1(\gamma_{0n} r) \cos(\omega_{0n\nu} t), \quad (5.10b)$$

$$B_\varphi(z, r, t) = -E_0 \frac{\omega_{0n\nu}}{c^2 \gamma_{0n}} \cos(k_\nu z) J_1(\gamma_{0n} r) \sin(\omega_{0n\nu} t), \quad (5.10c)$$

with

$$k_\nu = \nu \frac{\pi}{L}; \quad \nu = 0, 1, 2, \dots, \quad (5.10d)$$

and

$$\omega_{0n\nu}^2 = c^2 (k_\nu^2 + \gamma_{0n}^2); \quad \gamma_{0n} = \frac{r_{0n}}{R}. \quad (5.10e)$$

Here, J_0, J_1 are Bessel functions of first kind, r_{0n} is the n th root of the equation $J_0(r_{0n}) = 0$, $n = 1, 2, 3, \dots$, and E_0 is an arbitrary constant, usually set equal to one.

• TE fields:

$$B_z(z, r, t) = B_0 \sin(\kappa_\nu z) J_0(\gamma'_{0n} r) \cos(\omega'_{0n\nu} t), \quad (5.11a)$$

$$B_r(z, r, t) = -B_0 \frac{\kappa_\nu}{\gamma'_{0n}} \cos(\kappa_\nu z) J_1(\gamma'_{0n} r) \cos(\omega'_{0n\nu} t), \quad (5.11b)$$

$$E_\varphi(z, r, t) = B_0 \frac{\omega'_{0n\nu}}{\gamma'_{0n}} \sin(\kappa_\nu z) J_1(\gamma'_{0n} r) \sin(\omega'_{0n\nu} t), \quad (5.11c)$$

with

$$\kappa_\nu = \nu \frac{\pi}{L}; \quad \nu = 1, 2, \dots, \quad (5.11d)$$

and

$$\omega'_{0n\nu}{}^2 = c^2 (\kappa_\nu^2 + \gamma'_{0n}{}^2); \quad \gamma'_{0n} = \frac{r'_{0n}}{R}, \quad (5.11e)$$

where B_0 is a constant and r'_{0n} is the n th root of the equation $J'_0(r'_{0n}) = 0$, $n = 1, 2, 3, \dots$. The roots r_{0n} as well as r'_{0n} are tabulated, for example, in [1].

F Test Problems for the inhomogeneous Maxwell Equations

In order to test the numerical schemes for the inhomogeneous Maxwell equations, we consider a simple two-dimensional sender problem which can be solved analytically. Therefore, we assume that the time-dependent current of the form $I(t) = I_0 \cos(\omega t)$ flows in a wire at the position (x_0, y_0) perpendicular to the (x, y) -plane. The current

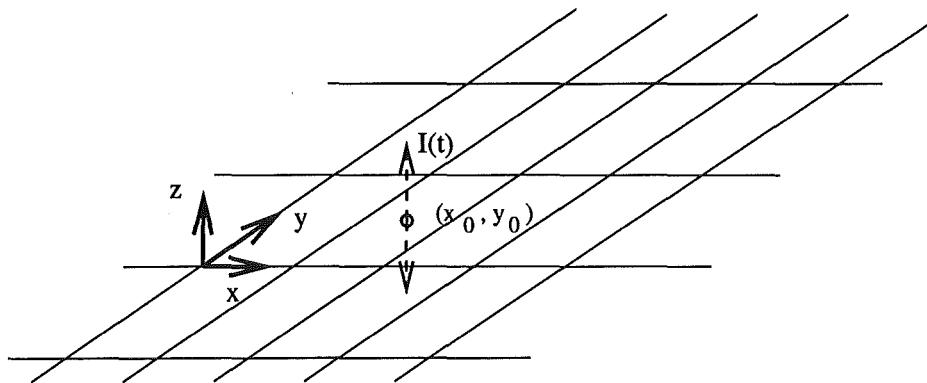


Figure 1: Dipole model of a two-dimensional dipole located at (x_0, y_0) .

density is then obtained from

$$\mathbf{j}(x, y, t) = J_z(x, y, t) \mathbf{e}_z, \quad (6.1a)$$

$$J_z(x, y, t) = I_0 \delta(x - x_0) \delta(y - y_0) \cos(\omega t), \quad (6.1b)$$

where I_0 and ω are arbitrary constants. This current induces a magnetic induction $\mathbf{B} = (B_x, B_y, 0)^T$ in the (x, y) -plane resulting in an electric field $\mathbf{E} = (0, 0, E_z)^T$ perpendicular to this plane. From the time-dependent Maxwell's equations, we obtain the following two-dimensional model system:

$$\left(\partial_x^2 + \partial_y^2 - \frac{1}{c^2} \partial_t^2 \right) E_z(x, y, t) = \mu_0 \dot{J}_z, \quad (6.2a)$$

$$\partial_t B_x(x, y, t) = -\partial_y E_z, \quad (6.2b)$$

$$\partial_t B_y(x, y, t) = \partial_x E_z, \quad (6.2c)$$

which will be called the 2d-dipole problem. The particular integral for the sender problem of the D'Alembert-type wave equations (6.2a) is determined with the retarded Green's function [11, 24]. If there are no boundary surfaces, the two-dimensional retarded Green function reads as [37]

$$G(P, \tau) = -\frac{c}{2\pi} \frac{\theta(c\tau - P)}{\sqrt{c^2\tau^2 - P^2}}. \quad (6.3a)$$

Here, c denotes the speed of light, $\tau = t - t_0$ and P is given by $P^2 = (x - \alpha)^2 + (y - \beta)^2$. Then, the solution of (6.2a) can be found from

$$E_z(x, y, t) = \mu_0 \int_{-\infty}^{\infty} \int_{\mathcal{G}} G(x - \alpha, y - \beta, t - t_0) \dot{J}_z(\alpha, \beta, t_0) d\alpha d\beta dt_0. \quad (6.3b)$$

Performing explicitly the analysis where the integrals can be calculated in closed form, we obtain cylindrical waves

$$\begin{aligned} E_z(x, y, t) &= E_0 \operatorname{Im} \left(i e^{-i\omega t} H_0^{(1)}(kR) \right), \\ &= E_0 [\cos(\omega t) J_0(kR) + \sin(\omega t) Y_0(kR)] \end{aligned} \quad (6.4a)$$

where J_n , Y_n denote the Bessel functions of the first and second kind, respectively, and $H_n^{(1)}$ are the Hankel functions, defined according to $H_n^{(1)} = J_n + i Y_n$. Assuming that the magnetic induction \mathbf{B} is initially equal to zero, we obtain from (6.2b), (6.2c)

$$B_x(x, y, t) = \frac{k}{\omega} E_0 \frac{y - y_0}{R} [\sin(\omega t) J_1(kR) + (1 - \cos(\omega t)) Y_1(kR)], \quad (6.4b)$$

$$B_y(x, y, t) = -\frac{k}{\omega} E_0 \frac{x - x_0}{R} [\sin(\omega t) J_1(kR) + (1 - \cos(\omega t)) Y_1(kR)] \quad (6.4c)$$

where the wave number k , the radius R and the constant E_0 are given by

$$k = \frac{\omega}{c}, \quad R^2 = (x - x_0)^2 + (y - y_0)^2, \quad E_0 = -\frac{1}{4} \mu_0 I_0 \omega. \quad (6.4d)$$

Very similar investigations can be performed for the three-dimensional case. With the three-dimensional boundary-free Green's function, one obtains the so-called Liénard-Wiechert potentials [24]. From these, one can calculate in lowest order the fields of the Hertz dipole [28, 52] which are given by

$$\begin{aligned} \mathbf{E}(\mathbf{x}, t) &= \frac{q}{4\pi\epsilon_0} \left\{ \frac{3 \left[\mathbf{n} \cdot \mathbf{r} \left(t - \frac{|\mathbf{x}|}{c} \right) \right] \mathbf{n} - \mathbf{r} \left(t - \frac{|\mathbf{x}|}{c} \right)}{|\mathbf{x}|^3} \right. \\ &\quad + \frac{3 \left[\mathbf{n} \cdot \dot{\mathbf{r}} \left(t - \frac{|\mathbf{x}|}{c} \right) \right] \mathbf{n} - \dot{\mathbf{r}} \left(t - \frac{|\mathbf{x}|}{c} \right)}{c|\mathbf{x}|^2} \\ &\quad \left. + \frac{\left[\mathbf{n} \cdot \ddot{\mathbf{r}} \left(t - \frac{|\mathbf{x}|}{c} \right) \right] \mathbf{n} - \ddot{\mathbf{r}} \left(t - \frac{|\mathbf{x}|}{c} \right)}{c^2|\mathbf{x}|} \right\}, \end{aligned} \quad (6.5a)$$

$$\mathbf{B}(\mathbf{x}, t) = \frac{q}{4\pi} \sqrt{\frac{\mu_0}{\epsilon_0}} \left\{ \frac{\dot{\mathbf{r}} \left(t - \frac{|\mathbf{x}|}{c} \right) \times \mathbf{n}}{c|\mathbf{x}|^2} + \frac{\ddot{\mathbf{r}} \left(t - \frac{|\mathbf{x}|}{c} \right) \times \mathbf{n}}{c^2|\mathbf{x}|} \right\}, \quad (6.5b)$$

with $\mathbf{n} = \mathbf{x}/|\mathbf{x}|$. Here, $\mathbf{r}(t)$ is the orbit of the charge q , usually assumed to be $\mathbf{r}(t) = d \sin(\omega t) \mathbf{e}_z$ where d is the extension of the orbit. Terms proportional to $\frac{1}{c^2|\mathbf{x}|}$ are called the long range approximation of the electromagnetic fields.

References

- [1] Abramowitz, M., Stegun, I.A. (editors); *Handbook of Mathematical Functions*, Dover Publications, New York, 1972.
- [2] Ambrosiano, J.J., Brandon, S.T., Löhner, R., and DeVore, C.R.; '*Electromagnetics via the Taylor-Galerkin Finite Element Method on Unstructured Grids*', J. Comput. Phys. **110**, 310 (1994).
- [3] Balescu, R.; *Transport Processes in Plasmas*, North-Holland, Amsterdam, 1988.
- [4] Birdsall, C.K. and Langdon, A.B.; *Plasma Physics via Computer Simulation*, McGraw-Hill, New York, 1985.
- [5] Bluhm, H., Böhnel, K., Buth, L., Hoppé, P., Karow, H.U., Klumpp, A., Rusch, D., Scherer, T., Schülken, U., and Singer, J.; in Digest of Technical Papers, 5th IEEE Pulsed Power Conf., Arlington, 1985, p.114.
- [6] Bluhm, H., Hoppé, P., Laqua, H., and Rusch, D.; '*Production and investigation of TW proton beams for an annular diode using strong radial magnetic insulation fields and a preformed anode plasma source*', Proc. IEEE **80**, 995 (1992).
- [7] Bluhm, H.J., Laqua, H.P., Buth, L., Hoppé, P.J.W., and Rusch, D.; '*Formation of a homogeneous hydrogen plasma layer for the production of Terawatt ion beams*', IEEE Trans. Plasma Sci. **21**, 560 (1993).
- [8] Boris, J.P.; '*Relativistic Plasma Simulation - Optimization of a Hybrid Code*', Proc. 4th Conf. on Num. Sim. of Plasmas, NRL Washington DC, 1970.
- [9] Bystritskii, V.M., Didenko, A.N.; *High-Power Ion Beams*, AIP Translation Series, New York, 1985.
- [10] Colella, P.; '*Multidimensional upwind methods for hyperbolic conservation laws*', J. Comput. Phys. **87**, 171 (1990).
- [11] Courant, R. and Hilbert, D.; *Methoden der mathematischen Physik*; Springer-Verlag, Berlin, 1993.
- [12] Davidson, R.C.; *Theory of Nonneutral Plasmas*, Benjamin, Reading, 1974.
- [13] Ehrlich, L.W.; *Iterative Methods for large Linear Systems*, Academic Press, New York, 1990, p.81.
- [14] Enquist, B. and Majda, A.; '*Absorbing Boundary Conditions for the Numerical Simulation of Waves*', Math. Comput. **31**, 629 (1977).
- [15] Godunov, S.K.; '*Finite difference method for numerical computation of discontinuous solutions of the equations of fluid dynamics*', Mat. Sbornik **47**, 271 (1959).

- [16] Halter, E.; *'Die Berechnung elektrostatischer Felder in Pulsleistungsanlagen'*, Kernforschungszentrum Karlsruhe GmbH, **KfK 4072**, Karlsruhe, 1986.
- [17] Halter, E., Kündahl, J., Krauß, M., Munz, C.-D., Schneider, R., Stein, E., Voß, U., and Westermann, T.; *'Interaktive Gittererzeugung im Rahmen eines offenen CAD-Systems'*, 9. DGLR/AG STAB-Symposium 1994, Erlangen, 1994.
- [18] Halter, E., Kündahl, J., *'InGrid, interaktive Gittererzeugung in der Produktsimulation'*, Institut für Innovation und Transfer der FH Karlsruhe, 1994.
- [19] Harten A., Lax, P.D., and Leer, van B.; *'On upstream differencing and Godunov-type schemes for hyperbolic conservation laws'*, SIAM Rev. **25**, 35 (1983).
- [20] Harten, A., Chakravarthy, S.R.; *'Multi-dimensional ENO schemes for general geometries'*, Technical Report, 91-76, ICASE, 1991.
- [21] Hedstrom, G.W.; *'Non-reflecting boundary conditions for nonlinear hyperbolic systems'*, J. Comput. Phys. **30**, 222 (1979).
- [22] Hockney, R.W. and Eastwood, J.W.; *Computer Simulation using Particles*, McGraw-Hill, New York, 1981.
- [23] Holland R.; *'Finite-Difference Solution of Maxwell's Equations in generalized nonorthogonal Coordinates'*, IEEE Trans. Nucl. Sci. **30**, 4589(1983).
- [24] Jackson, J.D.; *Classical Electrodynamics*, Wiley, New York, 1975.
- [25] Jones, M.E.; *'Electromagnetic PIC codes with body-fitted coordinates'*, Proceedings 12th Conference on the Numerical Simulation of Plasmas, San Francisco, 20-24 September 1984, IM3, 1987.
- [26] Kuntz, M.; *'Simulation zeitabhängiger, zweidimensionaler Effekte in Impulsleitungen'*, Diploma Thesis, University Karlsruhe, Karlsruhe, 1992 (unpublished).
- [27] Leer, B. van; *'Toward the ultimate conservative difference scheme V. A second order sequel to Godunov's method'*, J. Comput. Phys. **32**, 101 (1979).
- [28] Lehner, G.; *Elektromagnetische Feldtheorie*, Springer-Verlag, Berlin, 1994.
- [29] Löhner, R. and Ambrosiano, J.; *'A Vectorized Particle Tracer for Unstructured Grids'*, J. Comput. Phys. **91**, 22 (1990).
- [30] LeVeque, R.J.; *Numerical Methods for Conservation Laws*, Birkhäuser, Basel, 1990.
- [31] Lindman, E.L.; *'"Free-Space" Boundary Conditions for the Time-depending Wave Equation'*, J. Comput. Phys. **18**, 66 (1975).
- [32] Madsen, N.K. and Ziolkowski, R.W.; *'A three-dimensional modified finite volume technique for Maxwell's equations'*, Electromagnetics **10**, 147 (1990).

- [33] Madsen, N.K.; *'Divergence Preserving Discrete Surface Integral Methods for Maxwell's Curl Equations Using Non-Orthogonal Unstructured Grids'*, preprint, 1995 (unpublished).
- [34] Marchuk, G.I.; *Methods of Numerical Mathematics*, Springer-Verlag, New York/Heidelberg/Berlin, 1975.
- [35] Matsumoto, M. and Kawata, S.; *'TRIPIC: triangular-mesh PIC code'*, J. Comput. Phys. **87**, 488 (1990).
- [36] Morse, R.L. and Nielson, C.W.; *'Numerical Simulation of the Weibel Instability in One and Two Dimensions'*, Phys. Fluids **14**, 830 (1971).
- [37] Morse, P.M. and Feshbach, H.; *Methods of Theoretical Physics*, McGraw-Hill, New York, 1953.
- [38] Munz, C.-D.; *'On the numerical dissipation of high resolution schemes for hyperbolic conservation laws'*, J. Comput. Phys. **77**, 18 (1988).
- [39] Munz, C.-D.; *'Theorie und Numerik nichtlinearer hyperbolischer Differentialgleichungen'*, Kernforschungszentrum Karlsruhe GmbH, **KfK 4805**, Karlsruhe, 1990.
- [40] Munz, C.-D.; *'Godunov-Typ Verfahren für die Gleichungen der kompressiblen Strömungsmechanik'*, Kernforschungszentrum Karlsruhe GmbH, **KfK 5058**, Karlsruhe, 1992.
- [41] Munz, C.-D., Schneider, R., Stein, E., and Voß, U.; *'Finite-volume method based approximation of Maxwell's curl equations for the self-consistent numerical solution of the Maxwell-Lorentz system'*, in preparation.
- [42] Ohring, S.; *'Application of the Multigrid Method to Poisson's Equation in Boundary-Fitted Coordinates'*, J. Comput. Phys. **50**, 307 (1983).
- [43] Pointon, T.D., Desjarlais, M.P., Seidel, D.B., Slutz, S.A., Coats, R.S., Kiefer, M.L., and Quintenz, J.P.; *'Three-dimensional particle-in-cell simulation of applied-B ion diodes'*, Phys. Plasmas **1**, 429, (1994).
- [44] Press, W.H., Flannery, B.P., Teukolsky, S.A., and Vetterling, W.T.; *Numerical Recipes*, Cambridge University Press, Cambridge, 1987.
- [45] Qin, B.-L. and Pedrow, P.D.; *'Particle-in-cell Simulation of Bipolar dc Corona'*, IEEE Trans. on Dielectrics and Electrical Insulation **1**, 1105 (1994).
- [46] Roe, P.L.; *'Approximate Riemann solvers, parameter vectors, and difference schemes'*, J. Comput. Phys. **43**, 357 (1981).
- [47] Roe, P.L.; *The use of the Riemann problem in finite difference schemes*; Lecture Notes in Physics 141, Springer-Verlag, Berlin/Heidelberg, 1981.

- [48] Schneider, R. and Munz, C.-D.; *'The Approximation of Two-fluid Plasma Flow with explicit Upwind Schemes'*, appears in Int. J. Num. Mod..
- [49] Schimassek, W., Bauer, W., and Stoltz, O.; *'Generation of a focused proton beam with a self-magnetically B_{Θ} -insulated ion diode'*, Rev. Sci. Instrum. **62**, 168 (1991).
- [50] Seldner, D. and Westermann, T.; *'Algorithms for Interpolation and Localization in Irregular 2D Meshes'*, J. Comput. Phys. **79**, 1 (1988).
- [51] Sod, G.A.; *Numerical Methods in Fluid Dynamics*, Cambridge University Press, Cambridge, 1985.
- [52] Sommerfeld, A.; *Elektrodynamik*, Band III, Harri Deutsch Verlag, Thun, 1977.
- [53] Sommerfeld, A.; *Optik*, Band IV, Harri Deutsch Verlag, Thun, 1977.
- [54] Stoer, J. and Bulirsch, R.; *Einführung in die Numerische Mathematik II*, Springer-Verlag, Berlin, 1978.
- [55] Strang, G.; *'On the construction and comparison of difference schemes'*, SIAM J. Numer. Anal. **5**, 506 (1968).
- [56] Thompson, J.F., Warsi, Z.U.A. and Mastin, C.W.; *'Boundary-fitted coordinate systems for numerical solution of partial differential equations - A review'*, J. Comput. Phys. **47**, 1 (1982).
- [57] Thompson, J.F., Warsi, Z.U.A. and Mastin, C.W.; *Numerical Grid Generation, Foundations and Applications*, North-Holland, New York, Amsterdam, Oxford, 1985.
- [58] Thompson, K.W.; *'Time dependent boundary conditions for hyperbolic systems'*, J. Comput. Phys. **68**, 1 (1987).
- [59] Wagatha, L.; *'Approximation of Pseudodifferential Operators in Absorbing Boundary Conditions for Hyperbolic Equations'*, Numerische Mathematik Vol. 42, Springer-Verlag, Berlin, 1983.
- [60] Weiland, T.; *'Eine Methode zur Lösung der Maxwellgleichungen für sechskomponentige Felder auf diskreter Basis'*, AEÜ, Band 31, Heft 3, 116 (1977).
- [61] Weiland, T.; *'On the Numerical Solution of Maxwell's Equations and Applications in the Field of Accelerator Physics'*, Deutsches Elektronen-Synchrotron, DESY 84-006, Hamburg, 1984.
- [62] Wesseling, P.; *'A Robust and Efficient Multigrid Method'*, in: Multigrid Methods; Hackbusch, W. and Trottenberg, U. (eds), Lecture Notes in Math. 960, p.614-630, Springer-Verlag, Berlin, 1982.

- [63] Westermann, T.; *'Teilchenfortbewegung in elektro-magnetischen Feldern'*, Kernforschungszentrum Karlsruhe GmbH, **KfK 4325**, Karlsruhe, 1988.
- [64] Westermann, T.; *'Optimization by numerical simulation of the focusing properties of self-magnetically insulated ion diodes'*, Appl. Phys. Lett. **58**, 696 (1991).
- [65] Westermann, T.; *'Localization Schemes in 2D Boundary-Fitted Grids'*, J. Comput. Phys. **101**, 307 (1992).
- [66] Westermann, T. and Schuldt, R.; *'Investigations of diffusional effects in applied-B ion diodes'*, Phys. Fluids B **5**, 4408 (1993).
- [67] Westermann, T.; *'Numerical modelling of the stationary Maxwell-Lorentz System in technical devices'*, Int. J. Num. Mod. **7**, 43 (1994).
- [68] Westermann, T.; *'Particle-in-Cell Simulations with Moving Boundaries - Adaptive Mesh Generation'*, J. Comput. Phys. **114**, 161 (1994).
- [69] Winslow, A.M.; *'Numerical solution of the quasilinear Poisson equation in a nonuniform triangle mesh'*, J. Comput. Phys. **2**, 149 (1967).
- [70] Yee, K.S.; *'Numerical Solution of Initial Boundary Value Problems Involving Maxwell's Equations in Isotropic Media'*, IEEE Trans. Ant.& Prop. **14**, 302(1966).
- [71] Zhou, P.-B.; *Numerical Analysis of Electromagnetic Fields*, Springer-Verlag, Berlin/Heidelberg, 1993.